Developing Microelectrode and Microfluidic Devices for Studying Neuronal Development

Kyriakos Michail

Submitted for the degree of Doctor of Philosophy

Heriot-Watt University

School of Engineering & Physical Sciences

June 2020

ABSTRACT

In this thesis technologies are developed to make integrated devices to study neural activity *in vitro*: microelectrode arrays (MEAs), microfluidic modules and human neural stem cells (hNSCs). My aim was to develop novel *in vitro* models for neurodegenerative diseases such as multiple sclerosis (MS). As MS is a chronic neuroinflammatory disease that results in loss of myelin it evokes changes in neuronal conduction velocity in the central nervous system (CNS). Therefore, developing a system that could electrically follow the progress of myelination through immunocytochemistry and via conduction velocity would be of great value in MS research. As a step towards this goal, I developed and fabricated functional custom MEAs on which the electrical activity of human dopaminergic neurons (differentiated from hNSCs) and mouse spinal cord cells was recorded. Microfluidic microchannels measuring 5 μm wide were successful in separating the cell bodies of human cerebral cortical neurons (hCCNs) from the axons in two different compartments. Mouse spinal cord cultures were electrically active from 2 days *in vitro* (DIV) and remained active up until 52 DIV. Nominal conduction velocity (NCV) measurements were recorded from these cultures on commercial MEAs from 6 to 24 DIV. NCV increased from 0.03 m/s at 2 DIV to 15.00 m/s at 24 DIV indicating increasing myelination. Combining this data with molecular methodologies promises new approaches in developing more human-relevant models for MS research and will provide a deeper understanding of the process of myelination and possible new treatments that may one day cure MS.

ACKNOWLEDGEMENTS

First, I would like to express my deepest gratitude to my supervisor Euan Brown who was always available when I needed him, for all the knowledge, help and advice he provided throughout the years.

I would also like to thank Julia Edgar for all her advice and feedback as well as providing the mouse spinal cord cells and Neil Ross for the guidance and training in the nanofabrication facility.

A special thank you to those who aided my research through their advice: Graeme Whyte, Tim Ryan, Nick Leslie, David Flynn, Maïwenn Kersaudy-Kerhoas and Gary Beveridge.

I can't not mention Matthew Euston, the founder of the spearing crew, who offered his help at any moment and for keeping me sane in the lab.

Thank you to all my fellow PoBBBs members that made this whole experience more pleasant with their great company.

Finally, I would like to thank Medical Research Scotland and Epigem Limited for funding my project.

Research Thesis Submission

Please note this form should be bound into the submitted thesis.

Name:	Kyriakos Michail		
School:	EPS		
Version: *(i.e. First, Resubmission, Final)*	Final	Degree Sought:	Doctor of Philosophy

Declaration

In accordance with the appropriate regulations I hereby submit my thesis and I declare that:

1. The thesis embodies the results of my own work and has been composed by myself
2. Where appropriate, I have made acknowledgement of the work of others
3. The thesis is the correct version for submission and is the same version as any electronic versions submitted*.
4. My thesis for the award referred to, deposited in the Heriot-Watt University Library, should be made available for loan or photocopying and be available via the Institutional Repository, subject to such conditions as the Librarian may require
5. I understand that as a student of the University I am required to abide by the Regulations of the University and to conform to its discipline.
6. I confirm that the thesis has been verified against plagiarism via an approved plagiarism detection application e.g. Turnitin.

ONLY for submissions including published works

Please note you are only required to complete the Inclusion of Published Works Form (page 2) if your thesis contains published works)

7. Where the thesis contains published outputs under Regulation 6 (9.1.2) or Regulation 43 (9) these are accompanied by a critical review which accurately describes my contribution to the research and, for multi-author outputs, a signed declaration indicating the contribution of each author (complete)
8. Inclusion of published outputs under Regulation 6 (9.1.2) or Regulation 43 (9) shall not constitute plagiarism.

* *Please note that it is the responsibility of the candidate to ensure that the correct version of the thesis is submitted.*

Signature of Candidate:		Date:	02/10/2020

Submission

Submitted By *(name in capitals):*	KYRIAKOS MICHAIL
Signature of Individual Submitting:	
Date Submitted:	02/10/2020

For Completion in the Student Service Centre (SSC)

Limited Access	Requested	Yes		No		Approved	Yes		No	
E-thesis Submitted ***(mandatory for final theses)***										
Received in the SSC by *(name in capitals):*						Date:				

Inclusion of Published Works

Please note you are only required to complete the Inclusion of Published Works Form if your thesis contains published works under Regulation 6 (9.1.2)

Declaration

This thesis contains one or more multi-author published works. In accordance with Regulation 6 (9.1.2) I hereby declare that the contributions of each author to these publications is as follows:

Citation details	e. g. Author 1 and Author 2, Title of paper, Title of Journal, X, XX-XX (20XX)
Author 1	Contribution….
Author 2	Contribution….
Signature:	
Date:	

Citation details	e. g. Author 1 and Author 2, Title of paper, Title of Journal, X, XX-XX (20XX)
Author 1	Contribution….
Author 2	Contribution….
Signature:	
Date:	

Citation details	e. g. Author 1 and Author 2, Title of paper, Title of Journal, X, XX-XX (20XX)
Author 1	Contribution….
Author 2	Contribution….
Signature:	
Date:	

Please included additional citations as required.

TABLE OF CONTENTS

GLOSSARY

AMPA	α-amino-3-hydroxy-5-methyl-4-isoxazolepropionic acid
CMOS	Complementary metal oxide semiconductor technology
CNP	2’ , 3’ -cyclic nucleotide 3’-phosphodiesterase
CNQX	Cyanquixaline
CNS	Central nervous system
CSI	Coherence scanning interferometry
D-PBS	Dulbecco’s Phosphate-Buffered Saline
DI	De-ionised
DIV	Days *in vitro*
DRG	Dorsal root ganglion
EAE	Experimental autoimmune encephalomyelitis
EGF	Epidermal growth factor
ESPC	Excitatory spontaneous postsynaptic current
FDM	Fused deposition modelling
FEP	Fluorinated ethylene-propylene
FGF	Fibroblast growth factor
GABA	γ-aminobutyric acid
GFAP	Glial fibrillary acidic protein
hCCN	Human cerebral cortical neuron
hESC	Human embryonic stem cell
hiPSC	Human induced pluripotent stem cell
IBA1	Ionised calcium binding adaptor molecule 1
MBP	Myelin basic protein
MEA	Microelectrode array
MIC	Metal ion containing
MIF	Metal ion free
MS	Multiple sclerosis
Na_v	Voltage-gated sodium channel
NCV	Nominal conduction velocity
NeuN	Neuronal nuclei
NF	Neurofilament
NG2	Neural/glial antigen 2
NMDA	N-methyl-D-aspartate

OPC	Oligodendrocyte progenitor cell
PD	Parkinson’s disease
PDMS	Polydimethylsiloxane
PLL	Poly-L-lysine
PLP	Proteolipid protein
PMMA	Poly(methyl methacrylate)
PNS	Peripheral nervous system
PVD	Physical vapour deposition
RD	Recording device
SC	Schwann cell
SEM	Standard error of the mean
SHH	Sonic Hedgehog
TEA	Triethylammonium
TH	Tyrosine hydroxylase
TTX	Tetrodotoxin
UV	Ultraviolet
WIV	Weeks *in vitro*
XF	Xeno free

Contributions of others to this Thesis

The flow modelling data used for creating Figure 2.17 (Chapter 2) was carried out by Janez Javornik, who ran the flow simulations as part of an Erasmus Plus studentship. The parameters were refined in discussion with me including dimensions, pressures, flow rates and time of simulation.

The electrophysiology data for human dopaminergic neurons allowing for comparisons with human cerebral cortical neurons were kindly provided by Matthew Euston. These include Figures 3.6, 3.7B, 3.8B, 3.9B and C (Chapter 3). Also, for comparisons purposes the immunofluorescence images in Figure 4.4C (Chapter 4).

The immunofluorescence images in Figure 4.1 (Chapter 4) were not obtained by me but were generated as part of joint work and have been included in a publication where I was a co-author (Bijland *et al.*, 2019). I included them in order to offer a comparison with the electrical activity and nominal conduction velocity data obtained from commercial microelectrode arrays.

PUBLICATIONS

Bijland, S., Thomson, G., Euston, M., **Michail, K.,** Thümmler, K., Mücklisch, S., Crawford, C.L., Barnett, S.C., McLaughlin, M., Anderson, T.J., Linington, C., Brown, E.R., Kalkman, E.R., Edgar, J.M., 2019. An *in vitro* model for studying CNS white matter: Functional properties and experimental approaches. F1000Research 8, 1–24. doi:10.12688/f1000research.16802.1

Michail, K., Leslie, N.R., Flynn, D., Kersaudy-Kerhoas, M., Whyte, G., Ryan, T., Brown, E.R., 2017. GLIA Edinburgh 2017: Abstracts Oral Presentations, Posters, Indexes. Glia 65, E319. doi:10.1002/glia.23157

Chapter 1

Introduction

1.1 General Introduction

The development of new technologies and *in vitro* models has been of paramount importance in understanding how human diseases progress and how to treat them. This has been strongly underpinned by the availability of powerful molecular and genetic techniques as well as improvements in live-imaging methodologies such as super-resolution imaging. Perhaps less well recognised has been the quiet revolution that has occurred in microelectrode technology that has allowed the development of microelectrode arrays (MEAs) to detect the electrical activity of multiple excitable cells both *in vivo* and *in vitro* (Yi *et al.*, 2015). The use of MEAs for *in vivo* and *in vitro* analysis grew from the development of single microelectrodes (Renshaw, Forbes and Morison, 1940; Ward and Thomas, 1955). The first true arrays appeared in the early 1970s where extracellular activity was recorded from chick cardiomyocytes (Thomas *et al.*, 1972). Since then, MEAs developed apace with the first electrical recordings from dissociated neurons *in vitro* on a 32 electrode array occurring a few years later (Pine, 1980). At present MEAs are available in different layouts consisting of hundreds of electrodes that are used in *in* vitro and *in vivo* studies as well as complementary metal oxide semiconductor technology (CMOS) arrays consisting of thousands of electrodes (Miccoli *et al.*, 2019).

Coupled with these developments, the discovery of human induced pluripotent stem cells (hiPSCs) (Takahashi and Yamanaka, 2006), have seen an increase in the use of human neuronal cultures to study neurological disorders *in vitro* (Logan *et al.*, 2019). The use of hiPSCs allows the development of more relevant human models as well as avoiding problematic ethical issues raised when using human embryonic stem cells (hESCs). Furthermore, a focus on more relevant human tissues can lead to a reduction in the number of animals used for research.

However, with all its advantages, *in vitro* cultures also have disadvantages, probably the most significant being a complete lack of normal neural architecture. Thus, the development of shaping technology to provide a more *in vivo* like environment can be seen as a critical technology in neuroscience. The simplest of these shaping technologies deploys chambers connected by microchannels. These techniques were first deployed in the late 1970s where a three-chamber compartment to spatially control neuronal development was reported (Campenot, 1977). Since then, chambers with regular

microchannels have been developed using soft lithography to study axonal growth by following their growth through microchannels measuring only a few microns in width (20 μm wide, 3 μm height and 10,000 μm in length) (Park *et al.*, 2014).

The research in this thesis focuses on developing and fabricating MEAs as well as microfluidics microchannels that will be combined with the cultures of hiPSCs and animal primary cultures to form integrated biochips to study neurons of the CNS. Ultimately such biochips can be used to study different neurodegenerative diseases like multiple sclerosis (MS) allowing for new *in vitro* models to be created. As MS occurs due to the breakdown of myelin and its failure to remyelinate (Gruchot *et al.*, 2019), integrated biochips could be used to study neurodegeneration. Currently, most studies use MEAs and microfluidics separately to investigate myelination, demyelination and remyelination. Combining these three technologies will enable the study of diseases such as MS in unprecedented detail.

This introduction (Chapter 1) will provide an overview of the literature in order to allow the reader to understand the background and aims of this research. Later, I will detail the process of manufacturing, developing and testing custom MEAs and microchannels followed by their fabrication (Chapter 2). Fabricated MEAs and microchannel functionality will be assessed with human neural stem cell (hNSC) cultures that were later differentiated into cortical and dopaminergic neurons (Chapter 3) as well mouse spinal cord cultures (Chapter 4). Electrical activity recorded over time will be detailed as well as the developmental progress and maturation of these cultures. The data obtained will allow a robust understanding at what stages of these cultures electrical maturation and synaptogenesis occurs. In the primary mouse cultures the process of myelination by measuring electrode-to-electrode conduction velocity is investigated (Chapter 4). Finally, the experimental results of these chapters allow us to draw near to answering the question posed in this introductory chapter: Are MEAs combined with microchannels suitable for *in vitro* modelling neurodegenerative diseases and can human cells be incorporated in such systems?

1.2 Neurodegenerative Diseases

1.2.1 Prevalence and Pathophysiology

Neurodegeneration is a phenomenon that occurs in the central nervous system (CNS) which involves the dysfunction and destruction of neurons and glial cells (Dugger and Dickson, 2017). Examples of a few prominent neurological diseases caused by neurodegeneration include Alzheimer's disease (AD), Parkinson's disease (PD), multiple sclerosis (MS) and motor neuron disease (MND). The pathologies caused by the degenerative processes are diverse in their pathophysiology with a variety of symptoms such as memory loss and cognitive impairment (AD) (Canter, Penney and Tsai, 2016) as well as affect mobility, speech and breathing (MND) (Taylor, Brown and Cleveland, 2016).

These disorders are a major and increasing threat to human health, and are becoming more prevalent globally due to the increase in the demographics of elderly populations (Przedborski, Vila and Jackson-Lewis, 2003). One way to understand the burden neurological disorders have on society is by looking at the disability-adjusted life-years (DALYs) which is a measurement obtained by the sum of years lived with disability and years of life lost. The DALY for neurological disorders is estimated to be one of the highest worldwide and measures at approximately 276 million, which attributes to 11.6% of global DALYs for all diseases. Neurological disorders were the cause of about 9 million deaths worldwide in 2016, which equated to 16.5% of total global deaths, second behind cardiovascular diseases (Feigin *et al.*, 2019).

There are currently no cures for neurodegenerative diseases and the treatments available only serve to improve the patient's quality of life by managing the symptoms or halting the progression of the disease (Durães, Pinto and Sousa, 2018). Therefore, it is important to find new treatment methods that may eventually lead to cures. In order to do this, we must better understand what causes them to progress and the underlying pathological mechanisms which due to obvious ethical constraints in humans are currently lacking. For example, it is known that certain neurodegenerative diseases occur due to the abnormal build-up of proteins in the brain or tissue, like β-amyloid accumulation in AD (Wisniewski *et al.*, 1989), α-synuclein accumulation in PD (Takeda *et al.*, 1998) and β-amyloid and Tau accumulation in MS (Gehrmann *et al.*, 1995).

1.2.2 Parkinson's Disease

Parkinson's disease (PD) is the second most prevalent neurodegenerative disease after AD and is characterised as a movement disorder. It was estimated that 6.1 million people suffered with PD worldwide in 2016, which was a substantial increase when compared to 2.5 million recorded in 1990. PD is slightly more likely to occur in males than females as within those 6.1 million cases, 52.5% were men and 47.5% female. Prevalence of PD is uncommon before the age of 50, however, its prevalence increases with age and peaks between the ages of 85 and 89 (Ray Dorsey *et al.*, 2018). There is currently no cure, however, available treatments help manage the disease and improve the quality of life of PD patients. These treatments include dopamine substitution and deep brain stimulation that help reduce motor and non-motor symptoms (Poewe *et al.*, 2017).

PD was first explained by James Parkinson more than two hundred years ago in his essay on 'the shaking palsy' (Parkinson, 1817). He studied 6 cases where he noted individuals expressing symptoms such as agitated extremities, interrupted speech, bowed body and total inability of walking. Most of his observations are valid until now. However, since then we have obtained a better understanding in what causes PD, but we still have a lot to understand as there is still no cure for it. PD is characterised by the death of dopaminergic neurons in the substantia nigra part of the brain and the accumulation of the presynaptic α-synuclein within neurons and glia (Poewe *et al.*, 2017). Studies based on animal models show that the loss of dopamine producing neurons is triggered by the accumulation of α-synuclein (Dzamko, Geczy and Halliday, 2015). Therefore, it is known that cells with aggregated α-synuclein, known as Lewy's bodies, play a significant role in PD.

A model based on brains obtained at autopsy of patients clinically diagnosed with PD (Braak *et al.*, 2003), showed that PD begins in the medulla and olfactory bulb (stages 1 and 2) which associates with non-motor symptoms such as rapid eye movement sleep disorders and reduced sense of smell. As the disease pathology progresses, lesions are observed in the midbrain, specifically in the substantia nigra (stage 3 and 4). This is the stage at which PD is diagnosed and is the stage at which patients show motor symptoms such as tremors and bradykinesia. The final stages 5 and 6 of the pathology include the severe cases which show additional deterioration of the neocortex (**Figure 1.1**) (Braak *et al.*, 2003). Another model used for pre-clinical testing of new treatments is based on the

in vivo study of neurotoxic lesions caused by dopaminergic neuron toxins. It involves the exposure of mice and primates to 6-Hydroxydopamine (6-OHDA) and 1-methyl-4-phenyl-1,2,3,6-tetrahydropyridine (MPTP) which produce PD like effects to be observed such as substantia nigra cell death and typical PD symptoms in the animals. However, the typical Lewy body formations observed in humans are not reproduced in these animal models. (Tieu, 2011).

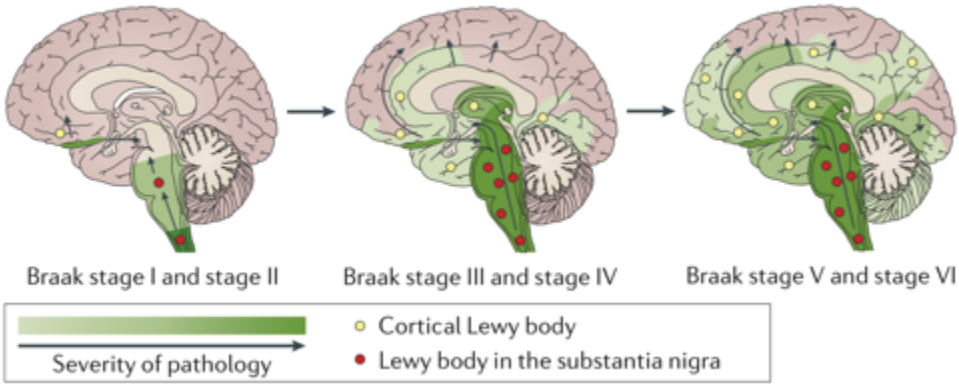

Figure 1.1: The progression of pathology in Parkinson's disease. In the early stages of PD (stages 1 and 2) α-synuclein aggregations are present in the medulla oblongata and olfactory bulbs. Motor symptoms begin to present themselves at stages 3 and 4, where lesions are found in the midbrain, substantia nigra. The final and most severe cases of PD are stages 5 and 6 where lesions spread to the neocortex (from Poewe *et al.*, 2017).

1.2.3 Multiple Sclerosis

1.2.3.1 Prevalence of MS

Multiple sclerosis (MS) is the most common chronic neuroinflammatory disease that affects the CNS. Worldwide, the estimate of people living with MS is about 2.2 million (Wallin *et al.*, 2019). In the UK alone it is estimated that there are over 130,000 people living with MS, with Scotland having the highest prevalence and incidence rates (MS Society, 2020). Incidence and prevalence studies carried out over the last few decades indicate that women between the ages of 20 and 40 are more prone to be affected by MS when compared to men (Inglese, 2006). The ages at which people are most likely to be diagnosed with MS are between 40 and 50 years (Mackenzie *et al.*, 2014). MS is not fatal but it dramatically reduces the quality of life of the people affected by it. The symptoms that arise from MS vary from person to person. The most common symptoms include

fatigue, loss of mobility, spasticity and cognitive decline (Feinstein, Freeman and Lo, 2015).

1.2.3.2 MS Subtypes

MS has been categorised into four distinct clinical phenotypes and these terms have been used since their proposal in 1996. The four categories are: relapsing-remitting (RRMS), secondary-progressive (SPMS), primary progressive (PPMS) and progressive relapsing (PRMS) (**Figure 1.2**) (Lublin and Reingold, 1996). RRMS is the most common (85%) form of the disease and it is characterised by sudden onsets of symptoms that occur for a few days to months followed by periods of full recovery that are also variable in length. After roughly 25 years, RRMS patients often transition into the SPMS form of the disease where there is a steady decline of their symptoms and will no longer experience periods of remission (Weinshenker *et al.*, 1989). Approximately 10% of patients fall in the PPMS course of the disease in which patients experience a steady decline and a worsening of their symptoms from the onset of the disease (Antel *et al.*, 2012). The final and least common form is PRMS, which is characterised by a steady increase of symptoms from the onset but with exacerbation periods and no periods of recovery (Inglese, 2006).

These classifications are useful from a theoretical standpoint. However, in clinical practice they are unable to capture the complexity of the disease as the transitions between RRMS and SPMS is unclear and also patients are placed in these categories based on their recollection and description of when their symptoms have occurred. Furthermore, all the MS phenotypes share common characteristics and there is currently no clinical or imaging characteristics that allow for clear differentiation between them.

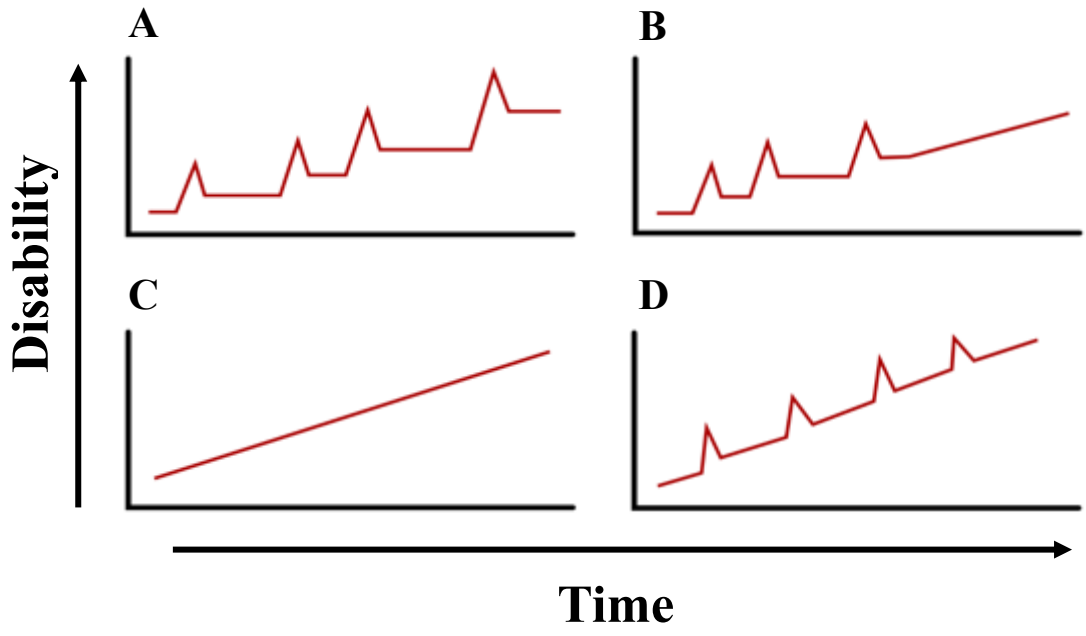

Figure 1.2: Four clinical phenotypes of multiple sclerosis. (A) Relapsing-remitting (RRMS) which is the most common. **(B)** Secondary-progressive (SPMS) is the form in which a RRMS patients will enter after about 25 years of having MS. **(C)** Primary progressive (PPMS) affects about 10% of MS patients. **(D)** Progressive relapsing (PRMS) is the least common form and the worst of the four (adapted from Jacobs, 2016).

1.2.3.3 MS Pathophysiology

In order to gain more knowledge about MS and its pathology, donated post-mortem brain tissue of patients have been studied. This pathology consists of plaques of inflammatory demyelination in the CNS in combination with inflammatory infiltrates, such as T cells and B cells, activated macrophages/microglia and axonal damage (Kutzelnigg and Lassmann, 2014). These plaques are not only observed in the white matter but are also present in the grey matter. MS lesions are highly variable from one patient to another with respect to axonal damage, inflammation and oligodendrocyte pathology (Lassmann, Brück and Lucchinetti, 2001).

Neuroaxonal injury has not only been observed in acute and chronic plaques but also in normal appearing white matter (Trapp *et al.*, 1998). Axonal loss is variable but may reach up to 70% when compared to healthy spinal cord and brain tissue (Lovas *et al.*, 2000). This form of axonal damage observed in MS is known as Wallerian degeneration, which

is the process of anterograde degeneration of the distal part of the axon that is separated from the cell body (Dziedzic *et al.*, 2010).

The blood-brain barrier (BBB) restricts the transfer of cells, such as leukocytes, from the blood into the CNS. In MS, the BBB fails to restrict access to leukocytes and they therefore are able to enter and interact with other cells in the CNS. It is not clearly understood how the BBB changes to allow this but it is hypothesised that these changes in the vascular endothelium could be due to the presence pro- inflammatory cytokines such as tumor necrosis factor (TNF) (Wu and Alvarez, 2011). The presence of leukocytes, such a T cells and B cells, in the CNS trigger an inflammatory response, which alters the structure of the myelin sheath significantly and therefore leads to demyelination (Vassall, Bamm and Harauz, 2015).

1.2.3.4 Myelin

Myelin is an electrically insulating membrane of great importance whose dry mass consists of mostly lipids, at approximately 80%, with the remaining being proteins such as myelin basic protein (MBP) and proteolipid protein (PLP). Myelin forms a tightly packed multi-layered sheath around axons, which aids in the faster conduction of action potentials (Aggarwal *et al.*, 2013). This myelin sheath was first observed about 300 years ago by Antonie van Leeuwenhoek (Schierbeek, 1953) but did not gain its current name for another 150 years since it was first observed. Rudolf Virchow first described this "medullary substance" that was found inside the hollow cavity of axons and hence gave it the name "myeline" as an analogy to bone marrow from the Greek 'myelos' ('marrow') (Virchow and Chance, 1860). Since then, the availability of new technologies and techniques such as electron microscopy, immunocytochemistry and electrophysiology has greatly improved our knowledge of the myelin sheath.

We now know that the myelin sheath is dynamic and is formed from glial cells such as oligodendrocytes in the CNS and Schwann cells in the PNS. Oligodendrocytes arise from oligodendrocyte progenitor cells (OPCs) and are responsible for myelination of axons in the CNS. On the other hand, Schwann cells originate from the neural crest and produce the myelin that wraps around axons in the peripheral nervous system (PNS) (Monk, Feltri and Taveggia, 2015). OPCs account for approximately 5% of all the cells in the CNS of an adult (Gautier *et al.*, 2015). Other types of glial cells are also found in the CNS and

these include astrocytes, which are the most abundant, and microglia (Zuchero and Barres, 2015).

To myelinate axons, OPCs are able to proliferate and migrate to the required regions of the CNS. They will then differentiation into myelin-forming oligodendrocytes and begin to form a myelin sheath around the axon (Jagielska *et al.*, 2012). They do this by two coordinated motions where the start of the innermost layer of growing myelin sheath wraps itself around the axon while the remaining myelin membrane forms layers along the axon (Snaidero *et al.*, 2014). The process by which oligodendrocytes choose which axons to myelinate is not clearly understood as of yet but it is known that they are selective towards axons that are at least 0.2μm in diameter (Simons and Trajkovic, 2006).

Recent studies have looked to identify factors that influence differentiation of OPCs and myelination. For example, an *in vivo* study by Azim and Butt, 2011 carried out on rats and mice, has identified that the enzyme glycogen synthase kinase 3β(GSK3β) has a regulatory effect on the proliferation and differentiation of OPCs. Inhibition of GSK3β enhanced the proliferation and survival of OPCs as well as their ability to differentiate into oligodendrocytes and thus promoted myelination via several different mechanisms.

Oligodendrocytes not only form myelin to electrically insulate axons but also offer trophic and metabolic support as well as cause the cluster of sodium channels throughout an axon forming nodes of Ranvier. These nodes are very important as they allow saltatory conduction to occur and therefore facilitate the faster transport of electrical impulses (Bradl and Lassmann, 2010). Therefore, demyelinated axons or axons with partial myelin sheaths result in a reduction of axonal conduction velocity, which compromises the signalling function of the neuronal cells. The nodes of Ranvier not only increase the nerve conduction velocity by 20 to 100 fold when compared to non-myelinated axons but also reduce the energy consumption of neurons (Nave and Werner, 2014). This occurs because the requirement of ATP- dependent Na^+/K^+ exchange in maintaining the resting potential is reduced as the action potentials are constrained to the internodes (Wang *et al.*, 2008).

1.2.3.5 Demyelination

Demyelination in MS (**Figure 1.3**) is caused by the malfunction of myelin-producing oligodendrocytes, which once differentiated from OPCs, are unable to migrate to regions

that require remyelination. In order for remyelination to occur OPCs have to proliferate, migrate into regions of demyelination and differentiate into myelin-producing oligodendrocytes (mature oligodendrocytes) (Aharoni, 2015). Studies have shown that remyelination does occur in MS patients, however the extent at which the layers of compact myelin form are not the same as it was before demyelination occurred. The myelin sheath is thinner and more vulnerable to subsequent damage. This has been reported by calculating the g-ratio, which is the ratio between the diameter of the axon and the diameter of the myelin fibre. Remyelinated axons have a higher g-ratio when compared to their equivalent healthy myelinated axons (Bradl and Lassmann, 2010)

Studies over the last few years have been looking at identifying factors that affect remyelination. One example of such factors is semaphorins which are secreted and trans-membrane proteins. More specifically, class 3 semaphorins have been shown to play a role in remyelination (Jongbloets and Pasterkamp, 2014). It has been identified that semaphorin 3A (Sema3A) blocked the recruitment of OPCs to demyelinated regions. Unlike Sema3A, semaphorin 3F (Sema3F) accelerated the recruitment of OPCs and also increased the rate of remyelination when upregulated (Piaton *et al.*, 2011).

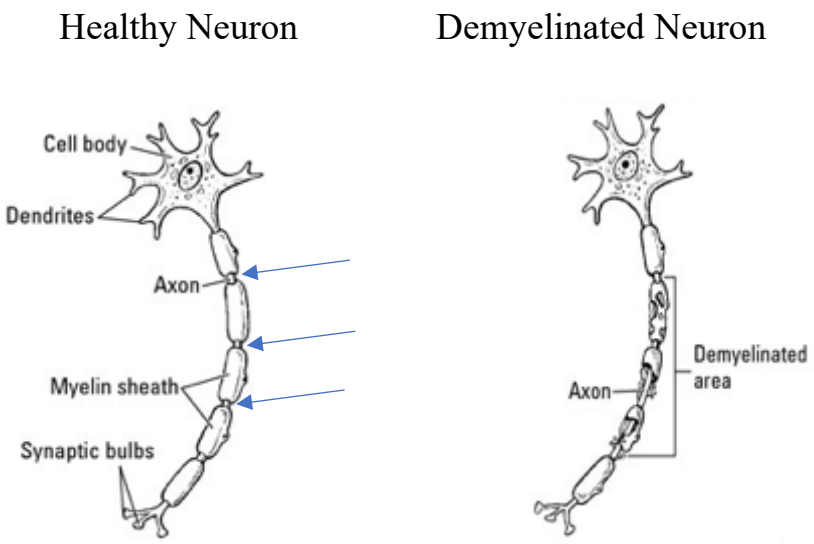

Figure 1.3: Structural changes of neurons in multiple sclerosis. A healthy axon has compacted myelin sheath wrapped around its axon forming distinct nodes of Ranvier (blue arrows). Multiple sclerosis occurs due to demyelination of the axons which lead to the breakdown of the myelin sheath. (Adapted from Kalb, Giesser and Costello, 2012).

1.2.3.6 Animal vs Human Models of MS

Experimental autoimmune encephalomyelitis (EAE) is the most commonly studied animal model for MS and it is thought to be the closest pathology model for MS (Franklin, 2015). Over the years, it has helped us better understand the mechanisms of MS as well as test and develop drugs to treat MS patients (Farooqi, Gran and Constantinescu, 2010). During the past few years, several other animal models have been developed, however, their outcomes do not always reflect what would happen when compared to a human MS patient. This is due to the fact that there several differences between human and rodent oligodendrocytes.

Some regions of rodent brains are underdeveloped when compared to human brains. For example, mice, unlike humans, totally lack the neocortical regions. Also, the opposite applies as the olfactory bulbs are much less developed in humans when compared to mice (Jakovcevski *et al.*, 2009). Another difference is that the numbers of oligodendrocytes present in the human brain are greatly increased when compared to those found in mice. Also, gliogenesis occurs postnatally in mice whereas in humans it occurs during gestation (Craig *et al.*, 2003). Finally, the time it takes for myelination to occur is another key difference. In humans it takes decades due to the complexity of the brain whereas in mice myelination only takes about 2 weeks (Semple *et al.*, 2013). However, there are some similarities between humans and rodents, which include that both their OPCs show similar responses to growth factors, such as platelet-derived growth factor (PDGF) (Wilson, Onischke and Raine, 2003).

The fact that there are so many differences between human and rodent models indicates the importance of developing human *in vitro* models that will be able to output more human relevant results. A possible solution to this is that since the discovery of human embryonic stem cells (hESCs) about two decades ago (Thomson *et al.*, 1998) and more recently human induced pluripotent stem cells (hiPSCs) (Takahashi and Yamanaka, 2006), together with their commercial availability, has allowed researchers to use human cells to develop novel models that will potentially improve our understanding of the diseases process to improve clinical tests and allow more targeted drug discovery.

1.2.4 Induced Pluripotent Stem Cells

Rather than using complex and possibly divergent animal models for disease process studies, the availability of human tissues/cells could advance understanding by enabling relevant experiments *in vitro*.

The discovery of hESCs, has generated great interest in developing new cell lines that would have a similar function to human primary cells such as neurons and glia. However, hESCs have associated ethical problems with their use relating to the destruction of human embryos (Di Ruscio *et al.*, 2015). Takahashi and Yamanaka, 2006, were able to address this as they discovered a method to reprogramme adult fibroblasts into induced pluripotent stem cells (iPSCs) by introducing four transcription factors, Oct3/4, Sox2, c-Myc and Klf4 to the cultures.

Protocols are now available to differentiate human iPSCs into almost any cell type and therefore studies have utilized them to differentiate them into human neural stem cells (hNSCs). These hNSCs, also referred to as neural progenitor cells, can be further differentiated into any neuronal cell line, for example, dopaminergic neurons, cortical neurons, motor neurons and glial cells (Selvaraj *et al.*, 2012). Therefore, iPSCs can be used for developing novel human *in vitro* models, as well as used in transplantation therapies of which they offer an advantage over hESCs as they will not induce a post-transplantation immune response because they are derived from the patients' cells (Goldman and Kuypers, 2015).

The time it takes to differentiate into each specific neuronal cell varies between each protocol. For example, differentiating into cerebral cortical neurons takes about 3 to 10 days (Axolbio, 2016) and differentiating into dopaminergic neurons takes 14 days (STEMCELL Technologies). These differentiation protocols are fairly short in comparison to that of glial cells. A protocol published by Wang et al., 2013 described the process in which they differentiated human iPSCs into oligodendrocytes over a period of 4 to 5 months. Since then a more recent protocol has been published that has halved the time (75 days) to generate human oligodendrocytes from iPSCs (Douvaras and Fossati, 2015).

The availability of such protocols, even though time consuming and expensive, opens the possibility of further studies to utilise the use of human neurons and OPCs to investigate remyelination, which will directly relate to humans and not rodents. There have already been studies that have demonstrated *in vivo* myelination in the shiverer mouse following the transplantation of human OPCs differentiated from iPSCs (Douvaras *et al.*, 2014).

1.3 Microelectrode Array Technology

Studying the function and connectivity of neurons in the brain involves interdisciplinary efforts and technological development which through the years have led to advances in genetic markers, immunostaining, electrophysiology and computational tools. These advances have allowed the identification of neuronal cell types and their functions in different regions of the CNS. At the core of this technology is the basic fact that the main functional substrate of the CNS is its wet bioelectricity which enables it to function as a massive parallel supercomputer. Thus, to get a better understanding of the brain's complexity and pathology, innovative technologies require the measurement of electrical potentials over a wide field and in as much detail as possible.

At the microscale, patch clamp can measure currents of single ion channels and carry out direct measurements of the intracellular voltage. While patch clamp is a powerful but exacting method (as not many neurons can be studied per experiment) (Wood, Williams and Waldron, 2004) it gives unprecedent detail with poor spatial resolution. At the macroscale, measurements can be obtained from large areas of the brain's activity using techniques such as electroencephalography (EEG) which can detect electrical activity from the scalp with centimetre range spatial resolution (Obien *et al.*, 2015) and can be equivalent to imaging large areas of the brain at high resolution.

Microelectrode arrays (MEAs) offer a solution to the poor spatial resolution but as they only measure electrical potential a little detail is lost. They can be deployed to measure electrical activity *in vivo* and *in vitro*. The first MEA *in vitro* recordings were done on chick cardiomyocytes in 1972 (Thomas *et al.*, 1972). The MEA was fabricated using 25 mm glass coverslips and consisted of 30 platinum black electrodes, arranged in two rows 50 μm apart and the interelectrode distance between rows was 100 μm (**Figure 1.4A**). For insulation a photopolymer layer was coated over the surface. A few years later, the first extracellular recordings from dissociated neuronal cultures were recorded on an

MEA. Dissociated cells from superior cervical ganglia of neonatal rats were cultured a glass coverslips that had 32 gold electrodes, in two horizontal groups of 16 at a 250 μm interelectrode distance with a silicon dioxide insulating layer (Pine, 1980).

1.3.1 Types of MEAs for *in vitro* Applications

Since those early arrays in the 1970s, MEAs have developed into having a variety of different features as well have thousands of electrodes. Most common MEAs have planar electrodes arranged uniformly with a set interelectrode distance and are used for *in vitro* cell culture analysis. An example includes the 60Standard MEA (**Figure 1.4B**) offered by Multichannel Systems (Reutlingen, Germany) which consists of 60 electrodes (59 recording and 1 internal reference electrode) in an 8 x 8 layout grid with two options for electrode diameters (10 and 30 μm) and two options for interelectrode distances (100 and 200 μm). The electrodes are made of titanium nitride (TiN) and the insulating layer is made of silicon nitride (Si_3N_4). Three dimensional MEAs are also commercially available that are ideal for studying brain slices as protruding electrodes can be fabricated that penetrate dead cell layers and therefore allow interfacing and recoding from healthy cells. A 60-3DMEA from Multichannel Systems (**Figure 1.4C**) consists of 60 TiN electrodes (59 recording and 1 internal reference electrode) arranged in an 8 x 8 grid with interelectrode distances of 100, 200 or 200 μm. The electrodes are 20 μm high, have a base diameter of 100 μm and a tip diameter of 12 μm. Another type of MEA offered by Multichannel Systems is a highly dense 256ThinMEA (**Figure 1.4D**) which contains 252 TiN electrodes and four ground electrodes in a 16 x 16 grid. The versions available offer electrodes of diameter 10 or 30 μm and interelectrode distances ranging between 30 to 200 μm. The electrodes are embedded in a 180 μm thick glass substrate making them ideal for high-resolution imaging.

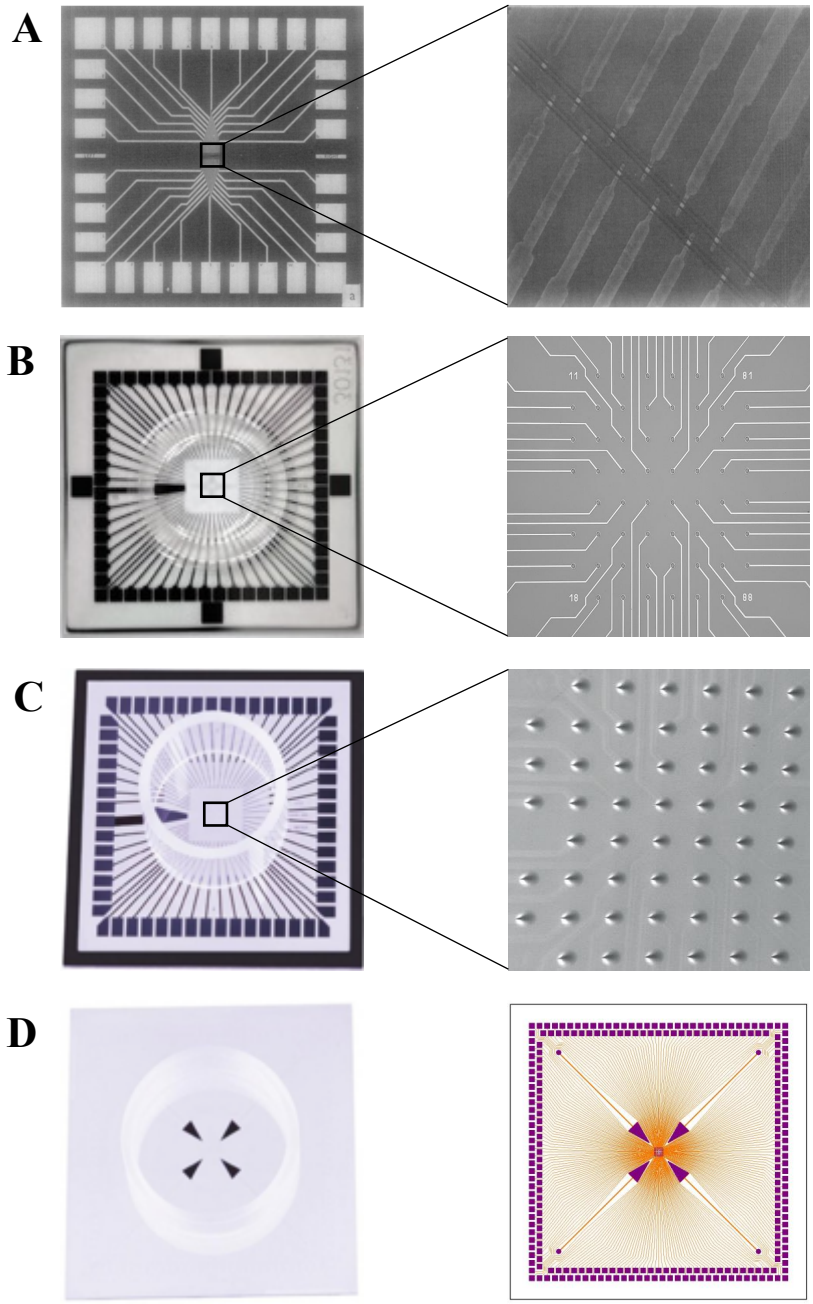

Figure 1.4: Different types of microelectrode arrays. (A) First MEA used for measuring electrical activity from dissociate cell cultures (Thomas *et al.*, 1972). Right panel shows a magnified view of the electrode arrangement. **(B)** Standard 60MEA with 59 planar recording electrodes and one internal reference electrode. Right image shows a magnified view of the electrode layout in the centre of the MEA. **(C)** An example of an MEA with 3D electrodes (right image) arranged in the same way as those of the standard 60MEA**. (D)** High density MEA consisting of 256 electrodes of which 4 are the ground electrodes (visible as arrow heads in left image). (From Multichannel Systems, 2015).

1.3.2 *In vitro* Neuronal Cultures and MEAs

Combined with immunostaining, MEAs have been used to study and identify neuronal types, analyse electrical activity in long term cultures and follow synaptogenesis. Examples include the use of MEAs to study excitatory and inhibitory synapses in long term culture of rat cortical neurons for up to 35 days *in vitro* (DIV) (Ito, Komatsu and Gohara, 2013). This study used antibody staining against vesicular glutamate transporter 1 (VGluT1) and vesicular transporter of γ-aminobutyric acid (VGAT) to investigate the distribution and densities of glutamatergic and GABAergic synapses which they then compared to the electrical recordings obtained from the MEAs. They found a correlation between synaptic densities and electrical activity as an increase in glutamatergic and GABAergic synapses was accompanied with an increase in electrical activity from 7 DIV and reached a plateau after 28 DIV which was when synapses reached their final mature state.

With advances in lithographic techniques, researchers began fabricating their own custom MEAs in order to adapt the electrode layouts to fit the experimental design and to avoid restrictions imposed by the fixed layouts provided commercially. High density CMOS-based MEAs containing over 11,000 electrodes were used by Bakkum et al., 2013, to investigate axonal action potential propagation by culturing rat cortical neurons on them. One of their measurements included conduction velocity, which ranged between about 0.2 and 1.8 m/s. Based on those measurements they concluded that these velocities were recorded from unmyelinated axons.

1.3.3 Microelectrodes *in vivo*

Microelectrodes are also being used *in vivo* to study the CNS in order to obtain a more detailed use of its neuronal structure and to look at highly localised drug delivery. Microelectrodes for stimulating and recording are aligned at the tip of a probe which is stereotactically placed in a region of the brain (**Figure 1.5**).

High density recording silicon probes (**Figure 1.5B**), of up to 512 channels, have been used to study the electroanatomical boundaries of layers and regions in the hippocampus and neocortex of rats (Berényi *et al.*, 2014). This system allowed the simultaneous recordings of local potentials and the unit activity from hundreds of sites while the animal

could move freely. This was achieved by having ultra-flexible connections and a miniaturised microdrive that allowed the probe to move to the vicinity of the desired regions of the rat's brain.

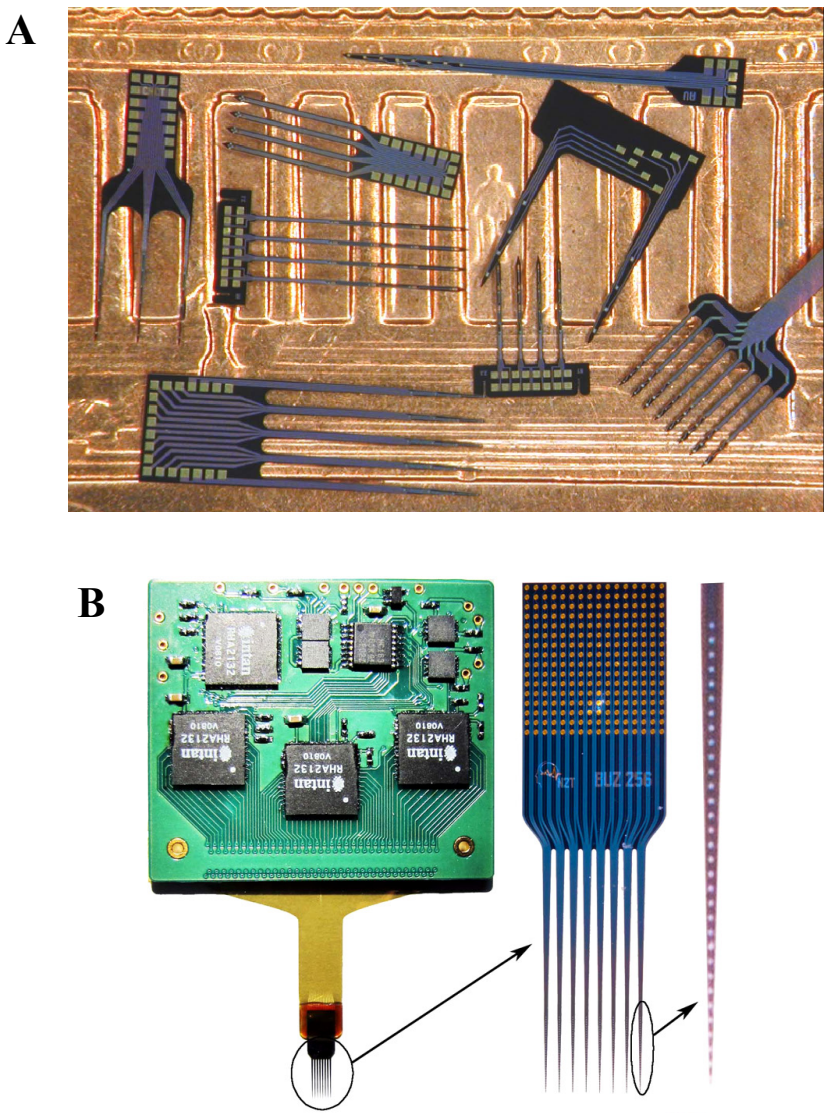

Figure 1.5: Examples of several probes with a series of microelectrodes for *in vivo* use. (A) Seven neural probes made from silicon on the back of a U.S penny fabricated by the University of Michigan. **(B)** High density silicon probe connected to a printed circuit board via a flexible ribbon cable that can transmit from 256 channels. Microelectrodes are embedded in the probes as indicated by the arrows (from Berényi *et al.*, 2014).

1.4 Microfluidics

Microfluidics, or mini labs-on a chip, have become very popular over the last few decades. Microfluidics allows delivery of drugs, solutions or reactive mixtures to be delivered faster, with smaller volumes of substrates and can be used to produce isolated chemical environments similar to those found in the human body (Park *et al.*, 2012). This type of system has also been extensively used to study and model the nervous system by constraining neurons to grow in a more neuro-architectonically valid orientation. Campenot, 1977 first introduced an *in vitro* three compartment device (**Figure 1.6A**) that separated neuronal cultures with localised fluidic control. Dissociated neurons from super cervical ganglia of newborn rats were cultured in the central chamber and neurite growth was guided into either of the other two chambers by adding nerve growth factor (NGF). Neuronal growth was guided into the chambers as growth was only observed along the 200 µm tracks formed between the collagen scratches previously done using insect pins. Growth was not found to not cross over the scratches. Recent studies still utilise these Campenot style chambers to study axon-glia interactions (Park *et al.*, 2009). However, the chambers are connected with much more precise features as the microchannels measure 15 µm in width and are separated by 60 µm (**Figure 1.6B**). The ability to fabricate micron level features has arisen due to the introduction of photolithography (**Figure 1.7**).

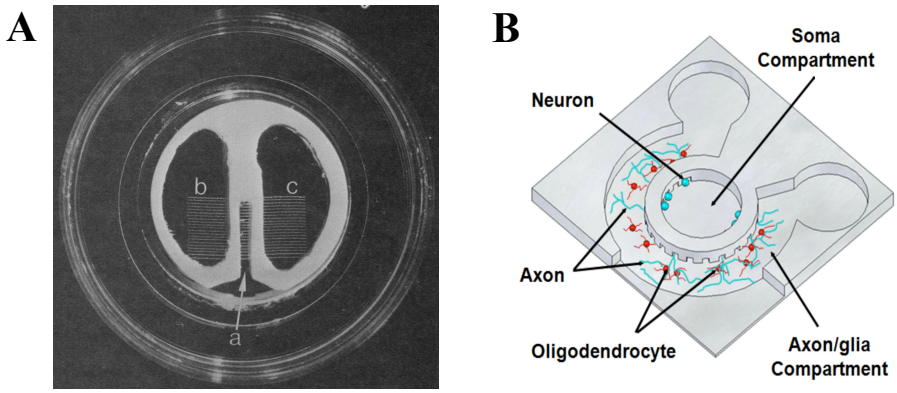

Figure 1.6: Chambers for neuronal growth control and guidance. (A) Campenot chamber made up of three compartments labelled a, b and c. Dissociated neurons were cultured in chamber a and NGF was added into the other chambers b and/or c. Neuronal growth was only observed in the chambers that had NGF and growth was observed to occur within the etched channels (from Campenot, 1977). **(B)** A more recent compartmentalised microfluidic device that was based off Campenot. Neurons were cultured in the middle soma compartment and oligodendrocyte were added in the surrounding compartment where they could only interact with axons that grew through the 15 µm microchannels (from Park *et al.*, 2009).

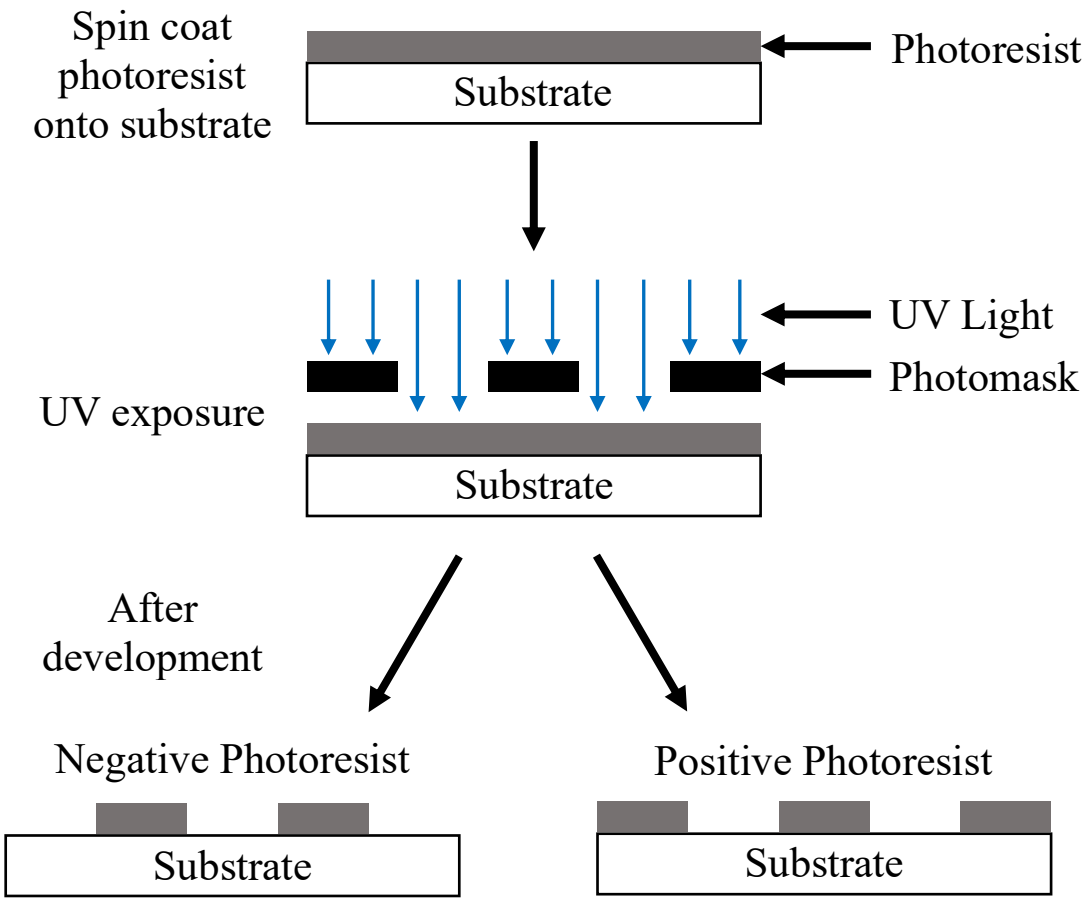

Figure 1.7: Photolithography process for fabricating microchannels. In order to fabricate microfluidic channels, a 'mold' has to be created called the master wafer. The microfluidic design is on the photomask and depending on if a negative or positive photoresist is used its design will be transferred onto the master wafer.

Depending on what is investigated, microfluidic devices are fabricated with a different number of compartments. A study by Coquinco *et al.*, 2014 designed and fabricated a microfluidic device with three compartments to study synaptic competition *in vitro* using rat cortical neurons. Neurons in each compartment were treated in a different way. They found that treating neurons in one of the compartments by inhibiting synaptic input activity using muscimol ($GABA_AR$ agonist) caused the increase in synapse number and axon elongation of the neurons cultured in the opposing un-treated chamber (**Figure 1.8**). Another study investigated nerve injury by culturing rat CNS neurons in a two-compartment microfluidic device where the cell body remained in the first compartment and axons grew through microchannels and into the second compartment in localised chemical treatments were applied to study axonal regeneration using myelin inhibitors such as NOGO-66 and myelin associated glycoprotein MAG (Park *et al.*, 2008).

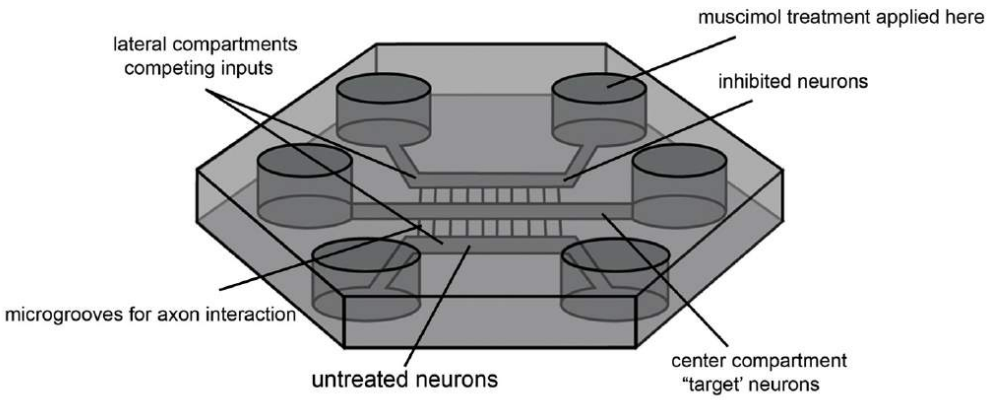

Figure 1.8: Illustration of 3 compartment microfluidic design used to study synaptic competition. Wells are connected to 3 separate compartments in which rat CNS neurons are cultured. Myelin inhibitors are added in the wells of one of the compartments and any effects in synaptic and axonal growth of the neurons in the other 2 compartments are observed (from Coquinco *et al*., 2014).

1.5 MEA and Microchannel Integration

As electrodes on MEAs are spatially fixed it means that electrical activity recorded from neuronal cell cultures is random and it depends on the proximity of the cells to the electrode. This means that if no cells grow over an area of electrodes then that region becomes redundant. This issue can be resolved by encouraging neuronal growth over the available electrodes by guiding growth using the aforementioned microfluidic channels.

Feber *et al*., 2015 designed and fabricated a two-compartment model that interfaces with a custom MEA where one compartment was used for stimulation and the other for recording. They also modified the microchannels in order to improve the unidirectional growth of axons by adding barbs throughout the channels. This prevented axons in the recording compartment from growing back into the stimulating compartment and therefore affect the electrical recordings.

Another more recent study used custom MEAs with integrated microchannels (**Figure 1.9**) to investigate the effects of myelinated and unmyelinated Schwann cells (SCs) have on axonal conduction (Sakai *et al.*, 2017). The microchannels were aligned over indium tin oxide (ITO) electrodes and measured 50 µm in width, 6 µm in height and 2000 µm in length. Dorsal root ganglia (DRG) neurons and SCs were cultured for up to 32 DIV. The compared three different cultures, neuron mono-cultures, neuron/SC co-cultures and neuron/SC myelin cultures by measuring conduction delays between 12 and 32 DIV. It

was found that the conduction delay was reduced in neuron/SC co-cultures between 12 and 27 DIV. The results were not as conclusive for the neuron/SC myelin culture as there was a large variance of the measurements.

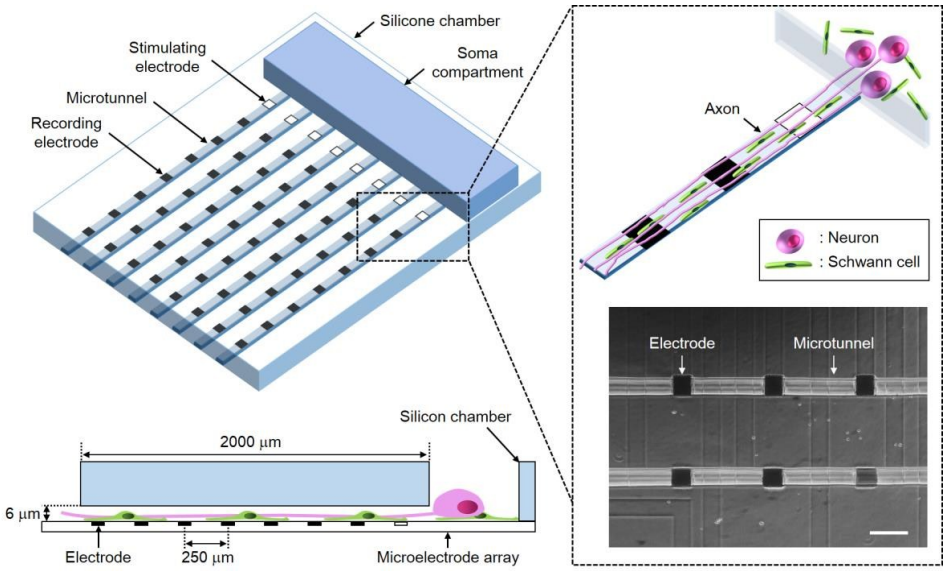

Figure 1.9: Illustrations of microtunnels aligned over electrodes of custom MEA. DRG neurons are seeded in the soma compartment, which only allows axonal growth through the microchannels that are seeded with Schwann cells. Each microtunnel is aligned over 8 electrodes, 1 stimulating (white) and 7 recording (black) electrodes. Scale bar = 100 µm. (From Sakai *et al.*, 2017).

Using microfluidic devices with integrated electrodes is a very important advancement in studying neurodegenerative diseases such as MS. These devices allow the measurements of neuronal conduction velocities, which as mentioned previously, are an indicator of how thick and compact the myelin sheath is (Jakovcevski *et al.*, 2009). Myelin can be identified by investigating the expression of myelin markers, such as MBP. However, this alone is not a reliable indicator as it does not show if the axon is properly ensheathed with myelin because MBP is not only expressed by compact myelin but also by early myelin. Measuring conduction velocity will accurately chart the progress of myelination *in vitro* as myelin matures the conduction velocity will be faster. Therefore, measuring conduction is potentially a more reliable, accurate and repeatable way to investigate demyelination and remyelination and can enhance already available techniques.

1.6 Research Aims

The research performed in this thesis has focused on developing a biochip that could be used to study human and mouse neuronal cultures *in vitro*. The biochip developed would have the ability to be used in developing novel *in vitro* models for diseases like multiple sclerosis. In order to achieve this the following had to be accomplished:

1. Design and fabricate functional custom microelectrode arrays.
2. Design and fabricate microfluidic microchannels.
3. Culture and differentiate human neural stem cells on custom microelectrode arrays and microchannels.
4. Measure conduction velocity from myelinating cultures.

Using MEAs with microchannels requires smaller volumes for culture when compared to standard petri dishes/wells, and therefore fewer cells due to the smaller surface area. This means that animal usage is reduced for investigations. Replacing animal cells with human neuronal cells completely eliminates the use of animals which was the ultimate goal of my thesis. Another advantage of MEAs is that they allow for real-time electrical recording and manipulation of neuronal cell cultures at any given moment and over long periods of time. Similarly, microchannels play an important role in the biochip as the cultures can be spatially segregated and therefore better mimic the cells environment in the human CNS and PNS. The ability to measure the conduction velocity throughout the culture period using MEAs should allow for a more accurate and novel method for assessing myelination *in vitro.* For example, an increase in conduction velocity could be an indicator that myelination is occurring and the myelin sheath is becoming more compact, which other techniques like electron microscopy cannot assess in real-time.

Chapter 2

Development and Fabrication of Recording Device, Microelectrode Arrays and Microchannels

Abstract

Microelectrode arrays (MEAs) have revolutionised our ability to examine brain activity *in vivo* and *in vitro* in real time across hundreds of electrodes, giving unprecedented insight into neuronal network function. The addition of microfluidics to deliver drugs and shape neuronal growth holds the promise of coupling such measurements with biochemical and pharmacological experiments. As a step towards this goal, I constructed a customised system to measure neuronal activity in real time that could incorporate both commercially available and custom MEAs and microfluidic modules. I developed methodologies to rapidly fabricate MEAs from design to useful end product. The final version of custom MEAs had a layout with both stimulating and recording electrodes to enable the study of neurodegeneration and myelination through activity analysis and evoked conduction velocity measurement. To complement the custom MEAs, microfluidic microchannels were modelled, designed and fabricated using several methodologies and aligned over the stimulating and recording electrodes. The purpose of the microchannels was to provide separate compartments between which relatively long stretches of only axons would grow and where different types of cells could potentially be cultured in either compartment. Therefore, the final product was a custom MEA with microchannels that can be used for a series of high throughout experiments to develop *in vitro* models for diseases such as multiple sclerosis and motor neuron disease.

2.1 Introduction

Microelectrodes arrays (MEAs) have been used over recent years for both *in vivo* (Jensen, Yoshida and Hofmann, 2006) and *in vitro* (Xiang *et al.*, 2007) applications. Their ability to obtain simultaneous extracellular recordings from numerous electrodes means that such arrays can be used to study any excitable biological tissue but also importantly the network activity of multiple excitable units. Some of the *in vitro* applications include studying neural activity of cells found in the central and peripheral nervous systems (Obien *et al.*, 2015; Sperry *et al.*, 2018). Other applications are drug discovery for neurodegenerative diseases (Scelfo *et al.*, 2012) as well as cardiovascular diseases (Melle *et al.*, 2020). Commercially available MEAs have different features to accommodate what needs to be studied. For example, Multichannel Systems provide arrays called "ThinMEAs" with a thickness of 180 µm which are ideal for high resolution imaging. Most common commercially available MEAs feature planar electrodes and these are used when culturing a layer of cells on top of them. Three-dimensional electrode MEAs are also available that are used to study tissue slices, as it is important to penetrate the damaged outer layer (Johnstone *et al.*, 2010). Standard planar MEAs used in *in vitro* cell cultures have a matrix of about 60 electrodes concentrated in the central part of the array with an interelectrode distance of 100 or 200 µm (**Figure 2.1**).

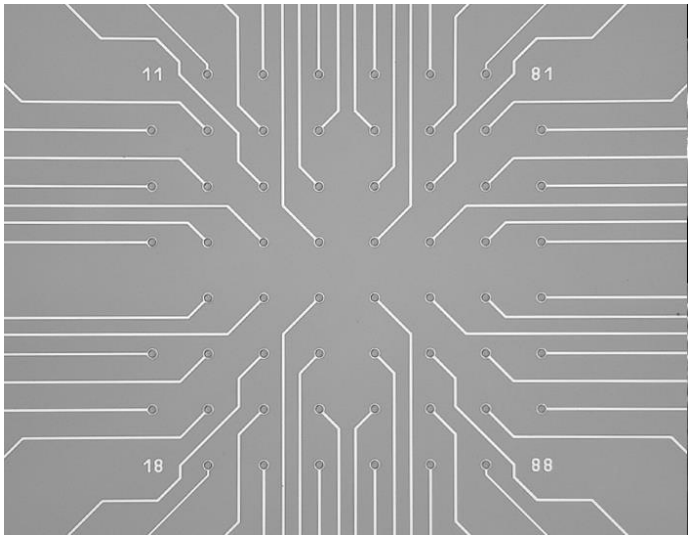

Figure 2.1: **Example of standard microelectrode array (MEA).** Consists of 60 electrodes of which 1 is the reference ground electrode. Different versions of these are available with the differences being the electrode diameters (10 µm or 30 µm) and the interelectrode distance (100 µm or 200 µm). (From Multichannel Systems, 2015).

The ability to manipulate the microenvironment around neurons with microfluidics has been a particularly successful method to couple electrical measurement and pharmacology manipulation in *in vitro* and *in vivo* recordings (Kim *et al.*, 2012; Lee *et al.*, 2015). Microfluidics is a powerful technique to deliver drugs to tissue and has also become very popular over the last few years as it allows to carry out investigations much faster using smaller volumes as well as also produce environments similar to those found in the human body (Achyuta *et al.*, 2013). In *in vitro* scenarios, microfluidics have been successfully used to study axon-glia interactions by culturing neurons and glia in separate compartments and then observing their interaction with time (Park *et al.*, 2009).

Here, both MEAs and microchannels have been designed and fabricated so that it was possible to align the microchannels over stimulating and recording electrodes in an integrated biochip to enable the integration of both technologies in a single module. The aim was to use the biochip to study neurodegeneration in neuronal models (see Chapters 3 and 4). The microchannels purpose was to restrict neuronal cell bodies in a stimulating compartment and allow axonal growth through to a recording compartment. This would be an ideal modality to assess myelination *in vitro* as it would enable calculation of evoked conduction velocity which is an indicator of myelin compactness (Mozafari *et al.*, 2015). As will be reported in the following chapters, although I was unsuccessful in enabling through-channel growth in my biochips, the results here show proof-of-principle and are an important step in enabling this technology,

2.2 Methods

2.2.1 Development of a Flexible System to Record from Microelectrode Arrays

To enable recording from both commercial and custom MEAs, I constructed a flexible lab-built system to monitor electrode activity as commercial array readers are specifically designed for the equivalent MEAs of the manufacturers. Currently there are several different commercially available recording devices, such as the ones offered by Multi Channel Systems (Reutlingen, Germany), Alpha MED Scientific (Osaka, Japan) and Axion Biosystems (Georgia, USA). These devices are capable of recording from 64 to 768 electrodes simultaneously, however, the main issue we faced regarding these was their cost and the fact that the holding module for electrode arrays was fixed and would not allow radical redesign of electrode pads and electrode configurations.

2.2.1.1 Signal Amplification

A Model 3600 amplifier was purchased from A-M Systems (Washington, USA) at a fraction of the cost of commercial array amplifiers. It had a 16-channel capability and eleven gain settings ranging from x2 to x20 000, eight low-pass filters ranging from 100 Hz to 20 kHz, eight high-pass filters ranging from 0.3 Hz to 500 Hz and a notch filter (50 or 60 Hz) per channel. Signals were pre-amplified by a x10 headstage (Omnetics, Minnesota, USA) which was located next to the array and then passed data to the Model 3600 amplifier.

A device to flexibly hold and interface the MEAs to the pre-amplifier headstage was fabricated in the electronics workshop. It consisted of a holding plate and a top plate which contained spring pins (PD8JS-2.2, Coda-Systems, Essex, UK) that had a tip diameter of 1 mm and a working travel of 0.45 mm which were used to interface with the electrode contact pads of the MEAs (**Figure 2.12**). In total three recording devices (RD1, RD2 and RD3) (**Figure 2.10**) were fabricated with the help of the electronics workshop each at different arrangements of spring pins and device to amplifier connections in order to enable recording from all 59 electrodes of commercial MEAs and allow recording and stimulation when using custom MEAs. The pins were connected to the pre-amplifier headstage through a nano strip connector (NPD-18-WD-18.0-C-GS, Omnetics). Each

cable was soldered to one pin with the exception of the ground and x10Ref cables that were both soldered onto the single ground pin.

2.2.1.2 Signal Digitisation

Analogue signals from the amplifier were digitised through a digital data acquisition system (PCIe-6343, National Instruments, Texas, USA). The digital signal was viewed in real-time in Clampex (Molecular Devices, California, USA). All 16 channels could be viewed simultaneously in Clampex.

2.2.2 Design and Fabrication of Custom MEAs

2.2.2.1 Designing of Custom MEAs

The designing of the custom MEAs were carried out using AutoCAD (Autodesk, Inc, California, USA). Throughout the project several different electrode configurations were trialled (**Table 2.1**) and these will be discussed in further detail below

2.2.2.1.1 Epigem MEA Design

The first design, V1.0, can be seen in **Figure 2.2A** which had 16 separate recording electrodes (red), 16 stimulating electrodes (green) that were connected to a single electrode contact pad and 1 ground electrode (dark green). The electrode contact pads measured 2.2 x 2.2 mm and were separated by 200 μm. The diameter for both the recording and stimulating electrodes was 20 μm and 60 μm for the ground electrode. The distance between the stimulating and recording electrodes was 1 mm.

This design was sent to Epigem Limited (Redcar, UK), who were the industrial partner responsible for fabricating and providing custom MEAs for my project. After several iterations of discussions and design, the arrays (**Figure 2.2B**) were received. They measured 49 x 49 mm and were made using poly(methyl methacrylate) (PMMA). The material used for the electrodes, tracks and contact pads was gold. After testing these custom MEAs with cells (detailed in Chapter 3) it was found that cells were not adherent for the prolonged period of time required for neuronal culture. Following issues with peeling off of the tracks after a single use, it was found that all of the electrode tracks

were exposed, and the tracks were not insulated. This meant that these arrays were not able to measure local changes in electrical potential to be detected at the electrodes. Following further discussions with Epigem, it was decided to fabricate the custom MEAs at the nanofabrication facility at Heriot-Watt University because they were unable to fabricate the arrays on any other surface other than PMMA or offer an insulating layer.

2.2.2.1.2 Heriot-Watt University MEA Designs

Several new electrode configurations were then designed in AutoCAD to improve the electrode placement for accurate conduction velocity recordings as well as to have fully functional electrode arrays (**Figure 2.3**). The designs were based on observations made of the axonal lengths of human cerebral cortical neurons (hCCNs) in my differentiated cultures (see Chapter 3).

The design, V2.0, features a total of 16 recording electrodes (red) in 8 groups of 2, separated by 500 µm (**Figure 2.3A)**. The stimulating electrodes (green) were arranged in 2 groups of 4 that horizontally align to the respective recording electrodes. The distance between the stimulating and first recording electrode was 1 mm and 1.5 mm from the second electrode. Both the stimulating and recording electrodes had a diameter of 30 µm. There is a single ground electrode (dark green), measuring 500 x 500 µm situated in between the two groups of recording electrodes.

The design, V3.0 (**Figure 2.3C),** had the same configuration of recording and stimulating electrodes as that of V2.0. However, this time there were 8 ground electrodes connected to one contact pad (dark green) that were aligned parallel to the stimulating and recording electrodes. The stimulating and ground electrodes had a dimeter of 80 µm and were 400 µm apart. The recording electrodes were 50 µm in diameter and the distance between the first recording electrode and ground was 600 µm, which meant it was 1 mm from the stimulating electrode. Also, the distance between the two recording electrodes was kept at 500 µm.

The designs, V3.2 and V3.4 (**Figures 2.3E** and **2.3F)** also featured the same configuration of recording, stimulating and ground electrodes as V3.0. However, some dimensions were altered. The stimulating, recording and ground electrodes had a diameter of 50 µm. The difference between V3.2 and V3.4 was that the ground electrodes were

400 µm and 200 µm apart respectively. The remaining dimensions were kept the same as V3.0.

Finally, design V4.0 had a different configuration of recording electrodes than all the previous ones (**Figure 2.3G)**. It featured 4 sets of 4 recordings electrodes with each being 500 µm apart and each set of 4 was separated by 3 mm from each other. All the electrodes had a diameter of 50 µm. The first recording electrode was 800 µm away from the ground which in turn the ground electrode was 200 µm apart from the stimulating electrode.

The design in **Figure 2.3H** is a representative design for the insulating layer that would be applied on top of the whole electrode array. It only featured the electrode contact pads and the stimulating, ground and recording electrodes with all the tracks absent. All these AutoCAD designs were sent to Micro Lithography Services Limited (Chelmsford, UK) to be made into a film photomask.

Table 2.1: Different designs of custom electrode configurations and layout.

Custom MEA	Stimulating Electrodes	Recording Electrodes	Ground Electrodes	Distance between Stimulating and Recording Electrodes	Distance between Stimulating and Ground Electrodes
V1.0	16 - 20 µm diameter	16 - 20 µm diameter	1 - 60 µm diameter	1 mm	N/A
V2.0	8 - 30 µm diameter	16 - 30 µm diameter. 8 groups of 2 separated by 500 µm	1 measuring 500 x 500 µm	1 and 1.5 mm	N/A
V3.0	8 - 80 µm diameter	16 - 50 µm diameter. 8 groups of 2 separated by 500 µm	8 - 80 µm diameter	1 and 1.5 mm	400 µm
V3.2	8 - 50 µm diameter	16 - 50 µm diameter. 8 groups of 2 separated by 500 µm	8 - 50 µm diameter	1 and 1.5 mm	400 µm
V3.4	8 - 50 µm diameter	16 - 50 µm diameter. 8 groups of 2 separated by 500 µm	8 - 50 µm diameter	1 and 1.5 mm	200 µm
V4.0	4 - 50 µm diameter	16 - 50 µm diameter. 4 groups of 4 separated by 500 µm	4 - 50 µm diameter	1 and 1.5 mm	200 µm

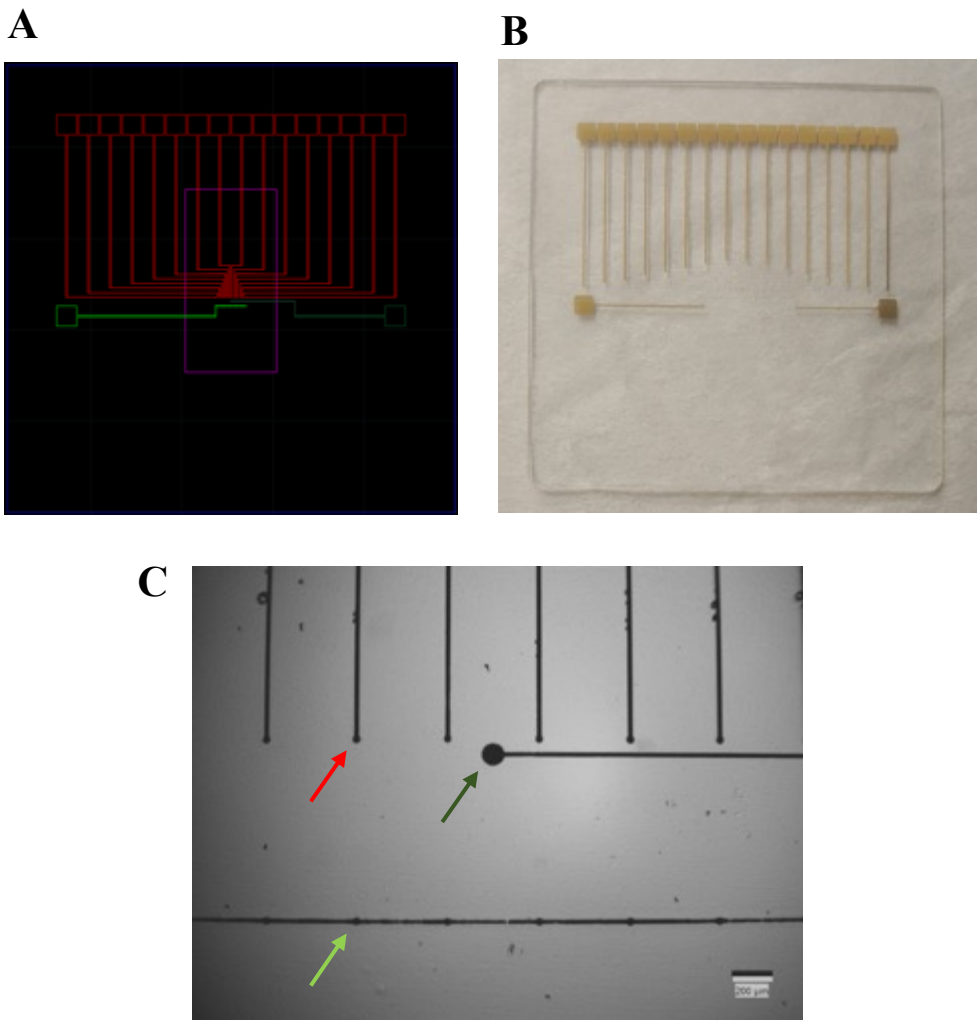

Figure 2.2: First custom microelectrode array design. (A) AutoCAD design showing recording electrodes (red), stimulating electrodes (green) and ground electrode (dark green). **(B)** MEA fabricated by Epigem with gold electrodes on PMMA. **(C)** Microscope image of electrode configuration showing stimulating (green arrow) and recording (red arrow) electrodes with the single ground (dark green arrow) electrode between them. Scale bar = 200 µm.

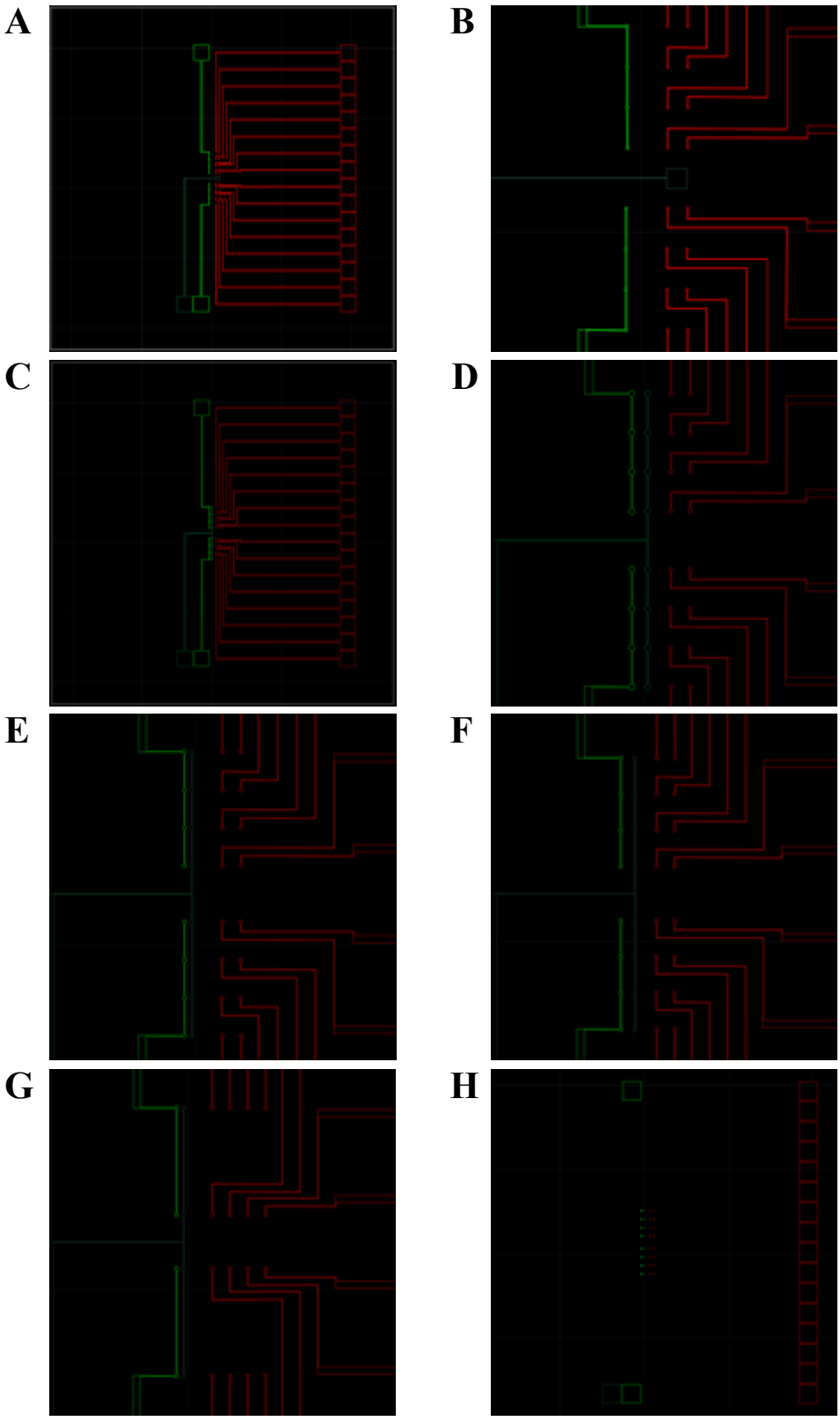

Figure 2.3: Updated custom MEA designs. All images show the recording electrodes in red, stimulating electrodes in green and ground electrodes in dark green. **(A)** Version 2.0 array configuration and **(B)** closer look at the design. **(C)** Version 3.0 array configuration and **(D)** closer look at the design. Closer look at **(E)** version 3.2, **(F)** version 3.4 and **(G)** version 4.0 of the array. **(H)** Design used for the insulating layer, hence the lack of tracks.

2.2.2.2 Fabrication of Custom MEAs

The custom MEAs were fabricated at the Heriot - Watt University nanofabrication facility. Instead of PMMA as the substrate, borosilicate was used. The borosilicate was cut to measure 49 x 49 mm using a DAD3220 Wafer Dicing Saw (DISCO Corporation, Tokyo, Japan) (**Figure 2.5C**). The electrode designs and the insulating patterns were transferred onto the borosilicate using photolithography.

The steps followed for the photolithography process for both the Ti and SiO_2 deposition are detailed below (**Figure 2.4**).

2.2.2.2.1 Cleaning of Substrate

The borosilicate substrate was washed using acetone and diluted Decon 90 (Decon Laboratories Ltd, East Sussex, UK). It was then rinsed with de-ionised (DI) water and blow dried using a filtered air gun. This was done in order to make sure the borosilicate surface was dust free and completely clean before starting the process.

2.2.2.2.2 1st Spin Coating

The borosilicate was then placed onto the spin coater SPIN 150 (SPS Europe, Putten, Netherlands) (**Figure 2.5A**) and was held in place by a vacuum seal. Negative photoresist, AZ nLOF 2070 (MicroChemicals, Ulm, Germany) was carefully placed over the whole surface of the borosilicate making sure to avoid any air bubbles. Once that was done, it was the spun at 3500 rpm for 40 seconds. The negative photoresist used is for forming a 7 μm layer, however, in this case it was diluted to form a 1 μm layer once spun. After this process, the substrate was hard baked at 95°C for 3 minutes.

2.2.2.2.3 Alignment and UV Exposure

The next step involved aligning one of the multielectrode designs film photomask with the prepared substrate. This was done using an MJB3 Mask Aligner (SÜSS MicroTec, Garching, Germany) (**Figure 2.5B**). The film photomask was placed onto the mask holder and was then loaded and secured onto the aligner. The substrate was positioned on the substrate holder that held it in placing using vacuum suction and was then slid under the

photomask. The substrate was brought into contact with the film photomask and then pulled the separation lever in order to be able to align the design with the substrate. The alignment was done by adjusting the x and y axis micrometres. Once the alignment was achieved, the separation lever was pushed back so that the substrate was back into contact with the film photomask. The substrate was then UV exposed for 40 seconds and once that was done the substrate was carefully removed from the mask aligner. A post exposure bake was then carried out at 115°C for 90 seconds.

2.2.2.2.4 Development

The substrate was then developed using the AZ 726 MIF (metal ion free) developer (Microchemicals). It was initially placed in the developer for 60 seconds and was closely monitored for another 15 to 30 seconds until the design features became visible. The substrate was washed in diluted Decon 90 for about 30 seconds, then rinsed with DI water and blow dried with a filtered air gun.

2.2.2.2.5 Electrode Deposition

Once this process was done, it was time to deposit titanium (Ti) onto the substrate. The Ti was deposited by a technique called physical vapour deposition (PVD) using a Minilab 080 (Moorfield Nanotechnology, Knutsford, UK) (**Figure 2.6A-B**). This involved an electron beam directed onto the metal that then evaporates and deposits onto the substrate. The borosilicate substrate was placed into an external chamber with the side to be coated facing downwards. The external chamber had to be degassed, in order to reach the same vacuum levels as the main chamber containing the Ti filled crucible, before sliding the substrate into the main chamber. During this, the parameters required were inputted into the SQM-160 rate/thickness film deposition monitor (Inficon, Bad Ragaz, Switzerland). These included the thickness of the metal layer to be deposited, the density and the Z-Ratio of the metal to be deposited. The thickness was set to 10 kÅ (1000 nm), the density of Ti at 4.500 and the Z-Ratio of Ti at 0.628. Once the substrate was secured and the main chamber door locked, the electron beam was directed onto the Ti using the controller knobs. The power was slowly increased up to 100 mA before opening the shutter to allow for the Ti to evaporate onto the borosilicate substrate. The rate was monitored and was kept between 2 to 3 Å/s. The shutter automatically closed, and the electron beam turned off when the Ti layer reached 1000 nm. The substrate was then carefully removed from

the main chamber into the external chamber, which was then pressurized to room temperature before opening to collect the substrate.

The electrode deposition formed a layer of Ti across the whole surface of the borosilicate. Therefore, the next step involved removing the excess Ti to leave behind only the array design. This was carried out by dissolving the negative photoresist previously applied using TechniStrip NI555 at 80°C (MicroChemicals) until all the unwanted layer of Ti was removed. Dissolving the negative resist meant that the Ti layer that was deposited on top of it was also removed leaving behind just the Ti array design.

2.2.2.2.6 2nd Spin Coating

The next step was to prepare the surface for the deposition of the silicon dioxide (SiO_2) insulating layer. The photolithography process was similar to what was described in section *2.2.2.2.3*. However, this time the insulating design photomask was used instead and an AZ 1505 positive photoresist (MicroChemicals) was used. The settings for the spin coater (**Figure 2.5A**) were 2000 rpm for 30 seconds. Also, the substrate was developed in an AZ 351B Developer MIC (metal ion containing) (MicroChemicals) which was used in a 1:4 dilution (1 part developer and 4 parts DI water). The substrate was then washed as previously and taken for SiO_2 deposition.

2.2.2.2.7 Insulator Deposition

The SiO_2 was deposited using the same process as the Ti, however the density and Z-Ratio parameters were changed to 2.648 and 1.000 respectively. The thickness of SiO_2 was 500 nm. Following the deposition, the next step was to remove the SiO_2 from the electrodes and contact pads as those were the areas that needed to be exposed. In this case, the positive photoresist was removed using acetone which only left behind SiO_2 on the tracks connecting the electrodes to the contact pads.

2.2.2.2.8 Laser Lithography

After testing these custom MEAs it was found that the tracks were not always fully insulated, or the electrodes not exposed (**Figure 2.13**). These issues were resolved by using a DWL 66+ (Heidelberg Instruments Mikrotechnik, Heidelberg, Germany) (**Figure**

2.5D) laser lithography system. This machine is able to laser etch structures down to 300 nm and able to do direct photoresist patterning. Therefore, it meant that the step of aligning the film photomask and exposing with UV was no longer necessary. The array designs were adjusted in KLayout (Matthias Köfferlein, Germany) in order to be read by the laser writer software. The borosilicate substrate, that was previously spin coated with a layer of negative photoresist, was placed onto the stage and then the rest was done through the software package provided by Heidelberg Instruments. The write-head automatically aligned itself with the substrate before it began etching the array design onto the photoresist. Once this was done, the same steps previously described for the Ti deposition were carried out, however this time the Ti thickness was set to 150 nm. The insulating design was also laser etched instead of using a film photomask. This meant that the electrodes and contact pads were precisely cut out and therefore exposed following the deposition (100 nm) and removal of SiO_2 as described in section *2.2.2.2.7*.

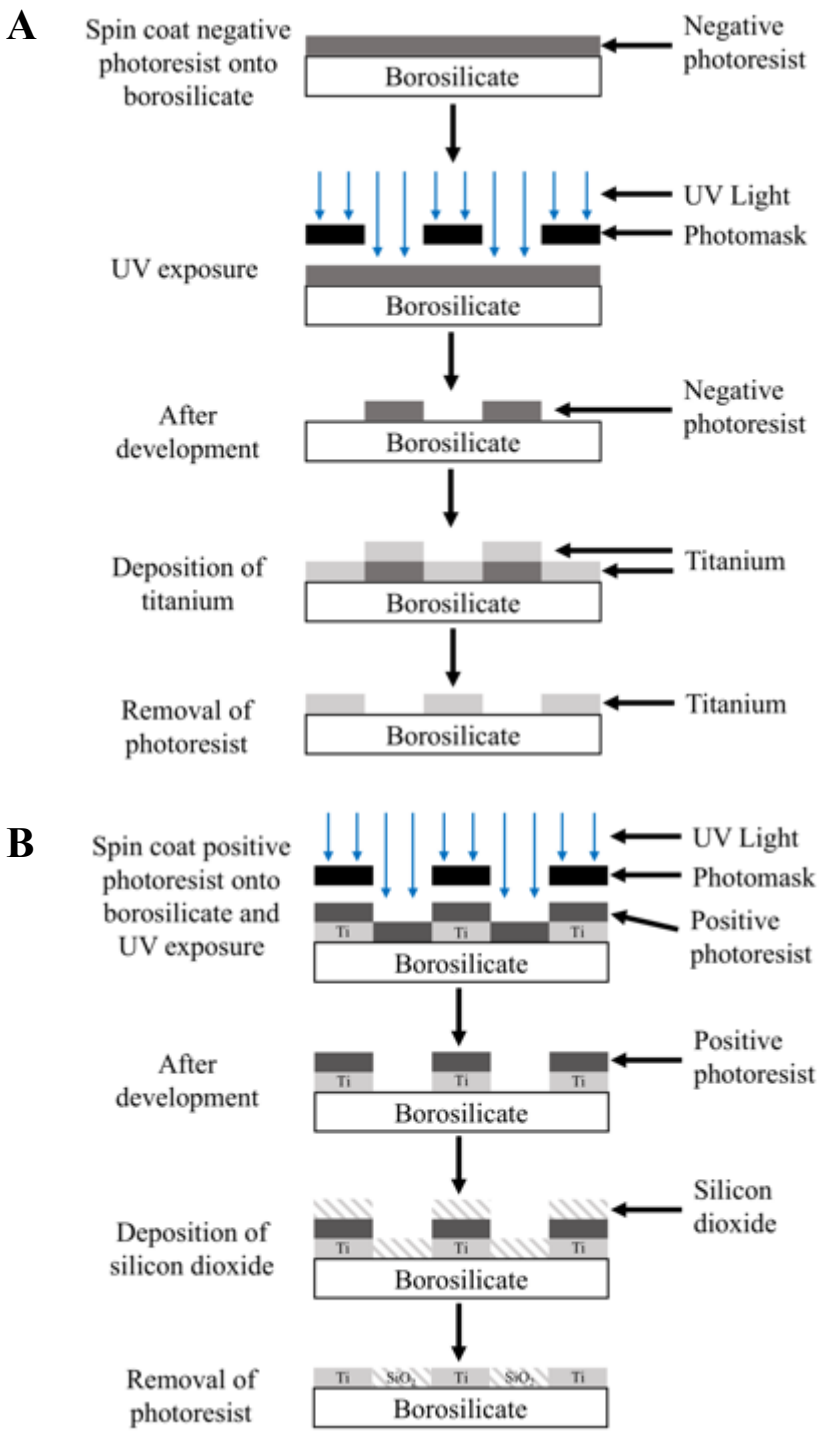

Figure 2.4: Step by step photolithography process for metal and insulator deposition. (A) A layer of negative photoresist was spin coated onto borosilicate. UV exposed negative photoresist became cross linked and the unexposed parts were dissolved with AZ 726 MIF developer. Titanium was then deposited over the whole surface of the borosilicate using physical vapour deposition. Finally, the negative photoresist was dissolved using TechniStrip NI555 which resulted in the removal of unwanted titanium, leaving behind titanium in the desired pattern. **(B)** The same steps were repeated for depositing the silicon dioxide (insulator) layer but instead a positive photoresist was used. UV exposed positive photoresist became degraded and was dissolved with AZ 351B MIC developer. Following the deposition of silicon dioxide, the positive photoresist was removed using acetone, to expose the titanium electrodes and contact pads and only insulate the tracks connecting the two.

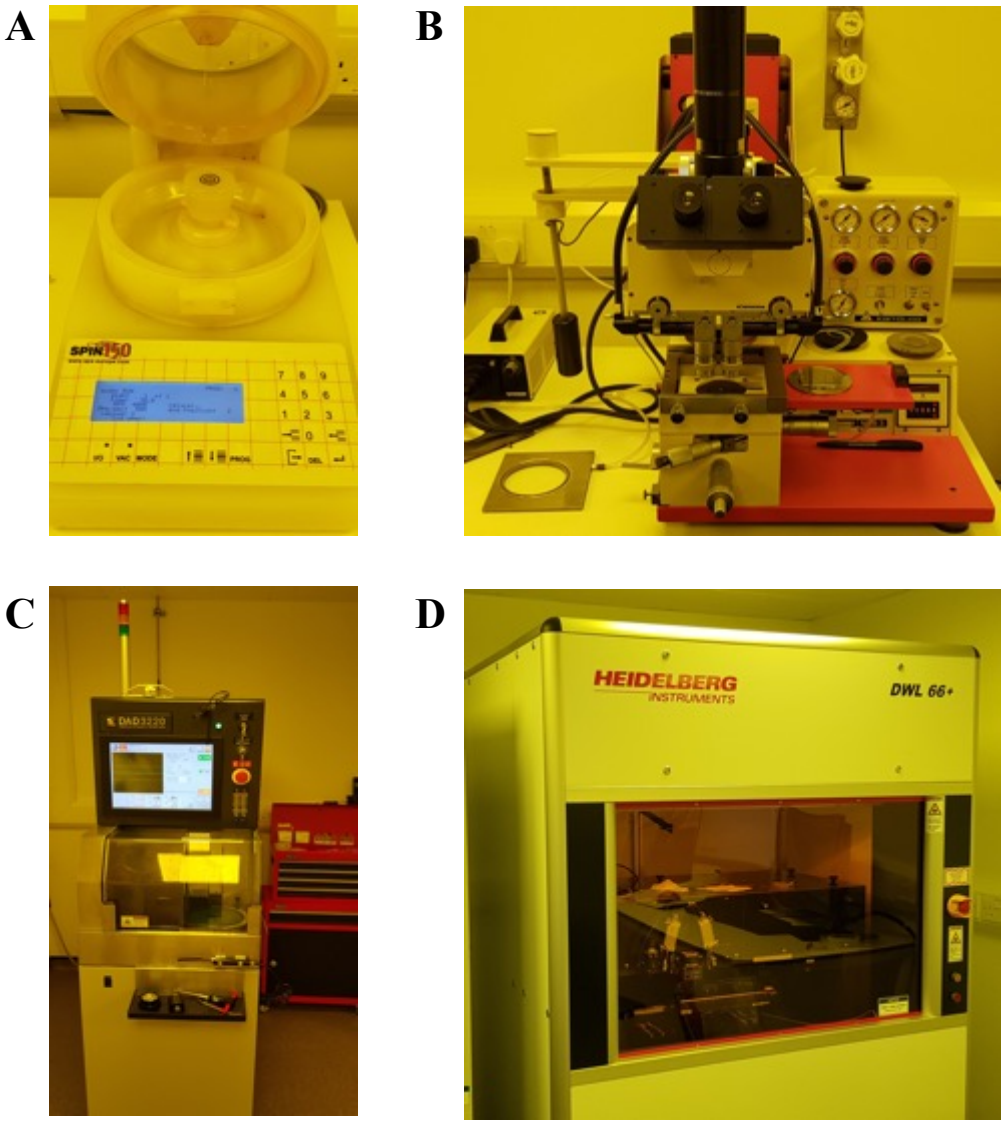

Figure 2.5: Equipment used for photolithography. (A) Spin coater for applying layer of either positive or negative photoresist onto borosilicate. **(B)** Photomask aligner for aligning film photomask over photoresist coated borosilicate and for UV exposure. **(C)** Dicing saw used for cutting borosilicate to measure 49 x 49 mm. **(D)** Laser lithography system for etching array design into photoresist without the requirement of a photomask.

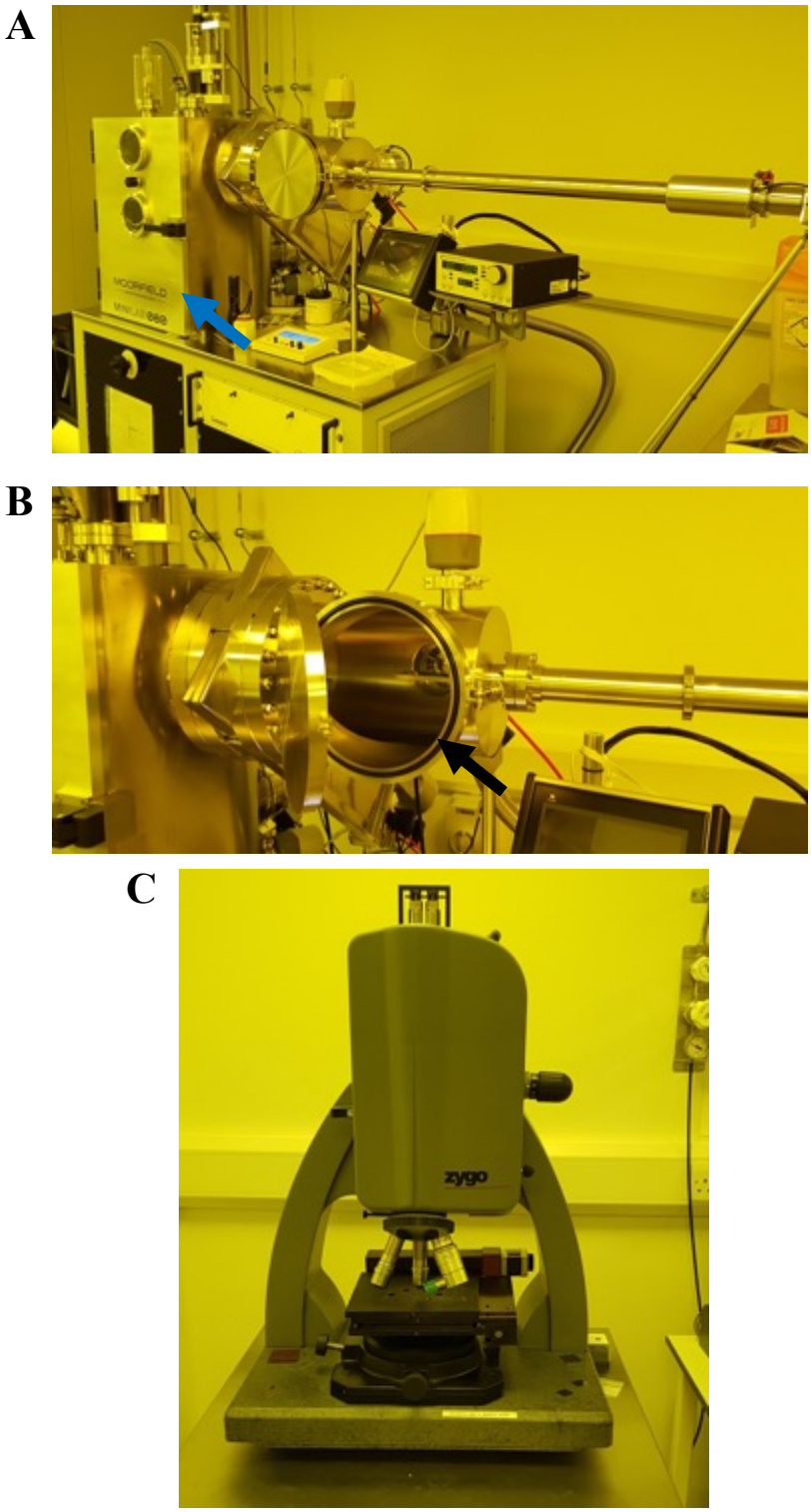

Figure 2.6: Equipment used for electrode deposition and evaluating custom MEAs. (A) Physical vapour deposition machine used for the layer deposition of titanium and silicon dioxide onto borosilicate. The vacuum sealed main chamber (blue arrow) was where the deposition occurs. **(B)** The borosilicate was initially placed in the external chamber (black arrow) before it was slid into the main chamber once a vacuum was reached in the external chamber. **(C)** Zygo 3D surface profiler used for evaluating quality of the metal and insulator deposition on the custom MEAs.

2.2.2.3 Evaluating Surface of Custom and Commercial MEAs

2.2.2.3.1 Imaging Surface Features

The integrity of the custom MEAs was investigated using a NewView 5000 3D surface profiler (Zygo Corporation, Pennsylvania, USA) (**Figure 2.6C**) and analysed using MetroPro software (Zygo Corporation, Pennsylvania, USA). This machine uses a technique called coherence scanning interferometry (CSI) to scan the surface using white light interferometry to measure and image the topography of a surface and can resolve sub-micron x-y features. A single light source is split into two by a beam splitter, the light waves travel in different directions before they merge, and the light is sent to the detector to produce interference.

The custom MEA was placed onto the stage and using the stage x-y control knob the features of the array were found using a 10x objective. Once the feature to be investigated was found, the focus Z control knob was adjusted upwards or downwards until bands of light and dark lines called fringes were formed. The fringes were adjusted, if necessary, using the stage tip and tilt knobs. The light intensity was adjusted and ranged between 70 – 75% in order to avoid saturation before the measure button was clicked to scan the surface and collect the data. This resulted in a false coloured image of the surface and a surface profile graph plot (**Figures 2.13 – 2.15**). This technique also allowed for evaluation of the thickness of each layer on the substrate. In order to do this, a virtual line was drawn along two different features. Then through the "surface profile menu" of the software, selected "show controller" followed by the "inspect" button twice to bring two virtual lines onto the graph (arrowhead) (**Figure 2.13C**). The two virtual lines were first placed along a horizontal section of the graph before pressing the "level" button. Then one of the lines was moved to a lower or higher section of the graph in order to obtain a measurement. The software used for this analysis was MetroPro (Zygo Corporation).

2.2.2.3.2 Electrical Integrity of Electrodes

To measure the level of insulation and electrical integrity of electrodes, I measured the impedance (Z) of each electrode. This was carried out using an Omega-Tip-Z (World Precision Instruments, Florida, USA) electrometer. A polydimethylsiloxane (PDMS) module was placed on top of the electrodes to form a well in which sodium chloride (150

mM) was added as a conducting liquid. Each electrodes impedance, in Ohms, was measured individually by placing the probe on each electrode contact pad. The electrodes impedance was regularly checked after use in culture to check the integrity of the individual electrodes.

2.2.3 Design and Fabrication of Microfluidic Microchannels

2.2.3.1 3D Printed Module

Initially a 3D printed module was made that would separate cells into two different compartments with a barrier in between. The module was designed in AutoCAD before it was converted into an .stl file that could be read by a 3D printer. The 3D printer used was the Ember by Autodesk (California, USA) (Dr. Ferry Melchels Lab) which is a stereolithography (SLA) type printer. This type of 3D printer was chosen as the features necessary for the channels were in the micron scale which a fused deposition modelling (FDM) printer cannot achieve. The X and Y - axes resolution of the Ember was 50 μm and had a 10 to 100 μm Z – axis resolution. The module measured 1 x 1 cm and was comprised of two compartments separated by a 1 mm barrier. The bottom of the barrier that would be in contact with the custom MEA had a series of microchannels measuring 100 μm in width and 100 μm in depth. The channels were separated by 200 μm from each other. The resin used for 3D printing the module was the standard PR48 Autodesk resin.

2.2.3.2 Microchannel Fabrication using Soft Lithography

An alternative method was to add microfluidic channels on top of the custom MEA to restrict the neuronal cell bodies in the stimulating area and guide the axons to the recording electrodes. Therefore, this was taken into account when designing the microchannels as they had to align with the electrode configurations of the custom MEAs. The microchannels were designed using Adobe Illustrator (Autodesk) and were then sent to Micro Lithography Services to be produced into a film photomask. The features of the design included two separate compartments 100 μm apart connected by a microchannel measuring 10 μm wide. The compartment where the cell bodies would be restricted in measured 100 μm wide and the second compartment where the axons would grow into measured 300 μm wide. The second compartment also had pillars embedded in it, and that was added in order to avoid it from collapsing and breaking.

The soft lithography protocol (MicroChem, 2015) to prepare PDMS devices was similar to the photolithography protocol used when fabricating custom MEAs, however, had different parameters (**Figure 2.7**). A test grade silicon wafer (SILI-0005, PI-KEM Limited) with a diameter of 7.62 cm and thickness 380 μm (± 50 μm) was used instead of a borosilicate substrate.

2.2.3.2.1 Spin Coating and UV Exposure

The wafer was placed onto the spin coater (WS-650MZ-32NPP, Laurell Technologies Corporation) and held in place by a vacuum (**Figure 2.8A**). The negative photoresist SU-8 2025 (Microchem) was spun onto the wafer in two stages. First stage at 500 rpm for 10 seconds with an acceleration of 100 rpm/s and the second stage at 3000 rpm for 39 seconds with an acceleration of 300 rpm/s. These settings gave a film thickness of 25 μm. The wafer was soft baked at 65°C for a 1 minute, then at 95°C for 5 minutes and back down to 65°C for another minute. Film photomasks with the designs were then carefully placed on top of the wafer making sure to not move them once in contact with it. The wafer was then exposed to UV for 41 seconds (**Figure 2.7B**) before carrying out the post exposure bake at the same temperatures and times as the soft bake. The clear parts of the photomask (the two compartments and microchannels) became cross-linked and the dark parts of the photomask did not. This meant that the uncross-linked areas were removed by the developer leaving behind the design features.

2.2.3.2.2 Development

The wafer was submerged in SU-8 developer and sonicated for 60 seconds. It was then washed with isopropanol and blow dried with an air gun. The wafer was placed back into the developer for a further 60 seconds but not sonicated. The same washing steps were done until the wafer was shiny clean. If any streaks were still visible, the wafer was placed back into the developer for a further 60 seconds and repeated the process until they were no longer present.

Finally, the wafer can be used as a mould to produce the microchannels for as long as it can be kept intact. The surface of the wafer is hydrophilic which meant that it would be difficult to peel off the PDMS from it without leaving any residues or breaking the wafer. A drop of trichloro (1H,1H,2H,2H-perfluorooctyl) silane (448931, Sigma-Aldrich,

Missouri, USA) was added onto the wafer and left to evaporate at room temperature in a fume hood, making sure to close the top of the petri dish. The purpose of this was to make the surface hydrophobic and therefore avoid the issues mentioned earlier. The wafer was kept in a petri dish (**Figure 2.9B**).

2.2.3.2.3 PDMS Preparation

Once this was completed, PDMS was prepared by mixing Sylgard 184 silicone elastomer base with the curing agent at a 10:1 ratio. PDMS was then poured over the wafer and before curing, air bubbles were removed using a vacuum chamber. The PDMS cured in an hour at 60°C. Once cured, PDMS modules (microchannels) were carefully cut out using a scalpel trying to avoid damaging any of the features on the wafer. Holes were then cut out using a 6 mm biopsy punch on either side to form wells (**Figure 2.9B**). This was also carefully done in order to avoid damaging the microchannels.

When replacing the film photomask with a quartz photomask, the same protocol for soft lithography was followed when producing the wafer. The only difference was instead of placing the film photomask on top of the wafer prior to UV exposure a quartz photomask was used instead.

2.2.3.2.4 PDMS Device Bonding

The PDMS modules fabricated were then bonded onto custom MEAs, polystyrene wells of tissue culture plates and borosilicate coverslips before culturing cells in them (discussed in detail in Chapters 3 and 4). Before bonding was carried out the surfaces had to be made hydrophilic. This was achieved by placing the PDMS modules and the surfaces they would bond onto into a Zepto plasma system (Diener Electronic, Ebhausen, Germany) (**Figure 2.8C**). Finally, the PDMS microchannels had to be carefully aligned with the stimulating, ground and recording electrodes before bonding onto the MEAs. This was done by hand with the aid of an inverted microscope.

2.2.3.3 Microchannel Flow Modeling Simulations

To better predict the behaviour of fluids and cells in the microfluidic module and refine the design of channels, flow modeling simulations were carried out. The microchannel

designs made in AutoCAD were imported into ANSYS Discovery SpaceClaim (Ansys Inc, Pennsylvania, USA) software where they were converted into an .sab geometry file. The file was then imported in ANSYS Workbench (Ansys Inc, Pennsylvania, USA) where a mesh was created on the surfaces labelled inlet, outlet and walls. The layer heights of the designs were set to 25 μm. The programme then generated the mesh from all the input data. The mesh was then transferred into ANSYS Fluent where the simulations were carried out. The input pressure was set to 67.7 Pa and 22.6 Pa at the outlet. Operating pressure was set to 45.1 Pa. The input and output pressures were calculated from the height of fluid in the input and output end wells. The height in the input end was 6.9 mm and 2.3 mm in the output end. The simulations were done over a period of 60 seconds. Once the simulations were complete, the data was exported and later analysed using Microsoft Excel. The flow simulations were carried out by Janez Javornik (Erasmus Plus Student, Dr. Euan Brown's Lab).

The volume transferred from the input well and into the output well through the microchannels per 24 hours was calculated as follows. The flow rate (Q) for each microchannel was calculated by multiplying the area (A) and the average velocity (v) ($Q = A \times v$). The time (T) it takes to fill in the microchannel of known volume was calculated by dividing the volume (V) by the flow rate ($T = V / Q$). The volume transferred per second was calculated by dividing the V by T. This value was multiplied by 86,400 (number of seconds in 24 hours) to obtain the final value, volume transferred in μl / 24 hours.

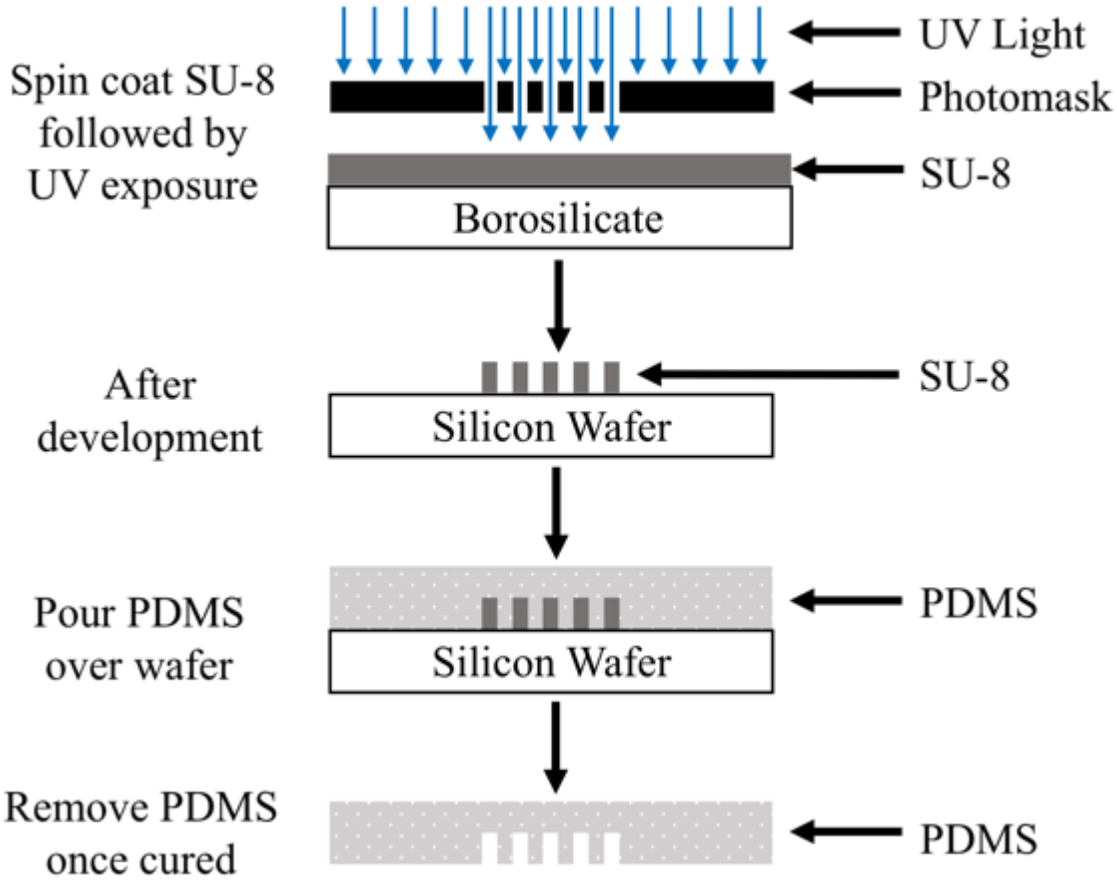

Figure 2.7: Soft lithography process to produce microchannels. (A) A layer of SU-8 (negative photoresist) was spin coated onto a silicon wafer. A photomask was placed over the SU-8 layered silicon wafer after a soft bake step. Following UV exposure, the exposed regions became cross linked and the unexposed parts were dissolved with developer. Polydimethylsiloxane (PDMS) was prepared and poured over the wafer mold created. The PDMS with embedded microchannels was then carefully removed once it had cured (60°C for 1 hour). The wafer mold could be then used to produce more PDMS modules with microchannels.

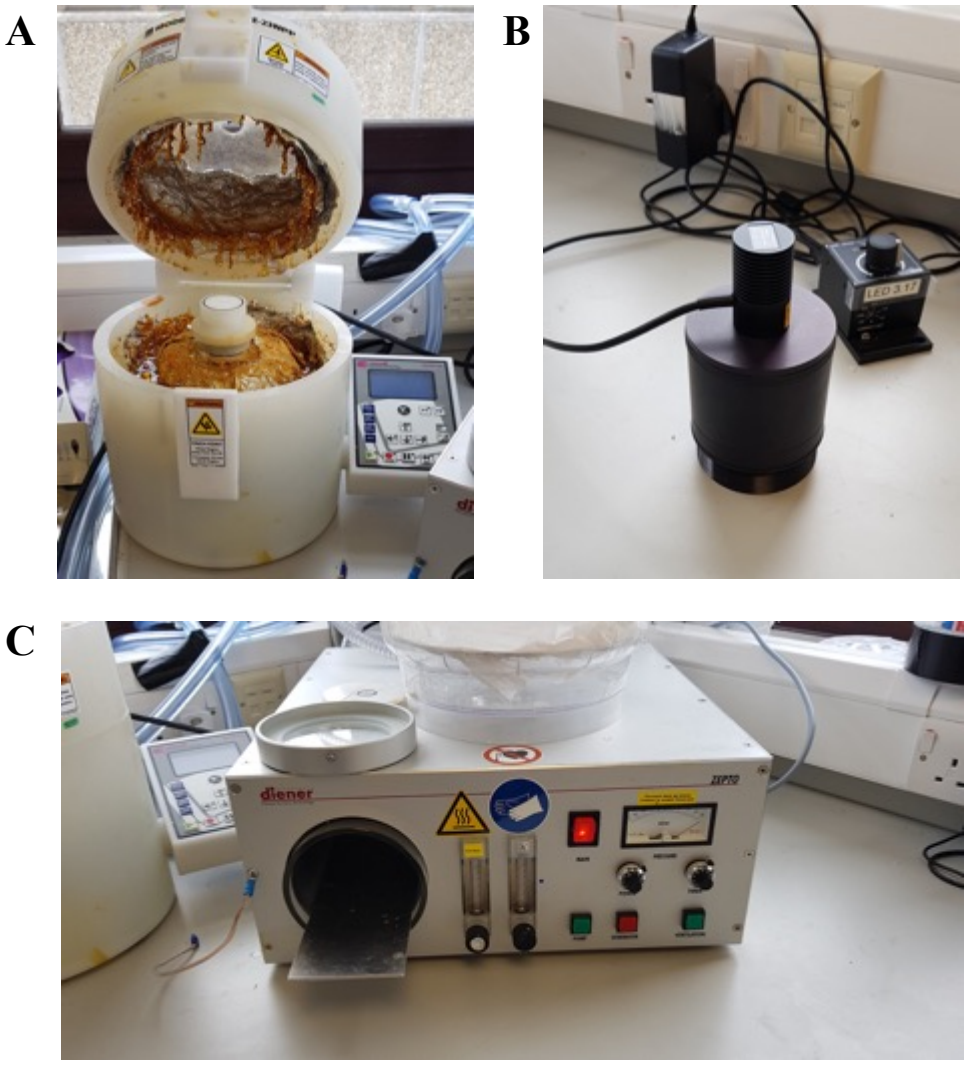

Figure 2.8: Equipment used in soft lithography process for making microchannels. (A) Spin coater for applying layer of SU-8 onto silicon wafer. **(B)** UV lamp for exposure step. **(C)** Plasma coater for making surface of PDMS and MEAs hydrophilic.

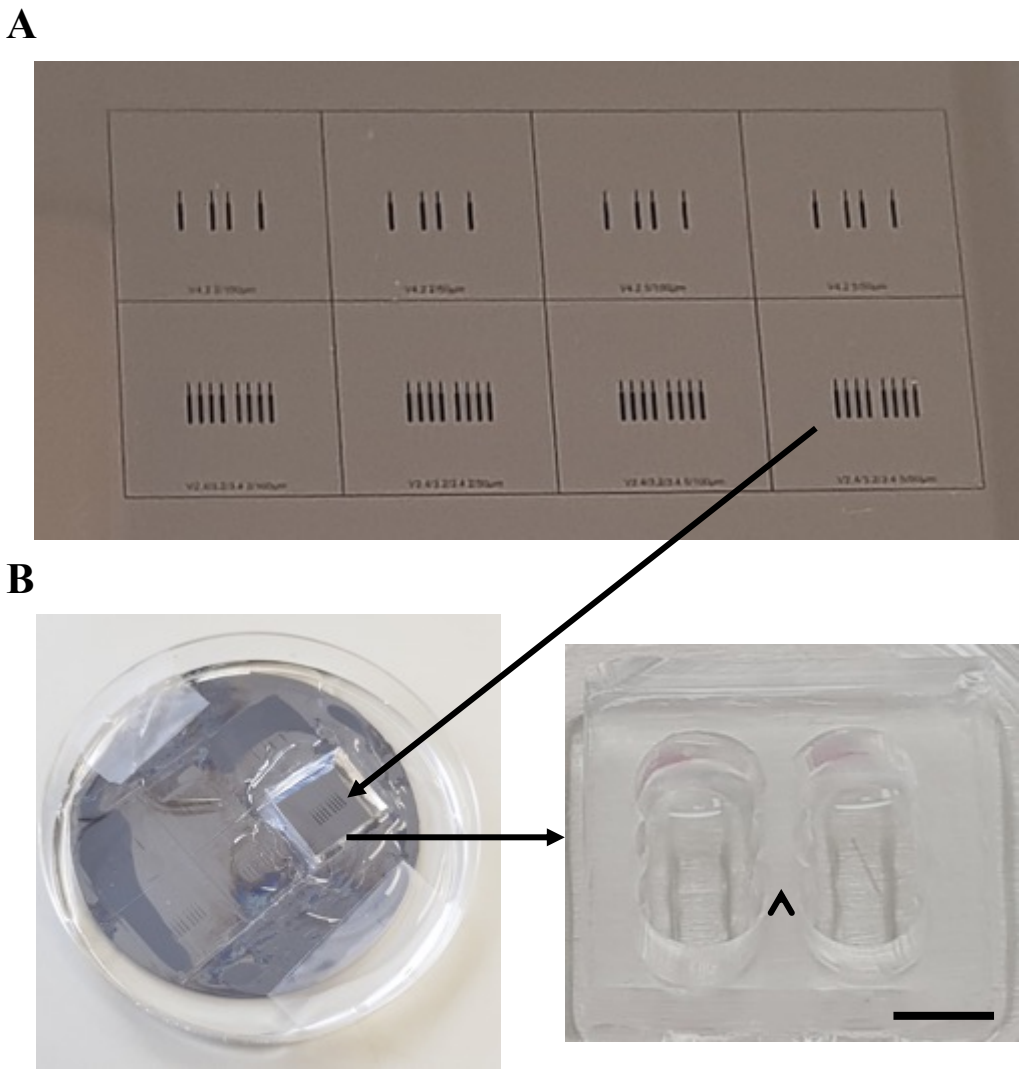

Figure 2.9: Example of PDMS module with microchannels. (A) Quartz photomask with different microchannel designs. The desired pattern was clear to allow UV light to pass through and form that pattern onto the SU-8**. (B)** PDMS covered silicon wafer (silver disc at bottom of petri dish) shown on the left. The microchannel design produced (arrow from quartz photomask) can be seen. The PDMS cut out is shown on the right. PDMS module comprised of two well compartments with the microchannels in between them (arrowhead). Cells were cultured in the left compartment and media alone was added in the right compartment. The volume in the left compartment was greater than that in the right compartment in order to allow media to flow from one compartment to the other. Scale bar = 5 mm.

2.3 Results

2.3.1 Development of System to Record from MEAs

The recording devices, RD1 and RD2, (**Figure 2.10A** and **2.10B)** both have the same arrangement of spring pins, forming a square with a total of 60 pins (16 on each side). As the amplifier is only capable of recording from 16 different electrodes it was necessary to be able to swap from one side to another easily in order to record from the whole commercial MEAs when necessary. As can be seen, the tops of these devices were different, and this is because RD2 (**Figure 2.10B)** is the new and improved version of RD1 (**Figure 2.10A)**. When recording from a different side, the ground cables had to also be moved and this regular change put a strain on the cables which in turn kept breaking off and needing to be re-soldered. Also, the other 16 cables were loosely soldered on top of the device and the same issue arose as they kept breaking off. Temporary fixes were done; however, it was important that these issues were addressed in the new device.

RD2 (**Figure 2.10B**) had no cables exposed and the ground cables were soldered onto one single ground point. Also, the cables interfaced the pins using a more robust connector that meant the regular changing of the recording side did not cause any issues with the cables breaking off and having to worry if any inactivity or activity recorded was due the connectivity of the cables to the pins. Finally, the recording device RD3 (**Figure 2.10C)** was the one produced to hold custom MEAs. It has a total of nineteen pins, sixteen for recording, two for stimulating and one ground.

2.3.1.1 Evaluating Recording Devices

After initial tests of RD1, it was found that the stage of the microscope (Brunel Microscopes Ltd, Chippenham, UK) was too thick to allow a clear focus on the cells with the objectives supplied with the microscope (**Figure 2.11A**). Therefore, the original stage was replaced with a 2 millimetre (mm) thick aluminium sheet with a cut-out that would allow the objectives to move through it freely. An additional sheet of aluminium with a circular cut-out (30 mm diameter) was then placed on top as a surface for the Peltier device (**Figure 2.11B**). Thermal paste was applied on both the aluminium sheet and the bottom of the recording device before aligning the circular Peltier device onto them. It

was important to keep our cultures in the MEAs at 37°C and using a Peltier was a simple, cheap but reliable way of doing so.

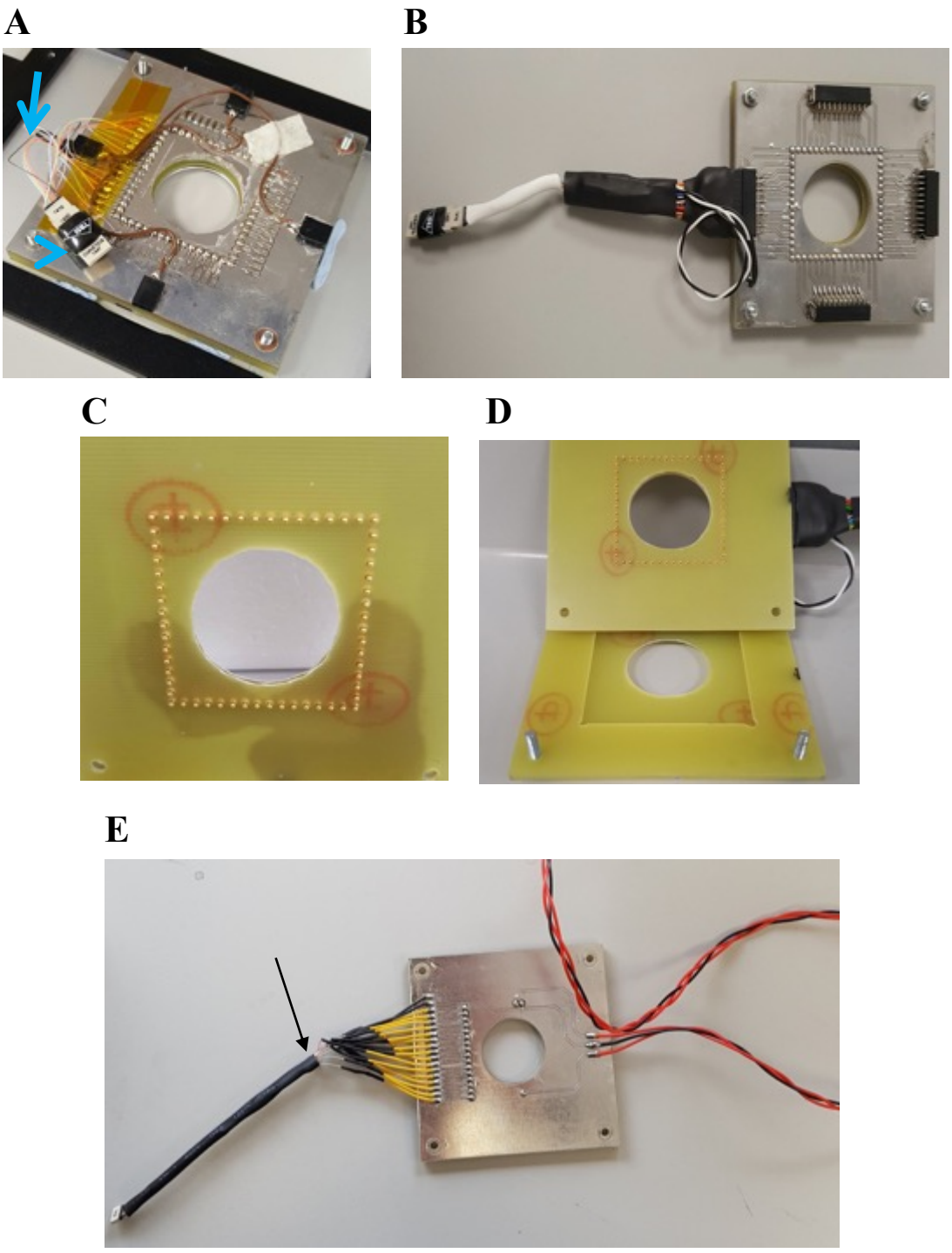

Figure 2.10: Evolution of the custom recording device. (A) First (RD1) and **(B)** upgraded (RD2) recording devices fabricated for holding and recording from commercial MEAs. Preamplifier headstage (blue arrowhead) connected to the pins through the nano strip connecting cables (blue arrow). **(C)** Close up view of pin configuration (total of 60 pins) and **(D)** base of device where the MEA is placed. **(E)** Recording device (RD3) for custom MEAs featuring 16 recording pins (arrow for 16 cable connections), 2 stimulating pins (red cable) and 1 ground pin (black cable in between the two red cable connection).

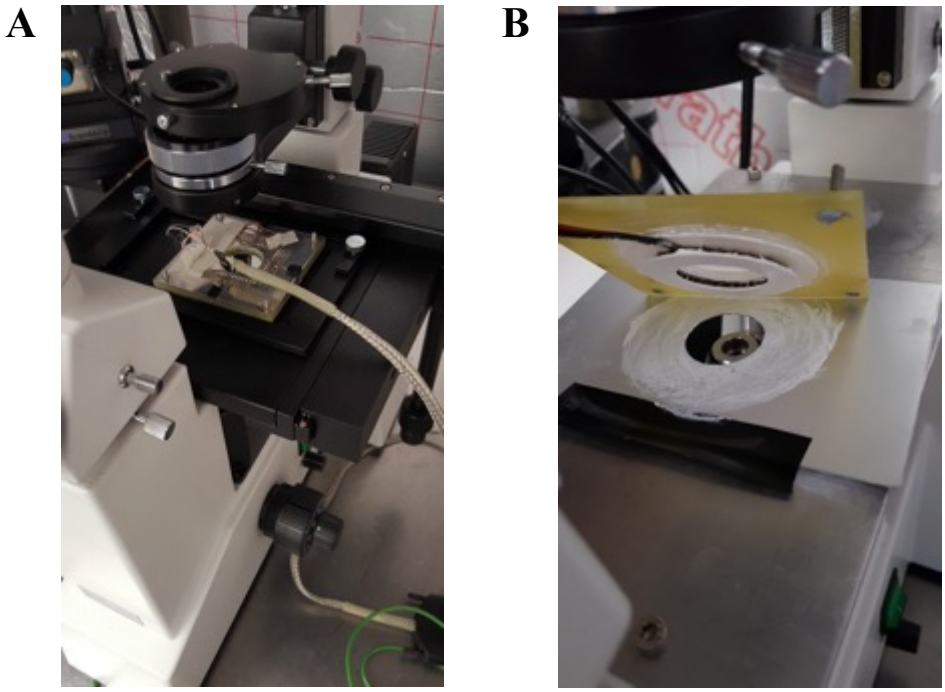

Figure 2.11: Microscope set up alterations for MEA recordings. (A) Original microscope stage that did not allow for imaging whilst recording from MEAs. **(B)** Current microscope stage where original stage was replaced with a thin aluminium sheet. Circular Peltier device (arrow) attached to the bottom holder of the recording device with thermal paste for temperature control.

2.3.2 Evaluating the Surface Properties of Custom and Commercial MEAs

Several different iterations of custom MEAs were fabricated. One of these can be seen in **Figure 2.12A** with a PDMS two-well module bonded on top of it.

2.3.2.1 Imaging Surface Features

The electrodes of V2.0 MEAs fabricated using a film photomask were found to not be exposed as the 3D imaging indicated no differences in thickness when compared to the insulated tracks (**Figure 2.13A**). The height of the track (Ti and SiO_2) compared to the surface plane (SiO2 layer) was approximately 900 nm. This was expected as for the V2.0 MEAs, the layer thickness was set to 1000 nm and 500 nm for Ti and SiO_2 respectively (**Figure 2.13C**).

The electrodes of V3.0 MEAs were exposed as the 3D image showed that the thickness of tracks was greater than that of the electrodes which meant that they were not insulated (**Figure 2.14A**). Relative to the electrode (Ti layer), the track (Ti and SiO_2) was 95 nm above it. In turn, the electrode was raised by 73 nm from the surface plane (SiO_2 layer) (**Figure 2.14C**). Therefore, the total thickness of the layers was 263 nm as the Ti layer was 168 nm and the insulating SiO_2 layer was 95 nm in depth.

The surface of a commercial MEA (60MEA200/30iR-Ti) was also analysed. It was found that the electrodes of the commercial MEAs were raised above the surface plane by about 300 nm (**Figure 2.15**).

2.3.2.2 Electrical Integrity of Electrodes

When evaluating electrode quality by measuring the impedance, if the impedance measured was zero it meant that the array was not properly insulated. On the other hand, if the resistance was infinite it meant that the electrodes were not exposed at all, were broken or were completely covered with SiO_2. Initially, it was found that not all electrodes were properly exposed as no resistance was measured from them. This was the case for the first custom MEAs that were fabricated using film photomasks, whereas the upgraded laser etched custom MEAs did not have this issue. The mean impedance calculated from

5 custom MEAs (80 electrodes in total) was 56.7 kΩ. The impedance of the commercial standard 60MEAs used was < 100 kΩ (Multichannel Systems technical specifications).

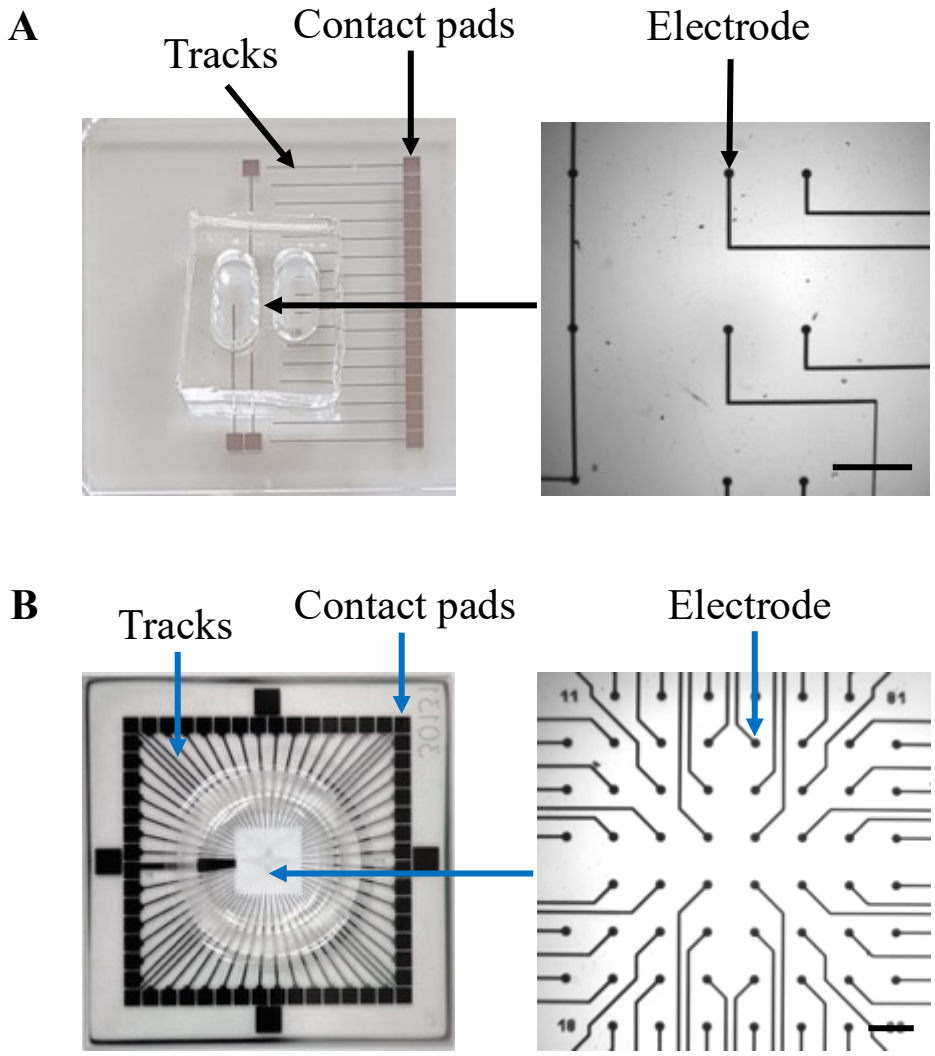

Figure 2.12: Features of custom and commercial MEAs. (A) On the left, one of the final versions of custom MEA fabricated at the Heriot Watt Nanofabrication facility. A series of 16 contact pads can be seen along the right side of the MEA which connect to the recording electrodes through the visible tracks. The other 3 contact pads visible are connected to the stimulating and ground electrodes. The electrodes are concentrated in one area near the centre of the MEA and the image on the right shows a few of these electrodes. More details on the module with two wells over the MEA will be explained in Section 2.4.3. Scale bar = 500 µm. **(B)** A commercial MEA (60MEA200/30iR-Ti) comprised of 60 contact pads and tracks connecting to 59 recording electrodes and 1 reference ground electrode. The electrodes are concentrated in the centre of the MEA and are laid out as seen in the image on the right. Scale bar = 200 µm.

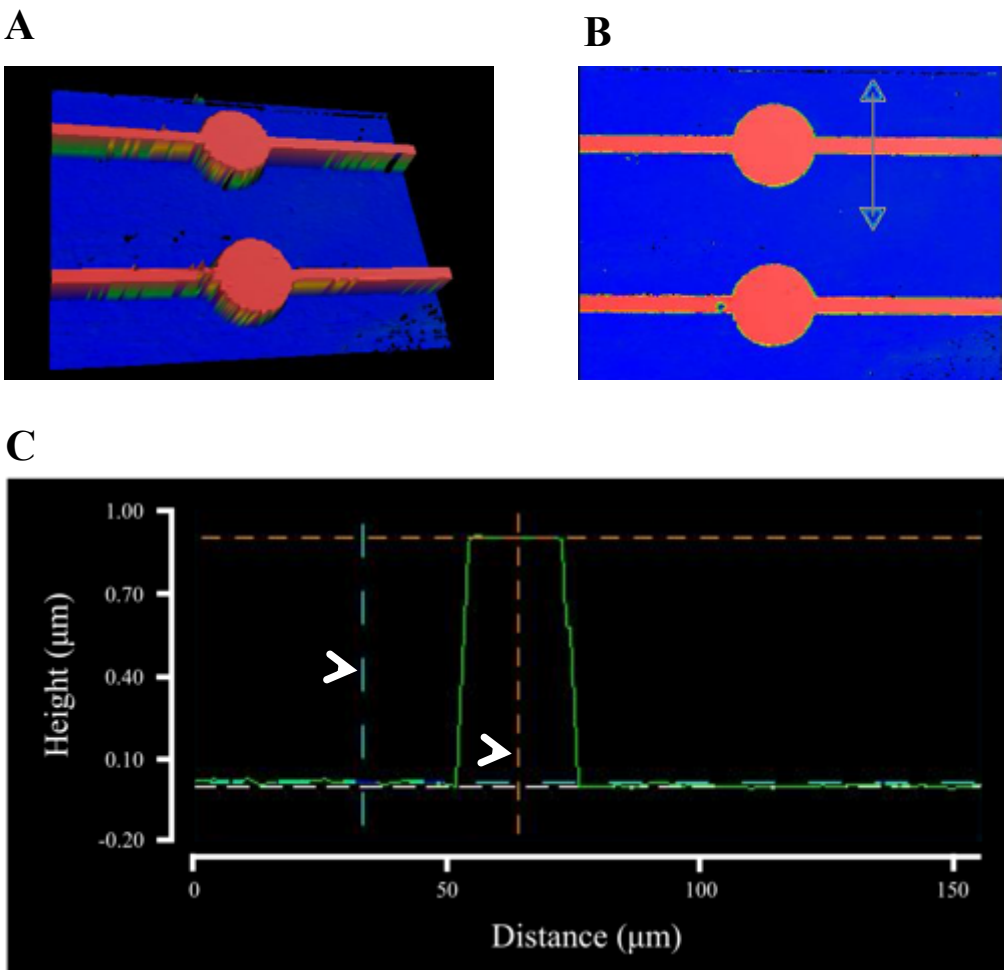

Figure 2.13: 3D profile of electrodes and tracks of first custom MEA fabricated using a film photomask. (A) 3D image of two electrodes – stimulating and ground in parallel, with the tracks on either side. In this MEA the electrodes were not exposed as no changes in height between the tracks and the electrodes were observed. **(B)** Scan showing cross-section line over electrode track. **(C)** Profile plot that shows the differences in height along the cross-section line. Virtual dashed lines used for calculating differences in height of features indicated by white arrowheads. In this case the track was about 900 nm above the surface.

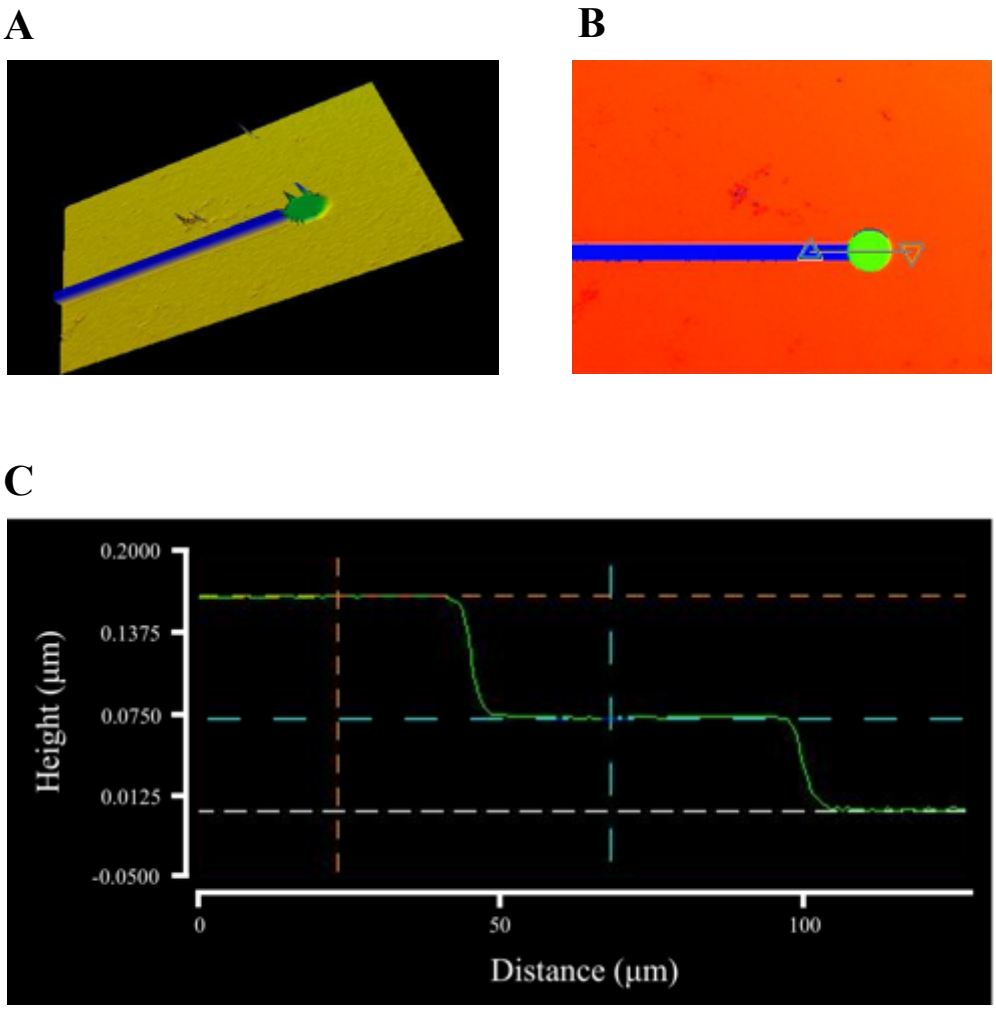

Figure 2.14: 3D surface profile of electrode and track of upgraded custom MEA (V3.2) fabricated using laser lithography instead of a film photomask. (A) 3D image of electrode (green) and track (blue). **(B)** Scan showing cross-section line across part of the insulated track, the exposed electrode and insulated surface of the MEA. **(C)** Profile plot showing the differences in height along the cross-section line. The insulated track is 95 nm above the exposed electrode which in turn is 73 nm above the surface of the MEA.

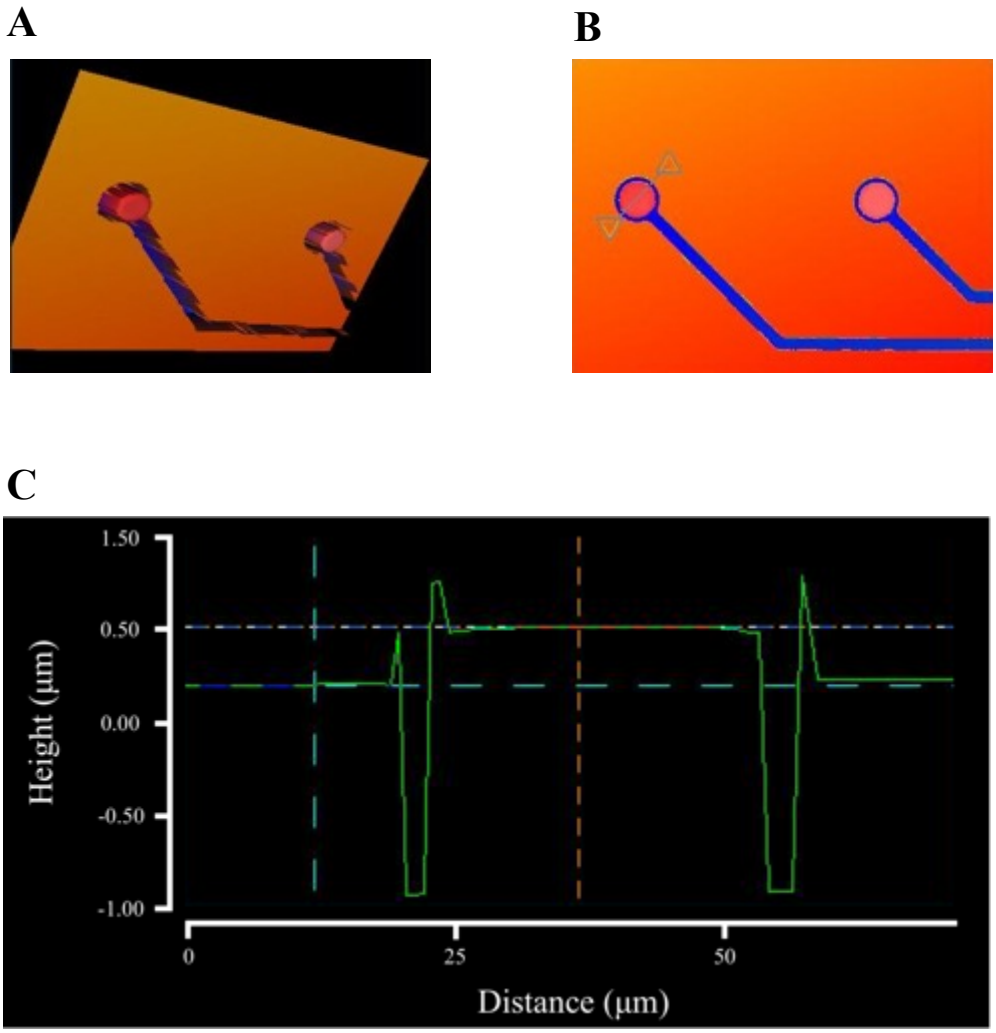

Figure 2.15: 3D surface profile of commercial MEA electrodes. (A) 3D image of the electrodes that are raised above the surface of the commercial MEA. **(B)** Scan showing cross-section line across one electrode. **(C)** Profile plot that shows the differences in height along the cross-section line. This shows that the electrodes of the commercial MEA are about 300 nm above the surface.

2.3.3 Fabricated Microfluidic Microchannels

2.3.3.1 3D Printing and Cell Survival

The 3D printed module comprised of two compartments separated by microchannels (**Figure 2.16)**. Following initial tests with culturing neuronal cells in the presence of the 3D printed module it was concluded that it would be of no use, as cell death was observed after a few days in culture. It was also noted that the minimum channel width of 100 µm was far too large to prevent cells from entering the second well from the first. This was not the case for the fabricated PDMS modules with embedded microchannels as PDMS is biocompatible and the channel width achieved using photolithography was 5 µm.

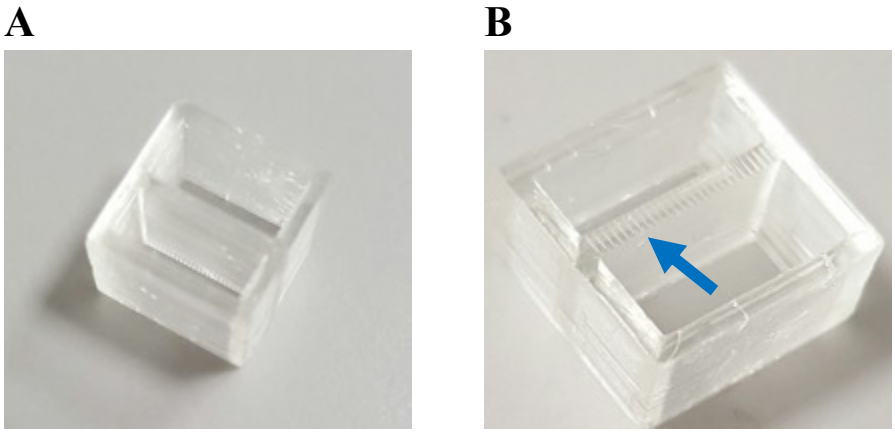

Figure 2.16: 3D printed compartments with microchannels. (A) Top view and **(B)** bottom view of 3D printed module with embedded microchannels (arrow).

2.3.3.2 Microchannel Flow Modelling

The flow simulations showed that laminar flow could be achieved in the microchannels measuring 5 and 10 µm in width (**Figure 2.17**) with the pressure used in the input well. Laminar flow occurs when fluid flows in parallel layers with no disruption. This was observed in the flow simulations as inside the microchannels there was a red 'fast' flow band. The peak velocities varied between the three designs as expected. The peak velocity for the microchannels measuring 10 µm wide by 100 µm in length was 48.4 µm/s with the average velocity along the microchannels being 13.8 µm/s (**Figure 2.17A**). The microchannels measuring 5 µm wide by 100 µm long had a peak flow velocity of 13.0

μm/s and an average velocity of 6.89 μm/s (**Figure 2.17B**). Finally, the peak flow velocity of the microchannels measuring 5 μm by 50 μm was 24.4 μm/s with the average velocity being 10.1 μm/s (**Figure 2.17C**). The flow velocity measured in the wells on either side of the microchannels was very low (around 1 μm/s) and was not laminar.

To estimate the exchange rate of solution between the two sides through the microchannels I calculated the volume transferred per 24 hours. The volume transferred was calculated to be 2.4 μl / 24 hours for the microchannels measuring 10 μm wide by 100 μm in length, 0.6 μl / 24 hours for the microchannels measuring 5 μm wide by 100 μm in length and 0.9 μl / 24 hours for the microchannels measuring 5 μm wide by 50 μm in length.

2.3.3.3 PDMS Microchannels

The first PDMS devices fabricated did not have smooth features and the microchannels were not consistently 10 μm wide (**Figure 2.18**). This was due to the film photomask used and therefore, the final devices were fabricated using a chrome coated quartz photomask (**Figure 2.9A**). Unlike with a film photomask, using a quartz photomask allows for fabricating devices with sub-micron features. Therefore, the designs sent to Micro Lithography Services had altered microchannel widths measuring 5 μm instead of 10 μm.

The PDMS devices fabricated using a quartz photomask had perfectly smooth features and the feature dimensions came out as expected. The microchannels were 5 μm in width and either 50 μm or 100 μm in length (**Figure 2.19**).

2.3.3.4 Microchannel Alignment

PDMS microchannels had to be aligned with the electrodes of the custom MEAs and the wells on either side had to be sealed to prevent media loss over the culture period. Plasma treating the PDMS surface and the surface of the custom MEA resulted in a strong bond between the two. The channels were aligned following the plasma treatment in order to establish a proper seal. PDMS microchannels were also bonded onto borosilicate coverslips and tissue culture treated wells. The seal formed on borosilicate coverslips and

custom MEAs lasted up to 6 weeks without leakage of media whereas on the tissue culture treated wells seals were maintained for only up to 2 weeks.

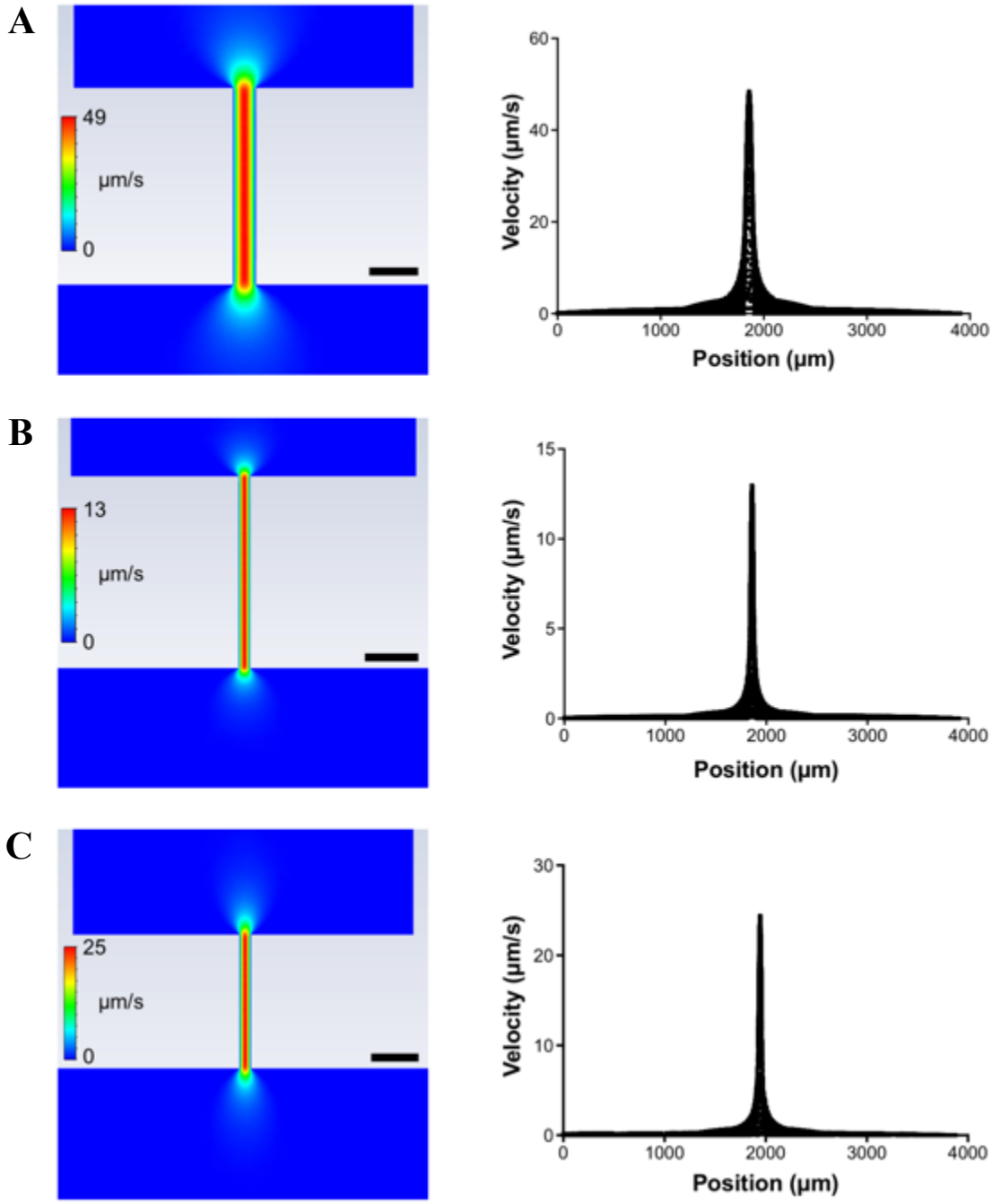

Figure 2.17: Flow modeling of microfluidic microchannels. The images on the left show the flow velocity along 3 different microchannel dimensions. Laminar flow was seen to occur in all the designs. The graphs on the right side, show the varying velocities that occur within the microchannels. The peak flow velocity for the **(A)** microchannels measuring 10 μm by 100 μm was 48.4 μm/s, **(B)** 13.0 μm/s for the microchannels measuring 5 μm by 100 μm and **(C)** 24.4 μm/s for the microchannels measuring 5 μm by 50 μm. All microchannels had a height set to 25 μm. Scale bar = 20 μm.

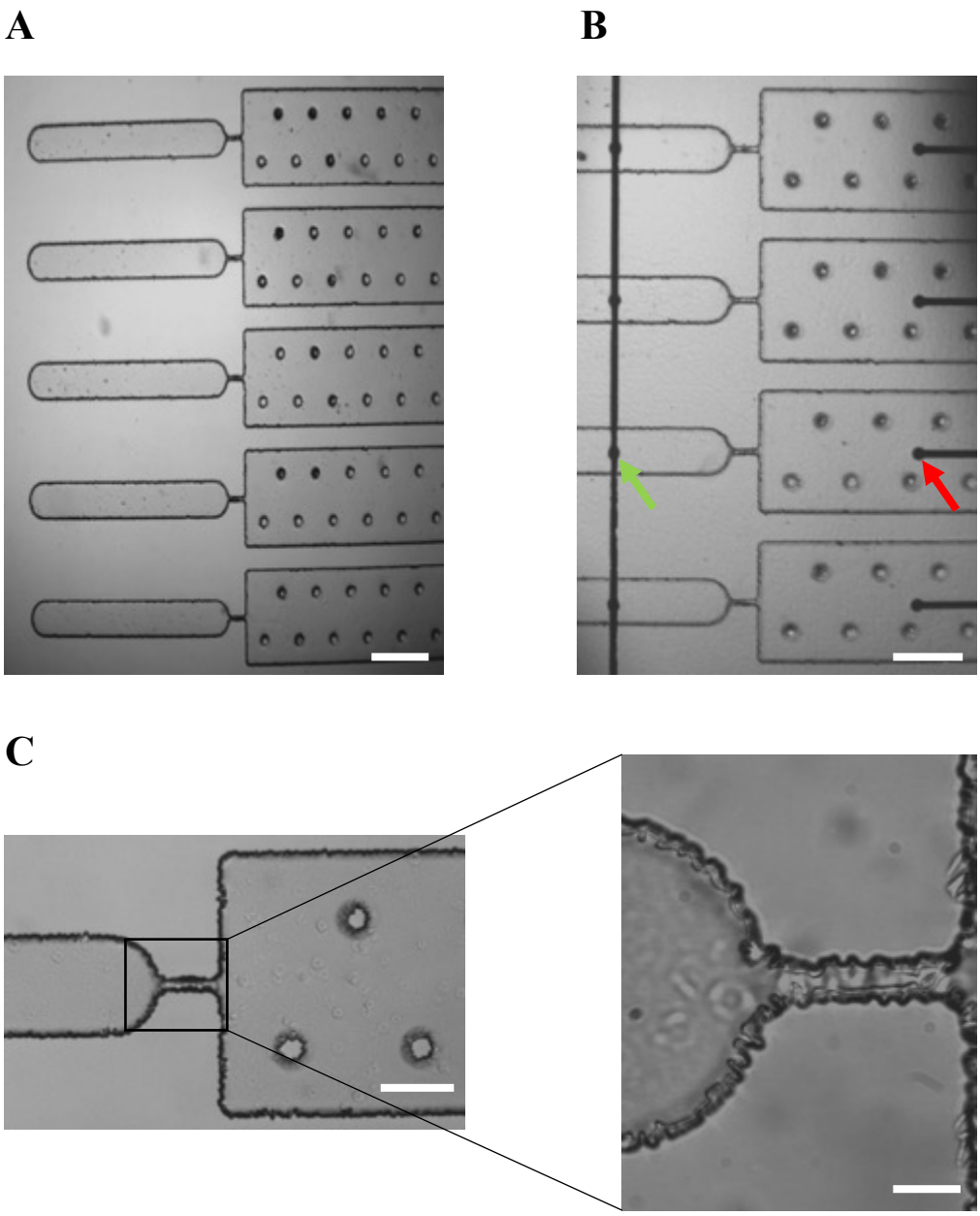

Figure 2.18: Fabricated microchannels in PDMS using film photomask. (A) Magnified view (4x) showing the full design of the PDMS device. The circular features seen are pillars to prevent that compartment from collapsing and breaking. Scale bar = 200 µm. **(B)** PDMS design aligned over stimulating (green arrow) and recording (red arrow) electrodes of one of the earlier custom MEA versions (V2.0). Scale bar = 200 µm. **(C)** Magnified view of a single microchannel on the left (scale bar = 100 µm). A closer look at the approximately 10 µm in width microchannel in between the two compartments. Scale bar = 20 µm.

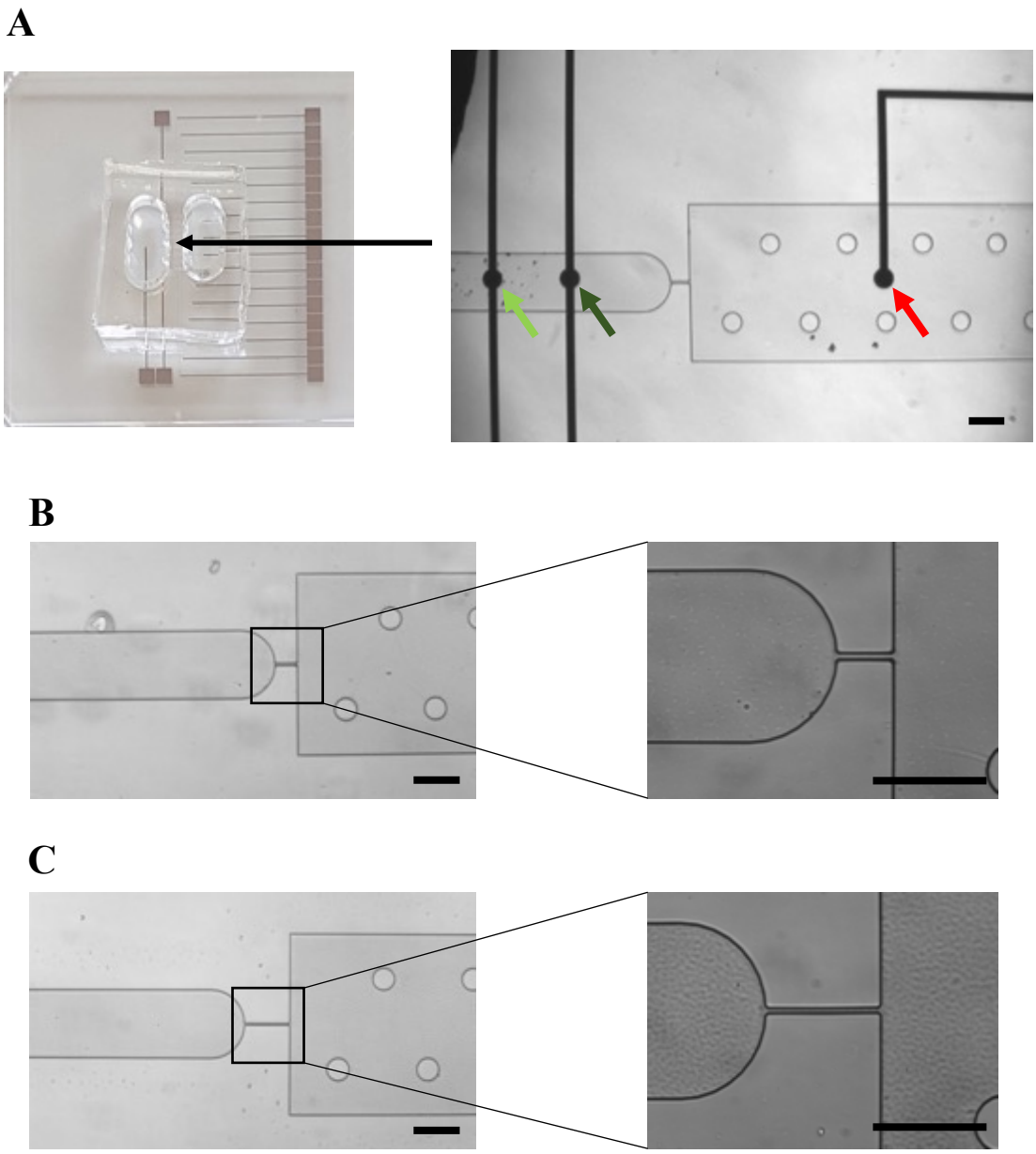

Figure 2.19: Fabricated microchannels in PDMS using quartz photomask. (A) PDMS device with microchannels bonded on top of one of the final version MEAs (left). The microchannels were aligned with the electrode pattern and one such example can be seen in the image to the right. The stimulating (green arrow) and ground (dark green arrow) electrodes are in the compartment to the left of the microchannel with one recording (red arrow) electrode to the right of it. **(B)** Closer view of one microchannel measuring 5 µm in width and 50 µm in length. **(C)** Closer view of one microchannel measuring 5 µm in width and 100 µm in length. Scale bars = 100 µm.

2.4 Discussion

This chapter focuses on the development and fabrication of MEAs and microfluidic microchannels as well as the integration of these into a unitary biochip. In addition, I describe here a simple to fabricate holder recording device that enables recording from many different configurations of MEAs. The increase in availability of commercial MEAs, as well as their vast applications, has led to an increase in research groups that use them as an extra technique to supplement and enhance their results. However, this is usually limited by the prohibitive cost of such systems ranging between £50,000 to £100,000. Companies like Multichannel Systems (Reutlingen, Germany), Axion Biosystems (Georgia, USA) and Alpha MED Scientific (Osaka, Japan) have been developing different systems and configurations of MEAs to suit the needs of different applications. The present system, though limited to 16 channels, cost less than £20,000 to construct.

The most common MEAs and the ones I used, are the standard 60MEAs provided by Multichannel Systems which allow direct cell culture onto them. There are several other MEA types and layouts however, for the purpose of what I was to study none were ideal. The main reason was that the interelectrode distances for the majority of the MEAs provided by Multichannel Systems varied between 30 μm to 200 μm versions. As the aim of the custom MEAs was to measure conduction velocity it was important for the electrodes to be spaced apart optimally to allow for several nodes of Ranvier to be positioned between the stimulating and recording electrodes. Thus, the interelectrode distance had to be greater than 200 μm. Therefore, several designs were developed until the most ideal one was found, which would allow stimulation and recording in order to calculate conduction velocity. This process, as well as that to fabricate custom MEAs, together with the issues that arose and how these were fixed have been addressed in this chapter.

In order to achieve the aims of my research it was necessary to develop microfluidic channels that would ensure the separation of cells and their structures in two different compartments. Microfluidics, just like MEAs, can be used in many different applications due its flexibility in being able to produce micron level structures to accommodate research demands. In this chapter, I show the process of developing a way of separating

cells and their structures by using microchannels that were narrow enough to prevent cells from one compartment to entering the second one.

When put together, custom MEAs and microchannels meant that neuronal cells could be cultured in one compartment where they could then be stimulated, and their processes would grow through the microchannels and into the second compartment where the recording electrodes are situated.

2.4.1 Development of System to Record from MEAs

The first step of my PhD was to acquire the required set up that would allow recording from multiple electrodes and which I could then use for all my futures experiments. Each company who produces MEAs have their own proprietary recording equipment. When looking at the available options such as those from Multichannel Systems, Axion Biosystems and Alpha MED Scientific, it became apparent that the costs of such equipment was much higher than our available budget. Therefore, an alternative method had to be sourced that would still allow for multiple simultaneous recordings. The commercially available set ups are all-in-one systems, consisting of the MEA holder, amplifier and temperature control, integrated together. Therefore, each of these components had to be either fabricated or purchased separately.

The main component of the set-up was the amplifier, and the A-M Systems Model 3600 amplifier had 16-channels which meant that simultaneous recordings from 16 separate electrodes could be carried out. The all-in-one set up from Multichannel Systems has the capabilities of recording from 60 up to 256 electrodes. In our case, 16 electrodes were enough and if needed the set up could be expanded by adding a second 16-channel amplifier.

The holder where the MEAs would be held in place and interfaced with the amplifier was important to be as versatile as possible. The holder's dimensions were set to those of the commercial standard 60MEA by Multichannel Systems, however, the holder size could be adjusted to fit any MEA as long as the pins interfacing the MEA contact pads to the amplifier were of the same layout. In this case the 60 spring pins were arranged in a square by having 16 pins on each side. Spring contact pins were chosen instead of any other interface connectors as they would reduce the chances of damaging the electrode contact

pads after continuous use. Damaging the surface of the contact pad would grant the MEAs useless as the signal obtained would be worse or even non-existent. This pin arrangement allowed for recording from the standard 60MEA (60MEA200/30iR-Ti), however, only from one side at a time due to the 16-channel limitation. The initial recording device functioned adequately but it was quickly decided that a more robust device was necessary. The first recording device required regular maintenance in the form of re-soldering cable connections and making sure the ground connection was in place after every use. Since upgrading the recording device these issues were no longer present as nano strip cables were not soldered on the top of the device to each pin directly. Instead they were 'packaged' inside a female pin connector that interfaced the pins through a male pin connector that was attached onto the top of the device, with one on each side.

An alternative recording device had to be fabricated to be able to interface with the contact pad layout of the custom MEAs. A set layout for the contact pads for all the custom MEAs was chosen and that was 16 contact pads on one side, 2 on another and 1 more on another side (**Figure 2.12A**). Unlike the recording device (RD2) used for the commercial MEAs this device was robust and required no connector changes to be able to record from different sides.

When purchasing an all-in-one system, the software package included allows for viewing the traces of all the electrodes in one window in real time. Possible open source software such as NeuroRighter (Rolston, Gross and Potter, 2009) were tested but it was concluded that the best real-time recording software was Clampex (Molecular Devices, California, USA). The pCLAMP software package included everything necessary for real-time recording from 16-channels and for post processing the data.

2.4.2 Design and Fabrication of Custom MEAs

Initial electrode designs were sent to Epigem, the industrial partner, who then fabricated and sent back the MEAs for testing. The MEAs sent back were initially tested by attempting to culture different cell types on them. After several attempts it was found that the cells would not grow for more than a few days and cell adherence was an issue. Furthermore, after just one use, the gold tracks and electrodes began peeling off and detaching. It was later found out that these MEAs were not properly insulated and the surface layer on which the cells were grown on was SU-8 which was not modified in any

way to be biocompatible and therefore not suitable for cell culture (Xue *et al.*, 2014). The importance of these two features was explained, however, Epigem was unable to provide a solution as they were limited in the equipment available for manufacture.

This led to me having to find an alternative route in obtaining these custom MEAs. Instead of having to outsource the MEAs, the nanofabrication facility at Heriot Watt offered all the necessary equipment to fabricate my custom MEAs in house. The initial designs, V1.0, included 16 stimulating electrodes in parallel to 16 recording electrodes separated by 1 mm. The distance between the recording and stimulating electrode plays an important factor, as if it was too small then that might not be sufficient to obtain any useful data from because there may not be sufficient numbers of nodes of Ranvier between them. The internode length varies throughout the central and peripheral nervous systems. For example, in rat layer V cortex it ranges between 27 μm to 154 μm (Arancibia-Cárcamo *et al.*, 2017).

The V1.0 design was later altered to having 8 groups of 2 recording electrodes in parallel to 8 stimulating electrodes with 8 ground electrodes between them. The distance between the stimulating and first recording electrode was kept at 1 mm. These upgraded designs (V3.0, V3.2 and V3.4) were done to improve the accuracy of the conduction velocity recordings. Knowing the time it takes between an electrical recording and the stimulus artefact allows one to calculate the conduction velocity as the distance between the stimulating and recording electrodes is also known. However, being able to calculate the conduction velocity from the action potentials recorded between two recording electrodes would be more accurate which is why the new designs had recording electrodes in parallel to each other. Therefore, all the custom MEAs from then on included that electrode design layout.

Another alteration was the use of titanium (Ti) instead of gold (Au) for the electrodes. The reasoning behind this was mostly about cost as Ti was a cheap and widely used metal on MEAs (Ghane-Motlagh and Sawan, 2013). Knowing that the surface of the MEA was important in maintaining a healthy cell culture, several different options were looked at before selecting silicon dioxide (SiO_2). It was decided to use SiO_2 instead of any other insulating material as it has a very high dielectric strength and was reported to be biocompatible (Bartzsch *et al.*, 2009).

Initially, the custom MEAs were fabricated using a film photomask to transfer the electrode and insulation patterns onto the photomask. The reason for the non-exposure of the electrodes from those first custom MEAs was most likely due the use of film photomasks which are known to be less reliable when dealing with features below 20 μm (Orabona *et al.*, 2013). It could have also been due to issues with misaligning the photomasks prior to UV exposure as even the slightest misalignment, due to the micron features, meant that the electrodes would end up insulated instead. This issue was resolved once the electrode and insulation patterns were laser etched onto the photoresist instead of using a film photomask. The quality of the deposition was also evaluated by measuring the impedance of each electrode. For some electrodes, the impedance measured was negligible meaning that they were not fully insulated. This could have been due to parts of the track being exposed as some tracks were slightly damaged and not fully formed. The mean electrode impedance of the custom array was 56.7 kΩ (50 μm electrodes). This was comparable to the electrode impedance stated by Multichannel Systems for their 30 μm electrodes which is < 100 kΩ. Increasing the electrode diameter causes a decrease in impedance. Having a lower impedance was important so that there was less electrical interference in the traces, thus a better signal to noise ratio (Nam and Wheeler, 2011).

The deposition layer of Ti and SiO_2 was reduced from the initial 1000 nm and 500 nm down to 150 nm and 100 nm respectively. This was because it was thought that having a difference of at least 500 nm between the electrode and the surface plane may have been an issue with the cells growing over the electrodes. Therefore, reducing the thickness difference between the Ti and SiO_2 to about 50 nm would mean that would not be an issue. However, it was found that changing this did not affect cellular growth over the electrodes as no differences were observed. This seems to be confirmed by previous studies as the difference between the metal and insulating layers varies between several hundred nanometres. For example, one study that also used Ti as the metal but silicon nitride (Si_3N_4) instead of SiO_2 had a difference of 200 nm between the two (Ryynänen *et al.*, 2011).

2.4.3 Design and Fabrication of Microfluidic Microchannels

The custom MEAs were designed in such a way to allow for stimulation of the neuronal cell bodies and recording from the axons. The commercially available MEAs do not have

any way of controlling which cells go where, and as a result they grow across the whole surface without any restriction. Therefore, this was addressed by designing and fabricating microchannels that would restrict neuronal cell bodies to the recording compartment and only allow their processes to grow into the recording compartment.

2.4.3.1 3D Printed Module

Initially, the possibility of using a 3D printed module with embedded microchannels seemed attractive and flexible. The 3D printed module consisted of two compartments separated by a barrier with embedded microchannels. The lowest dimension possible for the microchannels was 100 μm in width and 100 μm in depth. This was due to the resolution limitations by the Ember 3D printer, even though it was stated by Autodesk that 50 μm resolution could be achieved in the X and Y - axes. When we tried printing smaller microchannels (< 100 μm), these did not come out well as the microchannels were irregular and some did not even form properly. Another issue which quickly arose was that when culturing human neural stem cells and mouse AtT20 cells within the 3D printed module the cells did not survive for more than 24 hours. This implied that the resin used was not biocompatible.

2.4.3.2 PDMS Microchannels

Previous studies have shown successful ways of separating different cell structures and cell types in different compartments using microfluidics (Majumdar *et al.*, 2011; Park *et al.*, 2014). Majumdar *et al*., (2011) fabricated a two-chamber module separated by microchannels measuring 100 μm wide and 5 μm high in which they cultured rat dissociated hippocampal neurons in one compartment and glial cells in the other. Park *et al.*, designed a microfludic module where primary CNS neurons from rats were cultured in a central compartment that was connected to six surrounding compartments in which axons would solely grow through. The microchannels separating the compartments measured 20 μm wide, 10,000 μm long and 3 μm high.

These designs were assessed and taken into consideration when designing my microfluidic microchannels. Therefore, the concept was to have one microchannel in between two larger compartments. It was also important for this design to perfectly align over the electrode layout of the custom MEAs. This meant that each custom MEA

electrode layout had to have the same microchannel layout so that it would perfectly align with it. One compartment would align over the stimulating electrode, the other over the recording electrode and the microchannel would be in between the two. The compartment that aligns over the recording electrode was three times bigger than the one over the stimulating electrode as more surface area was needed for the several processes that would be growing into that compartment. Due to its size, this compartment had pillars embedded in it in order to avoid it from collapsing and breaking.

My first microchannels were fabricated using a film photomask for the soft lithography process and measured 10 μm in width. This was at the lower end of the resolution of a film photomask but for a first trial run for scoping the range it was ideal, as film photomasks are cheap, easy to handle and quick to fabricate. The issue with these first microchannels was that the edges of all the features were not smooth. This meant that the microchannels did not have the intended measurements of 10 μm in width and 25 μm in depth. This "roughness" along all the features was most likely caused by the UV light diffracting slightly through the film photomask and causing unwanted regions to become cured. To reduce this "roughness" the film photomask was held in place by adding a weight on top of it, which reduced any movements during the curing process and subsequently reduced any diffracted UV light to hit unwanted areas of SU-8. This made the features less "rough" however not to the extent of those microchannels fabricated using a quartz photomask. Using a quartz photomask instead of a film photomask produced accurate and smooth features.

When testing the initial PDMS devices, it was found that the cells were not always restricted by the microchannels and some were able to flow through and into the second compartment. In order to resolve this, the microchannel dimension had to be reduced. It was therefore decided to update the designs by reducing the width of the microchannels from 10 μm to 5 μm. These updated designs would be the final ones used throughout the whole of my PhD and we decided to have them fabricated on a quartz photomask instead of a film photomask. A quartz photomask allows for a much higher feature resolution below 1 μm, is more robust, and the quality of the design on the silicon master wafer is better than that of a film photomask. The only downside was its cost, which was 5 times that of a film photomask, hence the quartz photomask, was only used once I knew these designs would be the final versions.

The PDMS devices fabricated from the silicon master wafer prepared using a quartz photomask had smooth features and the microchannels measured exactly as they were intended to be. As mentioned, the main aim for reducing the microchannel width was to restrict any cells from flowing from the seeding compartment into the other. This was achieved and shown in more detail in Chapter 3.

2.4.3.3 Microchannel Flow Modelling

Once the PDMS modules were fabricated, holes were punched out on each side making sure to not damage the microchannels in between. The reason for this was to create two well compartments that would allow easy access for seeding cells and media changes (**Figure 2.19A**). Cells were seeded into one compartment and media alone in the other compartment. A higher volume of media was placed in the cell seeding compartment in order to achieve a slow flow from one compartment to another (Park *et al.*, 2012). This gentle flow would guide the cells towards the microchannels where they would be restricted and therefore adhere. However, to my knowledge the flow rates and forces in such channels are not often looked at. To better refine the design and understand the forces potentially acting on cells and their processes we carried out modelling of the flow and pressures in the microchannel designs.

The nature of the flow in the microchannels had two important implications for the later experiments. The lack of laminar flow in the input well means that the cultured cells placed in the feeder compartment for culture would have time to settle and the relatively low flow rate would effectively mimic the static conditions in standard cell culture conditions. Meanwhile, the laminar flow in the microchannels ensured that solution exchange occurred between the two wells compartments.

The flow modelling carried out showed that when the liquid height in one compartment was 6.9 mm and 2.3 mm in the other compartment laminar flow was achieved within the microchannels and the liquid did flow from the higher volume compartment and into the lower volume compartment. An average flow velocity ranging between 6.89 and 13.8 μm/s for the microchannels measuring 5 x 100 μm and 10 x 100 μm respectively was comparable to a previous study which used 2 μm polystyrene monodisperse microspheres to measure flow through channels (16 channels; 85 μm wide, 18 mm long, 45 μm high) which ranged between 7 – 14 μm/s (Millet *et al.*, 2007).

2.5 Conclusions

A more cost-effective way of measuring from MEAs was set-up as well fabricating an adaptable recording device which holds MEAs. Custom MEA fabrication was improved by using a laser writer for patterning the insulation layout instead of photolithography. No more issues with misalignment or complete coverage of the SiO_2 insulating layer was observed since adopting this technique. Microchannel features were improved drastically by replacing the film photomask used during the UV exposure of the soft photolithography process with a quartz photomask. The microchannels fabricated measured the exact dimensions required and the walls were smooth. Finally, the microchannels aligned as expected over the electrodes of the custom MEAs.

Chapter 3

Substrates for Shaping and Monitoring hiPSC Derived Neurons *in vitro*

Abstract

The majority of *in vitro* disease studies are carried out in animal (principally rodent) models. However, since the introduction of human embryonic stem cells (hESCs) and more recently the ethically derived human induced pluripotent stem cells (hiPSCs), these models can now be complimented or even surpassed with the use of human cell lines. In many cases, this may produce results that are much more relevant to human disease. Unfortunately, several significant barriers exist to their large-scale adoption. *In vitro* neurons form axonal processes, synapses and are active but they are not organised into layers and cell body/axon tracts as they are *in vivo*. To begin to address this issue towards developing a model to examine human neurodegenerations, I used differentiated hiPSCs and tried to assess their growth on different surfaces and through microchannels. I successfully differentiated hiPSCs into cortical and dopaminergic neurons which were kept in culture for up to 6 weeks. The cells were cultured on a variety of surfaces, including polystyrene, borosilicate, silicon nitride, silicon dioxide and SU-8. Their electrical properties were analysed using patch clamp electrophysiology, commercial and custom microelectrode arrays (MEAs). Data from these experiments showed that cortical neurons formed no synaptic inputs and were still electrically silent after 4 weeks *in vitro* whereas dopaminergic neurons formed synapses and exhibited spontaneous electrical activity as early as 2 weeks *in vitro*. Microchannels varying in width and length (5 or 10 μm in width and 50 or 100 μm in length) were tested with cortical neurons to see if axonal growth could be induced through them. 5 μm wide microchannels allowed for the separation of the cell bodies of cortical neurons from the axons in two different compartments on polystyrene and borosilicate. This data is an important step in developing stratified models where electrical activity, compartmentalisation of neuronal anatomy and degeneration can be studied *in vitro*.

3.1 Introduction

Animal models have been used for several decades to study human diseases. One example includes experimental autoimmune encephalomyelitis (EAE) which is the most commonly studied animal model for multiple sclerosis (MS) and it is believed to be the closest pathology model of MS (Franklin, 2015). Since the introduction of the EAE model (Rivers and Schwentker, 1935), it has helped us improve our understanding of the mechanisms of MS as well as develop drugs for its treatment (Farooqi, Gran and Constantinescu, 2010). However, animal models do not always reflect the same outcomes when the same drugs are tested on humans. In regard to MS, this is due to there being several differences between human and rodents. For example, in humans, myelination takes decades due to the complexity of the brain, whereas in mice, myelination only takes about 2 weeks (Semple *et al.*, 2013).

Since the discovery of human induced pluripotent stem cells (hiPSCs) (Takahashi and Yamanaka, 2006), it has led to the increase in availability of human cell lines that can be used to develop novel human models. hiPSCs are generated from adult fibroblasts which makes their usage ethical unlike human embryonic stem cells (hESCs) whose use sparked controversy within the scientific community due to the ethics behind their sourcing (Di Ruscio *et al.*, 2015).

Dissociated neuronal *in vitro* cultures are functional and allow for neurons to be investigated pharmacologically and visually. However, these dissociated and 'disorganised' cultures do not offer the same neuronal architecture as *in vivo* studies offer due to the disordered connectivity of neurons (Taylor *et al.*, 2010). Brain slices are an alternative to *in vivo* studies as they offer the same connectivity (Morin *et al.*, 2006). As mixed neural and glial cell co-cultures do not allow the study of localised interactions of axons and glial cells due to the presence of the cell bodies it would be advantageous to grow such cells in a way that would control their topology *in vitro*. One such study, developed a circular compartmentalised microfluidic device that isolated axons from cell bodies allowing the glial cells to only interact with the axons although electrical activity was not measured (Park *et al.*, 2009).

Here, human neural stem cells (hNSCs) were differentiated into cerebral cortical neurons and dopaminergic neurons. They were cultured on commercial and custom microelectrode arrays (MEAs) as well as polystyrene wells and borosilicate coverslips

that were previously pre-coated with either SureBond-XF or laminin. This allowed a detailed evaluation of their excitability and synaptic maturity in long term cultures. This data, alongside that obtained from patch clamp electrophysiology improves our understanding of their electrical behavioural organisation and development *in vitro*. Alongside the successful long-term cultures of the differentiated neurons, hCCNs were grown in a PDMS microfluidic device in which I was able to show that the cell bodies can be separated from the axons. This was an important step in developing a custom MEA that would be able to stimulate the cell bodies and record from the axons.

3.2 Methods

3.2.1 Culture and Expansion of iPSC-derived human neural stem cells

Culture media and hNSCs used were obtained from Axol Bioscience (Cambridge, UK). The hNSCs originated from female newborn cord blood CD34+ cells. For culture and expansion, the protocols provided by Axol Bioscience were followed with slight modifications that are detailed below. Initially, hNSCs were expanded on sterile 6-well tissue culture plates (Corning Inc) that were previously pre-coated with SureBond-XF (Xeno Free) 1x working solution for 4 hours at 37°C. The 1x SureBond-XF was prepared fresh each time from the 200x stock by diluting with D-PBS (without calcium and magnesium). Alternative tests were carried out where instead of pre-coating the culture surface with SureBond-XF, laminin was used at 20 µg/ml and incubated at 37°C for 30 minutes. The hNSCs were plated in Plating-XF medium at a density of 70,000 per cm^2 and incubated for 24 hours before fully replacing with Neural Expansion-XF medium that was freshly supplemented with 20 ng/ml of epidermal growth factor (EGF) and 20 ng/ml of fibroblast growth factor (FGF). Full media changes of Neural Expansion-XF medium were carried out every 2 days up until the culture was 80% confluent and that took about 4 to 6 days to occur. Once confluent, the hNSCs were detached using Unlock-XF medium. Unlock-XF medium was brought up to room temperature and 5 minutes before adding to the hNSCs was warmed in a 37°C bead bath. The hNSCs were washed twice with pre-warmed D-PBS (without calcium and magnesium) before adding 1 ml of Unlock-XF medium (6-well plate). The plate was incubated for 6 minutes at 37°C. The cells were gently transferred into a 15 ml Falcon tube and a 4:1 ratio of pre-warmed Expansion-XF medium to Unlock-XF medium was pipetted to stop the reaction. The cells were centrifuged at 200 x g for 5 minutes. The cell pellet was resuspended in Plating-XF, counted and re-plated into a 6 – well plate for further expansion. The hNSCs were passaged another 2 times (total of 3 passages) before they were cryopreserved in Neural Expansion-XF medium (without any supplements) and 10% dimethyl sulfoxide (DMSO). All the media used was pre-warmed at 37°C and cells were incubated at 37°C and 5% CO_2.

3.2.2 Differentiation of hNSCs to Human Cerebral Cortical Neurons

The protocol provided by Axol Bioscience was followed for differentiation of hNSCs to human cerebral cortical neurons (hCCNs). The required numbers of hNSCs were thawed and seeded at a density of 100,000 cells per cm^2 using Plating-XF medium. A full medium change was carried out using Neural Expansion-XF medium without any growth factors after 24 hours at 37°C. The cells were incubated for a further 24 hours and then another full medium change was carried it using Neural Differentiation-XF medium. Half medium changes with pre-warmed Neural Differentiation-XF medium were done every 3 days. After about 6 to 8 days, once a pure population of hCCNs was reached, half the media was replaced with Neural Maintenance-XF medium. After 24 hours, half the media was again replaced with Neural Maintenance-XF medium and from then onwards half media changes were carried out every 3 days. All the media used was pre-warmed at 37°C and cells were incubated at 37°C and 5% CO_2. The differentiation process was carried out on different surfaces which included polystyrene wells, borosilicate coverslips, silicon nitride Si_3N_4 (commercial MEA, Multichannel Systems), SU-8 (custom MEA V1.0, Epigem) and silicon dioxide SiO_2 (custom MEA V3.0, V3.2 and V3.4).

3.2.3 Differentiation of hNSCs to Human Dopaminergic Neurons

hNSCs were plated at a density of 30,000 cells per cm^2 using Plating-XF medium. Before plating, the polystyrene wells were pre-coated using SureBond-XF following the same steps discussed in section 3.2.1. After 24 hours, a full media change was carried out using STEMdiff™ dopaminergic neuron differentiation medium (STEMCELL Technologies) supplemented with 200 ng/ml of sonic hedgehog (SHH) protein (GF174, Millipore. Full media changes were done daily for 14 days. The cells were then detached and re-plated at a density of 20,000 cells cm^2 onto a SureBond-XF pre-coated surface using Plating-XF medium. The cells were re-plated on commercial and custom MEAs that were plasma treated prior to coating with SureBond-XF. A full medium changed was carried out after 24 hours using STEMdiff™ dopaminergic neuron maturation medium 1. Full media changes were performed every 2 days for 5 days. From day 19 onwards, full media changes were performed using STEMdiff™ dopaminergic neuron maturation medium 2 every 2 days. All the media used was pre-warmed at 37°C and cells were incubated at 37°C and 5% CO_2.

3.2.4 Microelectrode Electrophysiology

Recordings were obtained from 0 to 4 weeks hCCNs in the whole cell configuration at room temperature (20°C). Microelectrodes were pulled from borosilicate glass using a Flaming/Brown P-87 micropipette puller. The microelectrodes were pulled to a resistance ranging between 3 to 7 MΩ. Intracellular and extracellular solutions were prepared following those used in previous literature and already established in the Brown Lab. Intracellular solution (mM): 120 K-Gluconate, 25 KCl, 4 MgATP, 2 NaGTP, 10 EGTA, 1 CaCl2 and 10 HEPES, 290 Osm/kg, pH 7.2. Extracellular solution (mM): 129 NaCl, 5 KCl, 2 CaCl2, 1 MgCl2, 30 Glucose, 25 HEPES, 311 Osm/kg, pH 7.4. The osmolarity was checked using an automatic cryoscopic osmometer OSMOMAT 030 (Gonotec). If the osmolarity was higher than wanted it was reduced by adding distilled water, if it was lower, sucrose was added to increase it.

Three protocols were used to acquire relevant data:

1) Voltage clamp recording from a holding potential of -60 mV to + 60 mV in 200 ms + 10mV steps. This was used to obtain current-voltage (I/V) relationships and current densities for sodium channels.
2) Current clamp recording from a holding potential of -60 mV, with a 25 pA current step and the steps were 250 ms in duration. This was done to determine the ability of a cell to fire action potentials upon current injection.
3) Continuous voltage clamp recording from a holding potential of -60 mV. This was used to detect synaptic potentials and the presence of functional synapses.

Data analysis: All data acquired was analysed offline using WinWCP V5.54 (open source, Strathclyde Electrophysiology Software) and Clampfit 10 and 11.1 software for Windows (Molecular Devices Corporation, California, USA).

The data obtained through patch clamp were exported from WinWCP as an .abf file in order to be recognised by Clampfit which is where they were later analysed.

3.2.5 Recording from Commercial MEAs

hNSCs were plated at a density of 100,000 cells per cm^2 on the commercial 60MEA200/30iR-Ti-gr MEA's (Multichannel systems). The hNSCs were differentiated and maintained in culture following the protocols from sections 3.2.2 and 3.2.3. A fluorinated ethylene-propylene (FEP) membrane (ALA MEA-MEM-SHEET) was placed over the ring of the MEA and secured in place using an O – ring. This allowed for the culture to remain sterile when using the MEA outside of the tissue culture hood. The membranes are permeable to CO_2 and O_2 and can therefore be kept on the MEA's throughout the whole experimental time period. FEP membrane covers were removed only when changing media.

The membrane sealed MEA was then placed into the holder of the recording device (RD2) and left for 5 minutes in order for the temperature to be at 37°C before beginning the recordings. A one-minute gap-free protocol was set up on Clampex 10 software. To avoid any loss of electrical recordings, the low and high pass filters of the amplifier were adjusted until the optimal range was found. The settings used on the A-M systems Model 3600 amplifier were 3 Hz high pass filter, 1 kHz low pass filter, x20,000 gain, notch filter on and GND setting selected. Two recordings were acquired from each side of the MEA, for a total of eight. Representative images of each side were also taken using the Retiga R1 camera and Micro-Manager Open Source Microscopy Software. Once done, the MEAs were placed back into the incubator for future use. The MEAs were carefully transported to avoid as much disturbance as possible. This process was repeated for all commercial MEA recordings.

3.2.6 Recording from Custom MEAs

Before culturing cells on the custom MEAs, the PDMS module containing the microchannels had to be aligned with the electrodes. The custom MEAs together with the PDMS modules were plasma coated to ensure better bonding of the PDMS onto the surface of the MEA. The microchannels were then aligned over the electrodes by hand using a compound microscope. hNSCs were seeded in one of the compartments whilst the second compartment only contained media. To ensure the flow from one compartment to the other, the volume in the cell contained compartment was higher than that of the second compartment (300 µl : 100 µl). The hNSCs were cultured and differentiated

following the same protocols detailed in sections 3.2.2 and 3.2.3. An FEP membrane was also placed over the PDMS modules before transporting the custom MEAs for recording. The custom MEAs were placed into their dedicated recording device and the same recording protocol as detailed in section 3.2.5 was used.

3.2.7 Analysis of MEA Recordings

All data acquired was analysed offline using Clampfit 10 and 11.1 software for Windows (Molecular Devices Corporation, California, USA) and Excel 2019 (Microsoft, Washington, USA).

Each data file consisted of 16 traces, representing a single recording from 16 separate electrodes. Before further analysis, all traces were filtered using a lowpass Boxcar filter with smoothing points set to 15. To separate the 'fast' from the 'slow' waveforms, the threshold search tool was used. The baseline was set to 0 and the trigger marker was set below the peaks of the spikes. For example, if the trigger marker was set to 50μV, any spike above that was selected. The pre- and post-trigger lengths were both set at 1 ms (millisecond). In the event rejection section, the minimum allowed duration was set at 0.1 ms and the maximum allowed duration at 3 ms. With these values set, the threshold search was run, and all events detected were then saved. The waveforms sorted within this range were classified as 'fast' and the ones that did not were classified as 'slow'. The half-width data produced from this search were copied into Excel for further analysis. This was repeated for all other traces analysed.

For 'slow' waveforms, a template search was carried out. Firstly, the traces were decimated by a factor of 10 in order to increase the sampling interval so that a template could be created. Then, a representative waveform was selected to create a template. That template was then used in the template search to scan through the trace and select all waveforms resembling it. All the waveforms collected for that trace were then saved for further analysis. A new template had to be created for each trace analysed. The individual waveforms detected were then averaged to produce an average waveform representative of that week *in vitro*.

3.2.8 Immunocytochemistry

Coverslips were washed with PBS pre-warmed to 37°C before fixation in 4% paraformaldehyde for 10 minutes at room temperature (RT; 20°C). Following fixation, the coverslips were washed 3 times with ice cold PBS and the cells were then permeabilised with 0.1% Triton X-100 for 10 minutes at RT. The coverslips were subsequently washed 3 times for 5 minutes each time with PBS containing 0.1% Tween-20 at RT before a 30 minute incubation at RT in PBS containing 1% BSA and 0.1% Tween-20. This step was done to prevent non-specific antibody binding. After this, the primary antibody was diluted in PBS containing 1% BSA and 0.1% Tween-20 and added to cells which were incubated for 1 hour at RT. The coverslips were then washed 3 times for 5 minutes each time with PBS containing 0.1% Tween-20 at RT. The secondary antibodies were diluted in PBS containing 1% BSA and added to the cells which were incubated for 1 hour at RT in the dark. All secondary antibodies were conjugated to AlexaFluor fluorescent dyes. Coverslips were then washed 3 times for 5 minutes each time with PBS in the dark at RT. Cells were then incubated for 1 min in the dark following the addition of 0.1 μg/ml DAPI. Finally, the coverslips were washed with PBS 3 times at RT in the dark before they were mounted on glass microscope slides with the mounting medium Mowiol® 4-88. The slides were then stored at 4°C until analysis. All reagents were acquired from Sigma-Aldrich and all antibodies were from Abcam. A list of antibodies used and their dilutions can be found in **Table 3.1.**

3.2.9 Drugs and Compounds

All drugs used were diluted from concentrated stock and pipetted directly to the MEA. The drugs used were: tetrodotoxin (TTX; 1 μM; Tocris, 1069) and triethylammonium (TEA, 10 μM; Sigma-Aldrich, 471283).

Table 3.1: **Table illustrating the primary and secondary antibodies used, their description and the dilutions used.**

Primary Antibody	Description	Concentration	Secondary Antibody	Concentration
Anti-Tbr1	Species: Rabbit. Antibody against a cortical neuron marker in layer 6 of cortex.	1:200	Goat anti-Rabbit AlexaFluor-647	1:500
Anti-PSD-95	Species: Mouse. Antibody against a human postsynaptic marker associated with NMDA receptors	1:1000	Donkey anti-Mouse AlexaFluor-488	1:500
Anti-Synaptophysin	Species: Rabbit. Antibody against a ubiquitously expressed presynaptic marker	1:1000	Goat anti-Rabbit AlexaFluor-647	1:500

3.2.10 Graphs and Statistics

All graphs and statistical analysis were carried out in Prism 8 (GraphPad Software, San Diego, USA). Data were tested for normality in order to choose appropriate statistical tests. For parametric and multiple independent samples, a one-way ANOVA was performed. For non-parametric and multiple independent samples, a Kruskal-Wallis test with a Dunn's multiple comparisons test was performed. Statistical significance was accepted at probabilities of equal to or less than 0.05. A p-value of less than 0.05 is shown as a single asterisk (*). Data are presented as the mean ± standard deviation or the standard error of the mean (SEM) for the error bars.

3.3 Results

3.3.1 Immunocytochemical Characterisation of Human Cerebral Cortical Neurons

To determine if the human cerebral cortical neuron (hCCN) differentiation protocol was producing human cortical-like neurons, the cultures were stained for Tbr1, an early cortical neuron marker. At week 0, pre-differentiation, the cultures did not express Tbr1. Tbr1 positive neurons were identified from week 1 with the percentage of Tbr1 positive cells being nearly 100% (n = 4). By week 4, the population of hCCNs increased and the density was about 90%. The cells at week 4 still expressed Tbr1 and again Tbr1 positive neurons consisted of nearly 100% of the culture (n = 4) (**Figure 3.1**).

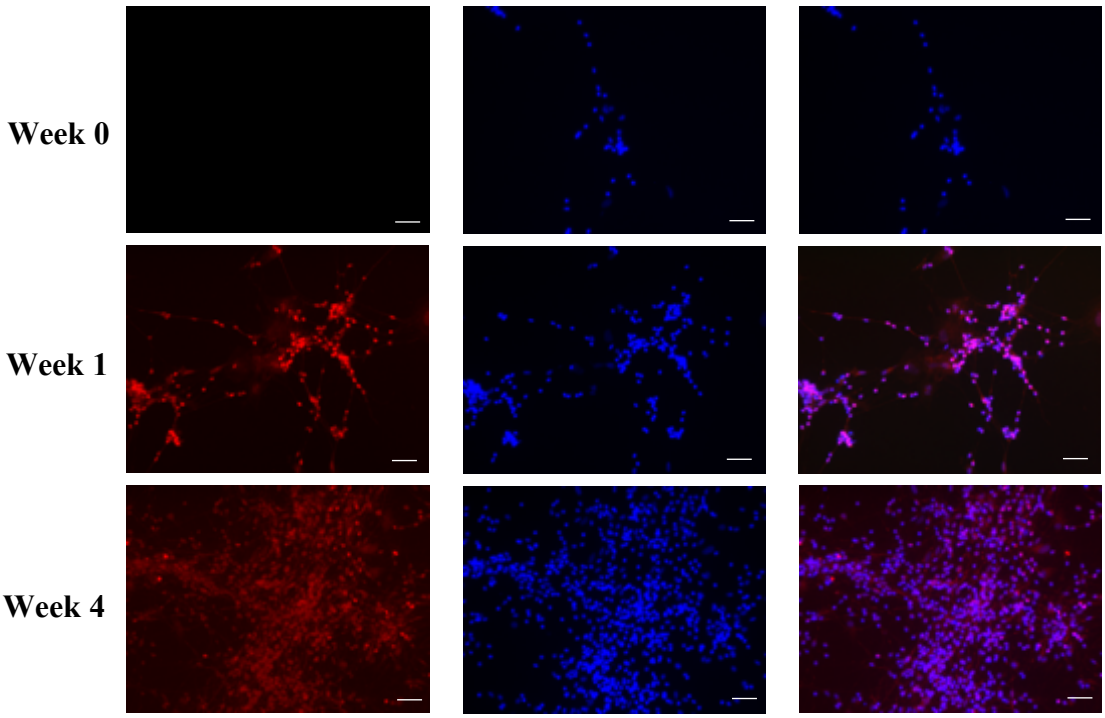

Figure 3.1: **Immunocytochemistry of differentiated cerebral cortical-like neurons.** Human neural stem cells were differentiated into cerebral cortical neurons and cultured for 4 weeks. Cultures were immunostained for the cortical neuron marker Tbr1 (red) and a nuclear stain DAPI (blue). The third column is a merged image of Tbr1 and DAPI. At week 0, the cultures were human neural stem cells and not yet differentiated, hence no Tbr1 expression. Tbr1 expression was observed from as early as week 1 (n = 4). Scale bar = 50 µm.

3.3.2 Culture of Human Neural Stem Cells on Different Surfaces

The hNSCs adhered and were able to proliferate over time when cultured on polystyrene pre-treated with SureBond-XF (Axol Bioscience, Cambridge, UK) (**Figure 3.2A**). However, this was not the case on the commercial MEAs. Unlike polystyrene wells, the surface of the commercial MEA consisted of silicon nitride. The culture of hNSCs on commercial MEAs was problematic as the hNSCs did not adhere onto the surface of the MEA in the same way as they did on a tissue culture treated polystyrene well. The MEAs were pre-treated with SureBond-XF before plating the hNSCs but after 1 day *in vitro* (DIV) the morphology of the culture was not like that of hNSCs cultured on polystyrene. More cellular debris was present in the MEAs after 1 DIV and the cells adhered did not have distinct cell bodies and processes. After 3 DIV, the cell density present on the MEAs was below 25% which was much lower than what was seen with the cultures on polystyrene (**Figure 3.2B**). On polystyrene, after 3 DIV the cell density observed was over 75%.

Pre-treating the culture surface with laminin instead of SureBond-XF had no positive effects as the same outcome was found on the commercial MEAs. There was again a reduction cell density at 3 DIV and the morphology of the cells at 1 DIV was similar to that of the cultures using SureBond-XF (**Figure 3.3B**). The hNSCs culture on laminin treated polystyrene had a similar morphology to those cultured on SureBond-XF treated polystyrene at 1 DIV. However, by 3 DIV, the laminin cultures did not proliferate to the same extent as the SureBond-XF cultures. The cell density at 3 DIV of the laminin cultures remained below 50%, on similar levels as 1 DIV (**Figure 3.3A**).

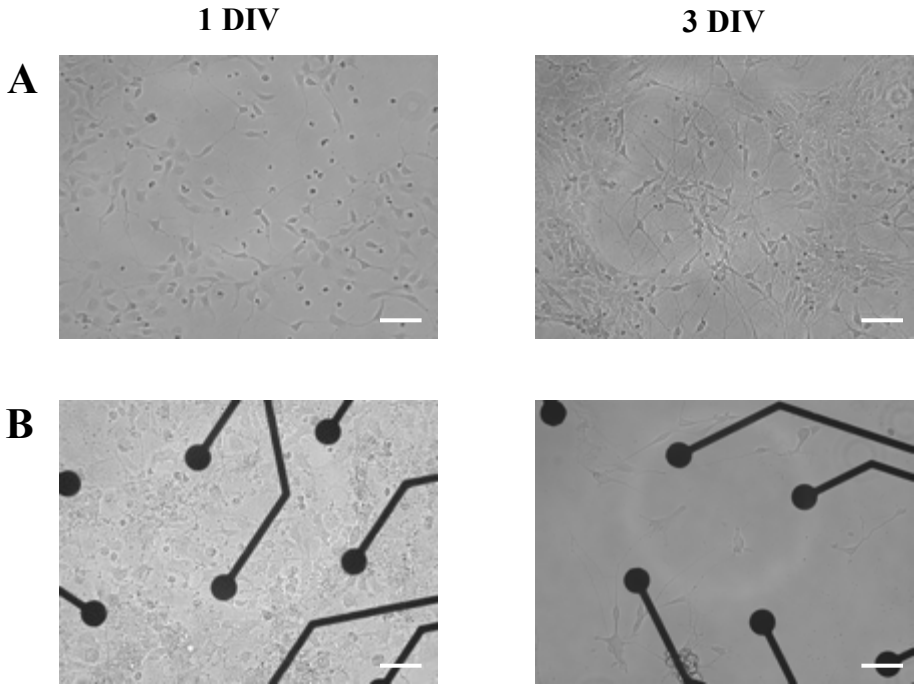

Figure 3.2: Culture of human neural stem cells on SureBond-XF coated polystyrene and commercial MEAs. (A) hNSCs cultured on tissue culture treated polystyrene wells at 1 (left) and 3 (right) days *in vitro*. **(B)** hNSCs cultured on commercial MEAs (silicon nitride surface) at 1 (left) and 3 (right) days *in vitro*. Scale bar = 50 µm.

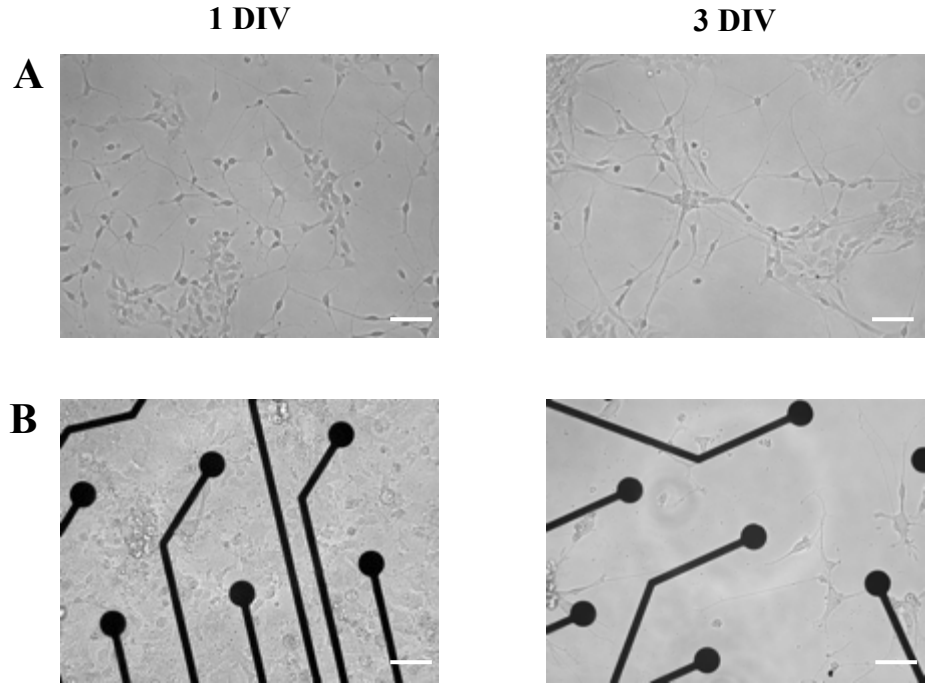

Figure 3.3: **Culture of human neural stem cells on laminin coated polystyrene and commercial MEAs. (A)** hNSCs cultured on tissue culture treated polystyrene wells at 1 (left) and 3 (right) days *in vitro*. **(B)** hNSCs cultured on commercial MEAs (silicon nitride surface) at 1 (left) and 3 (right) days *in vitro*. Scale bar = 50 µm.

3.3.3 Culture and Differentiation of Human Neural Stem Cells in Microchannels

hNSCs were successfully cultured and differentiated through polydimethylsiloxane (PDMS) microchannels that were bonded onto pre-treated with SureBond-XF polystyrene wells and borosilicate coverslips. The cells were only plated into the left-hand side compartment (**Figure 3.4A**). During and after differentiation (by week 1) an increase in axonal length was observed. The axons extended from the first compartment, through the microchannels and into the second compartment (**Figure 3.4B and 3.4C)**

The first PDMS microchannels that were tested did not provide complete restriction of the cell bodies, which caused a number of cell bodies to pass through and adhere into the second compartment (**Figure 3.4B**). The microchannels were designed to measure 10 μm in width, 100 μm in length and 25 μm in height. However, due to the 'roughness' of the walls, the microchannel width varied and measured between 10 to 20 μm. The issue of the cell bodies passing through into the second right-hand side compartment was resolved by reducing the width of the microchannels to 5 μm. The 5 μm microchannels were fabricated using a quartz photomask instead of a film photomask which solved the issue of the 'roughness' (**Figure 3.4C**). No cell bodies were present in the second compartment of the 5 μm PDMS microchannels as all of these were restricted by the microchannels to the left-hand side compartment. Only axons were observed to grow through the microchannels and in the right-hand side compartment (**Figure 3.4C**). The differentiated hCCNs were maintained for up to 2 weeks in polystyrene wells and up to 5 weeks on borosilicate coverslips that were pre-treated with SureBond-XF.

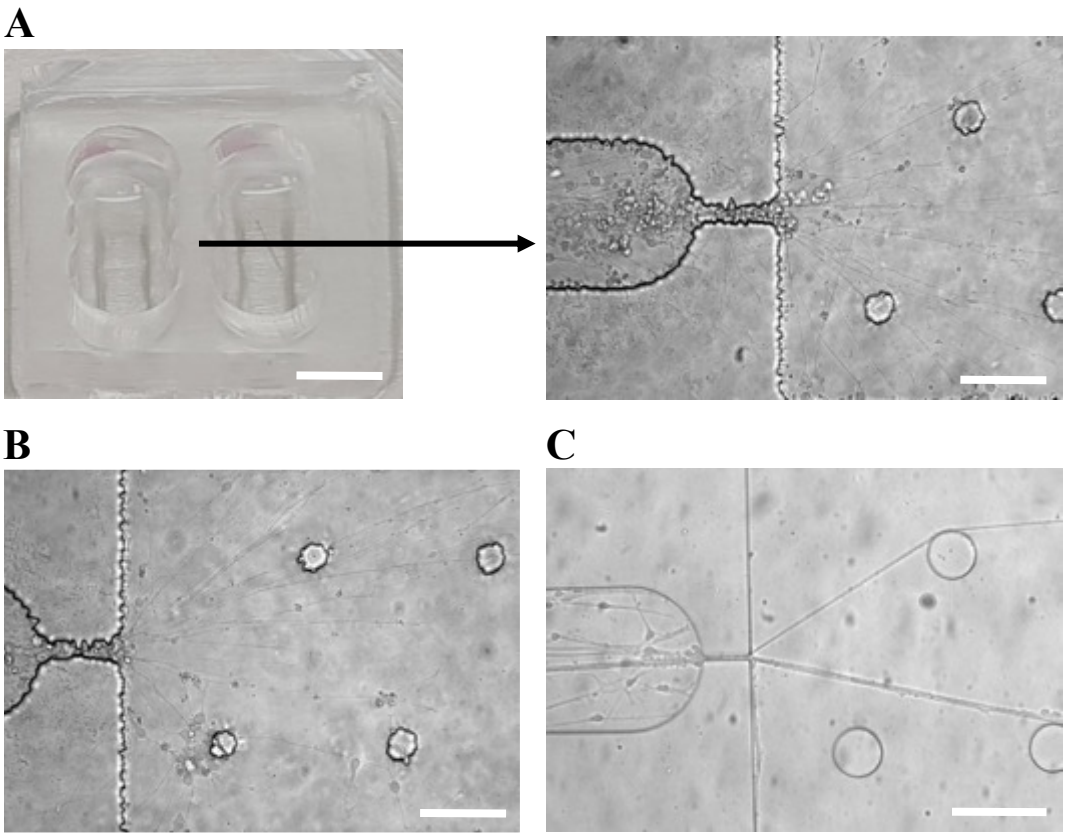

Figure 3.4: Human cerebral cortical neurons cultured in PDMS microchannels. (A) PDMS module bonded (left; scale bar = 500 μm) onto polystyrene with two compartments separated by microchannels (right; scale bar = 100 μm). Human neural stem cells seeded only into left compartment and differentiated into cerebral cortical neurons. **(B)** Axonal growth into second compartment but also cell bodies were able to pass through microchannel and adhere in the second compartment. The first microchannels fabricated had a variable width between 10 to 20 μm (n = 6). The differentiated hCCNs were maintained for up to 2 weeks on polystyrene wells**. (C)** Cerebral cortical neurons cultured in upgraded microchannels with a 5 μm width. Cell bodies remained in the left compartment and only the axons were able to growth through the microchannels and into the second compartment (n = 6). The differentiated hCCNs were maintained for up to 5 weeks on borosilicate coverslips. Scale bar = 100 μm.

3.3.4 Development of Ion Channels and Synaptic Inputs

In this section the development of electrical maturity of axons, and the formation of synapses were followed in hCCN and human dopaminergic neuron cultures using conventional electrophysiology.

3.3.4.1 Ion Channels

Voltage sensitive sodium currents were identified in all hCCNs from week 0 to week 4 (n = 25) (**Figure 3.5A and 3.5B**). The addition of 1 μM TTX to the extracellular solution resulted in the blocking of these sodium currents after 5 minutes (**Figure 3.5C**). The channels were identified in all the human dopaminergic neurons from week 0 to week 4 (**Figure 3.6A and 3.6B**). The currents were also blocked by the addition of 1 μM TTX and 10 μM tetraethylammonium (TEA) to the extracellular solution (**Figure 3.6C**).

When corrected for whole cell capacitance, the sodium current density increased from weeks 0 to 4 and from weeks 0 to 6 in hCCNs and human dopaminergic neurons (tyrosine hydroxylase positive, TH+) respectively (n = 4 to 7 for hCCNs per time point; n = 3 to 8 for TH-positive or negative cells per time point) (**Figure 3.7A and 3.7B**). In regard to hCCNs, the performance of a Kruskal-Wallis test indicated that for voltage-gated sodium (Na_V) currents the increase of time in culture on current density was significant ($p = 0.016$). The increase in current density of Na_V currents from week 0 to week 4 was found to be statistically significant (Dunn's multiple comparison test) as $p = 0.0278$. No statistical difference was found when comparing the other weeks with each other as $p > 0.05$ (**Figure 3.7A**).

When differentiating hNSCs to dopaminergic neurons, about 25% of the cultures consisted of dopaminergic neurons. Both TH+ and TH- cells had voltage-sensitive currents. A one-way ANOVA showed that for Na_V currents, the effect of time in culture on current density was significant for TH+ cells but was not significant for TH- cells (TH+: $p < 0.0001$; TH-: $p = 0.326$). A two-sided Dunnett test showed that for TH+ cells, the Na_V current density was significantly different between week 0 and week 6 ($p = 0.002$). No statistical difference was observed when comparing the other weeks as $p > 0.05$ (**Figure 3.7B**).

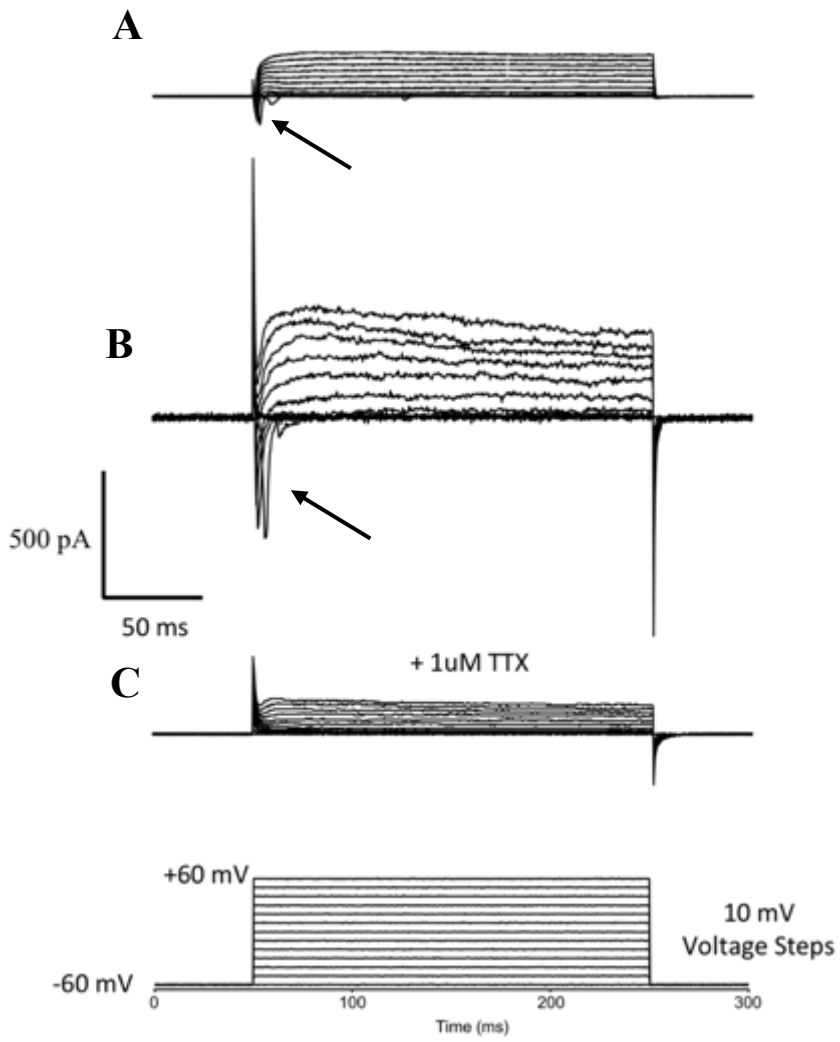

Figure 3.5: **Voltage-dependent currents in human cerebral cortical neurons**. Representative whole cell voltage clamp recordings showing voltage dependent sodium currents (arrow) at **(A)** 0 weeks (n = 4) and **(B)** 4 weeks *in vitro* (n = 4) **(C)** Representative whole cell voltage recording after 5 minutes since the addition of 1 μM TTX. Experimental protocol used shown in the bottom panel.

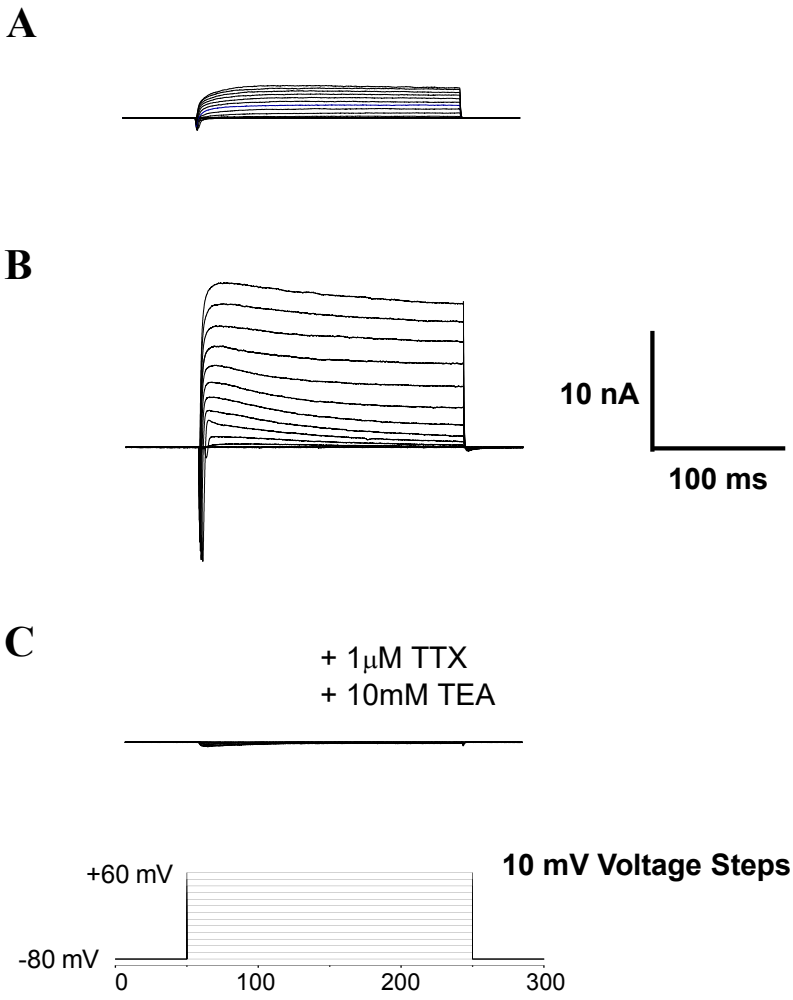

Figure 3.6: **Voltage-dependent currents in human dopaminergic neurons.** Representative whole cell voltage clamp recordings showing voltage dependent currents at **(A)** 0 weeks and **(B)** 6 weeks *in vitro*. **(C)** Representative whole cell voltage recording after the addition of 1 μM TTX and 10 mM TEA. Experimental protocol used shown in the bottom panel. (Figure from Euston, 2017).

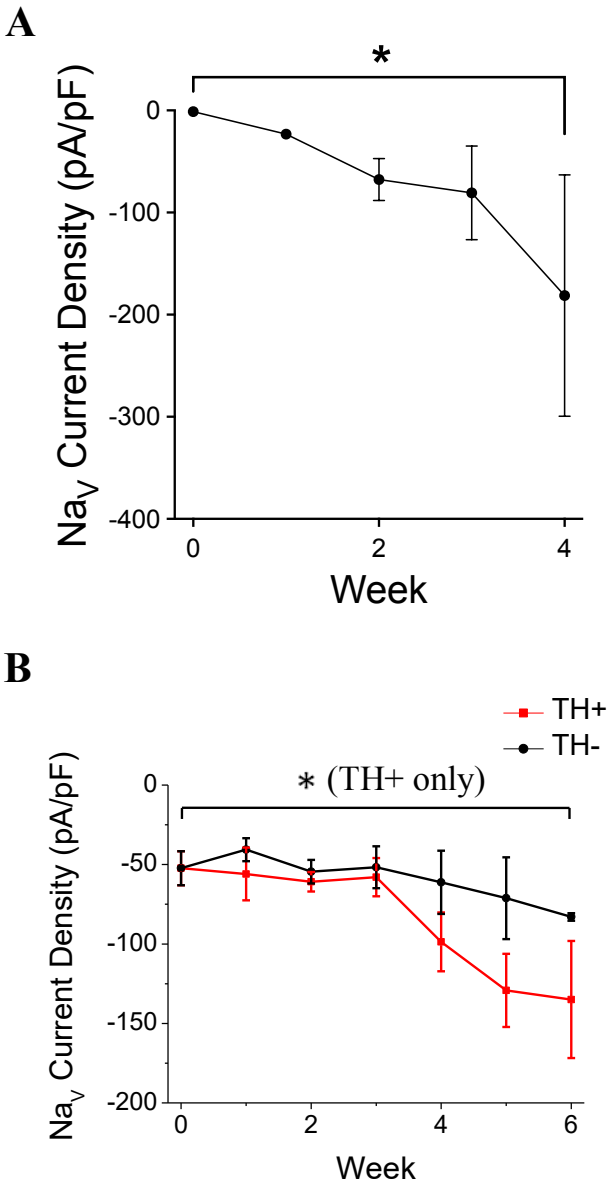

Figure 3.7: **Na_V current properties in human cerebral cortical and dopaminergic neurons. (A)** Mean Na_V current densities of hCCNs from weeks 0 to 4. **(B)** Mean Na_V current densities of TH+ and TH- cells from weeks 0 to 6. Data are presented as the means ± SEM. Statistical significance, $p < 0.05$ indicated by *. (B from Euston, 2017).

3.3.4.1 Synaptic Inputs

hCCNs were co-stained with the presynaptic marker synaptophysin and the NMDA receptor associated protein PSD-95 at 4 weeks in order to determine if they form synapses. The same co-stain was carried out for human dopaminergic neurons at 6 weeks post differentiation. Neither PSD-95 or synaptophysin were expressed by hCCNs at 4 weeks (**Figure 3.8A**), however, staining was seen for both in dopaminergic neurons at 6 weeks (**Figure 3.8B**).

To determine the electrical presence of synaptic currents, hCCNs were held at -60 mV potential in the whole-cell voltage clamp configuration. Cells were sampled from weeks 0 to 4. No excitatory spontaneous postsynaptic currents (ESPCs) were observed in all the cells tested between week 0 to 4 (Figure 3.9A) (n = 25). As expected, this was not the case for dopaminergic neurons. ESPCs were observed from as early as week 2 in both dopaminergic neurons and TH- cells. The percentage of cells with synaptic currents varied between 50% and 75% in dopaminergic neurons from week 2 to week 6 (**Figure 3.9B**).

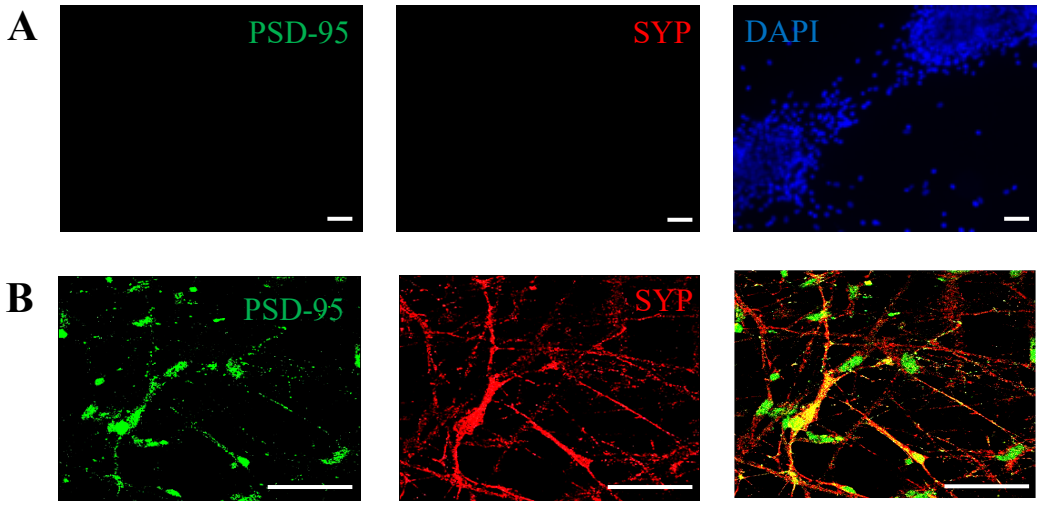

Figure 3.8: **Human cerebral cortical neurons form no synapses in culture. (A)** Representative images of hCCNs co-stained with the postsynaptic marker PSD-95, presynaptic marker synaptophysin (SYP) and DAPI. **(B)** For comparison, representative images of human dopaminergic neurons co-stained for PSD-95 and synaptophysin. Right most image is a composite of the PSD-95 and synaptophysin staining. Scale bar = 50 µm. (B from Euston, 2017).

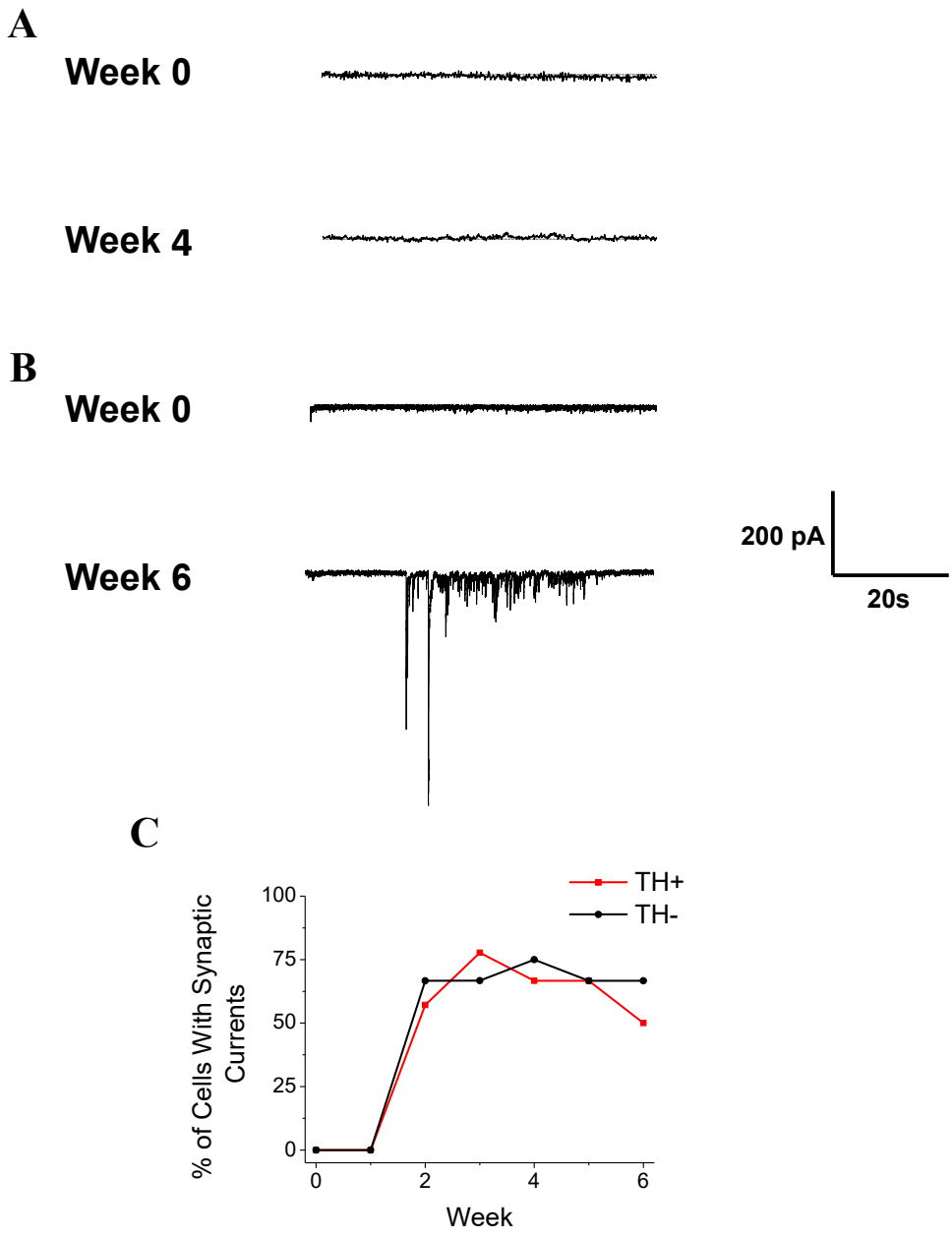

Figure 3.9: **Synaptic currents in human cerebral cortical and dopaminergic neurons. (A)** Representative whole cell voltage clamp recordings from a holding potential of -60 mV of hCCNs at week 0 and 4. Traces indicate no development of ESPSCs. **(B)** Representative whole cell voltage clamp recordings from a holding potential of -80 mV of human dopaminergic neurons at weeks 0 and 6. Trace at week 6 indicates the development of ESPCs in dopaminergic cultures. **(C)** Graph showing percentage of TH+ and TH- cells that display synaptic currents. Synaptic currents are present from week 2 onwards. (Figure from Euston, 2017).

3.3.5 Activity of Human Dopaminergic Cultures culture on MEAs

Unlike hCCNs, I was able to maintain human dopaminergic cultures over 4 weeks *in vitro* on both commercial and custom MEAs (**Figure 3.10A - C and Figure 3.11A - C**). The hNSCs were differentiated on polystyrene wells and were detached and re-plated onto the commercial and custom MEAs at 2 weeks. The human dopaminergic cultures were maintained for up to 6 weeks on the MEAs. The cultures were tested from week 4 to 6. As expected, the dopaminergic cultures were spontaneously excitable from week 4. Electrical activity was recorded on both commercial and custom MEAs throughout the period they were cultured on them (between 4 and 6 weeks). The representative traces, at each week shows how highly active the dopaminergic cultures are (**Figure 3.10D and 3.11D**).

The results from the commercial and custom MEAs were pooled together in order to analyse the electrical activity observed and the waveform characteristics. At week 4, 55.5% ± 7.4% (mean ± standard error of mean) of the channels were active (n = 6). One electrode on the MEA equates to one channel. The percentage of active channels at weeks 5 and 6 were 47.9% ± 20.6% and 73.2% ± 14.6% respectively (**Figure 3.12A**). A Kruskal-Wallis test with a Dunn's multiple comparisons test was carried out but no statistical significant differences were found between the three weeks as $p > 0.05$.

The electrically active channels were further analysed in a way to classify 'fast' and 'slow' waveform activity. Waveforms that were within 0.1 ms and 3 ms in duration were classified as 'fast' and the remaining as 'slow' (**Figure 3.12B**). The percentage of active channels containing 'fast' and 'slow' waveform activity was fairly similar between 4 to 6 WIV as it ranged between 27.1% to 30.7% and 69.3% to 72.9% respectively (**Figure 3.12C**).

The half-width of the 'fast' and 'slow' waveforms indicated that the 'fast' activity recorded between 4 to 6 WIV was similar (**Figure 3.13**) unlike that of the 'slow' activity which became narrower with time (**Figure 3.14**). The half-width is measured as the width halfway from the peak amplitude (**Figure 3.13A;** dashed line). The number of 'fast' waveforms detected from one representative channel at 4, 5 and 6 WIV (**Figure 3.13A; left**) were then averaged to form one waveform (**Figure 3.13; right**). The half-width measured at 4 WIV was 0.12 ms + 0.004 ms (mean ± standard error of mean; 8 spikes),

at 5 WIV was 0.13 ms ± 0.006 ms (9 spikes) and at 6 WIV was 0.12 ms ± 0.007 ms (6 spikes). No statistical significance was found between the 'fast' waveforms at 4 to 6 WIV as $p > 0.05$ (One-Way Anova with a Holm-Sidak's multiple comparisons test).

The number of 'slow' waveforms detected from one representative channel at 4, 5 and 6 WIV (**Figure 3.14A; left**) were then averaged to form one waveform (**Figure 3.14; right**). The average half-widths of 'slow' waveforms was reduced with time. The half-width measured at 4 WIV was 100.0 ms + 7.5 ms (mean ± standard deviation; 20 spikes), at 5 WIV was 72.6 ms ± 3.6 ms (15 spikes) and at 6 WIV was 39.3 ms ± 2.1 ms (31 spikes). A Kruskal-Wallis test with a Dunn's multiple comparisons test was carried out and the difference in half-widths between 4 and 5 WIV was not significant ($p = 0.0837$). The decrease in half-width between 4 and 6 WIV was highly significant ($p < 0.0001$; Kruskal-Wallis test with a Dunn's multiple comparisons test). The decrease in half-width between 5 and 6 WIV was also highly significantly different ($p < 0.0001$; Kruskal-Wallis test with a Dunn's multiple comparisons test).

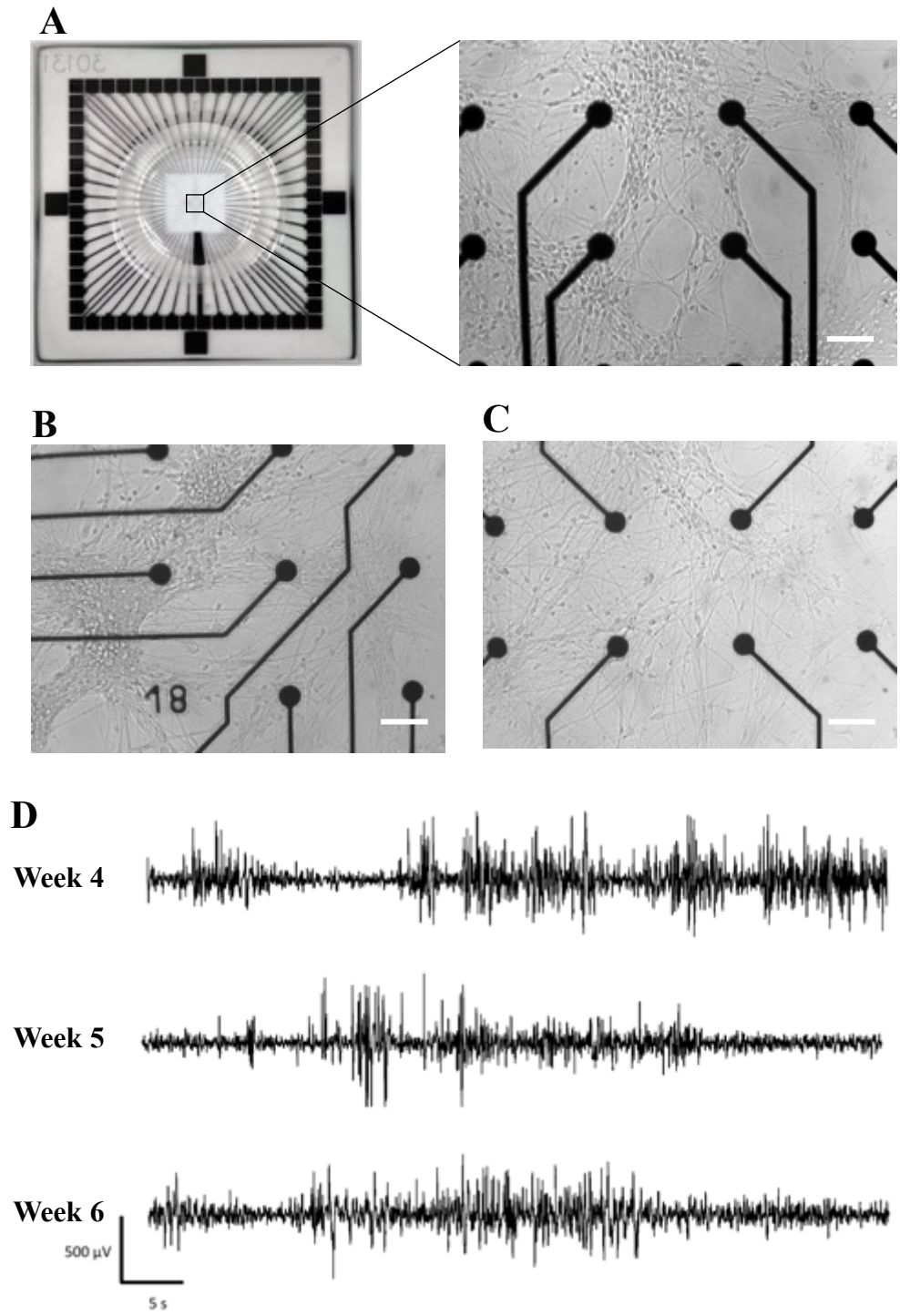

Figure 3.10: **Spontaneously excitable human dopaminergic cultures recorded on commercial MEAs. (A)** Commercial standard MEA used (left) for measuring electrical activity of human dopaminergic cultures. Representative image of culture at 4 weeks (right). Representative images of dopaminergic cultures at **(B)** 5 weeks and **(C)** 6 weeks. Scale bar = 50 µm. **(D)** Representative trace of one active electrode showing that the cultures are highly excitable between 4 to 6 weeks *in vitro*.

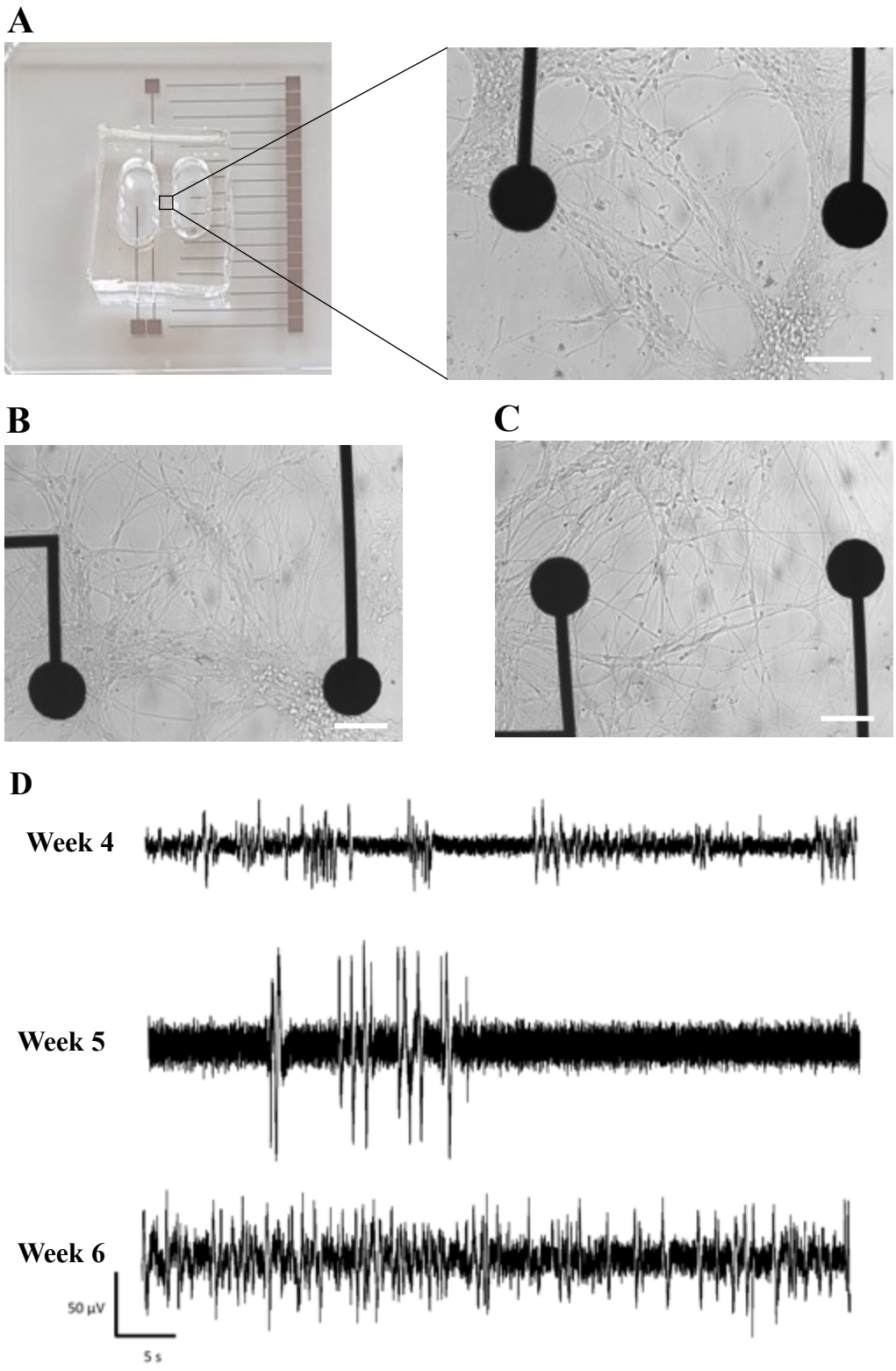

Figure 3.11: **Spontaneously excitable human dopaminergic cultures recorded on commercial MEAs. (A)** Custom MEA used (left) for measuring electrical activity of human dopaminergic cultures. Representative image of culture at 4 weeks (right). Representative images of dopaminergic cultures at **(B)** 5 weeks and **(C)** 6 weeks. Scale bar = 50 µm. **(D)** Representative trace of one active electrode showing that the cultures are highly excitable and bursting activity between 4 to 6 weeks *in vitro*.

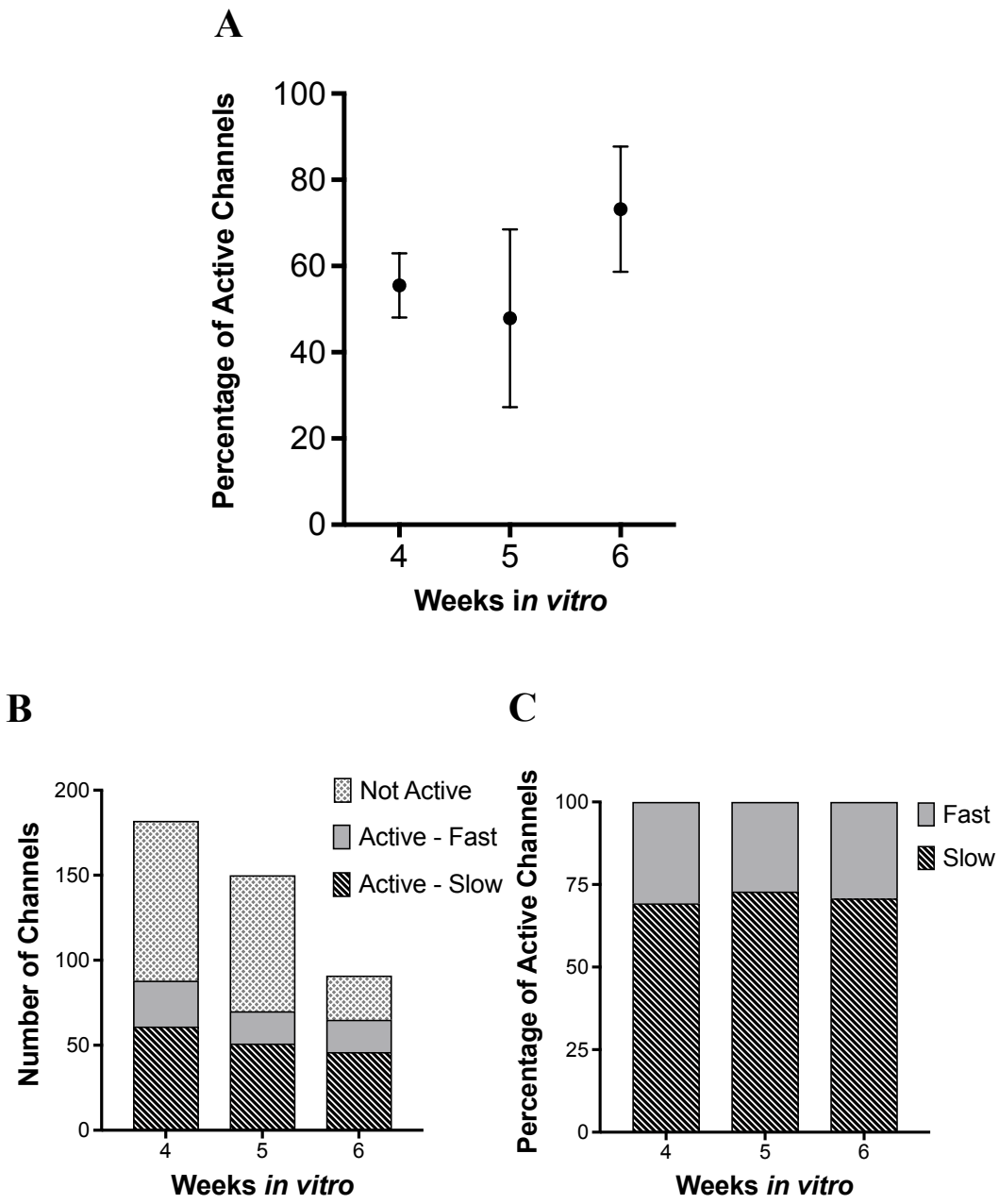

Figure 3.12: **Electrical activity recorded from human dopaminergic neuron cultures on commercial and custom MEAs. (A)** Percentage of electrically active channels at 4 (n =6), 5 (n =4) and 6 (n = 3) weeks *in vitro.* **(B)** Active channels were classified as having 'fast' (0.1 ms to 3 ms duration) and 'slow' (greater than 3 ms duration) waveform activity. (**C**) Percentage of active channels that had 'fast' and 'slow' waveform activity remained on about the same levels throughout weeks 4 to 6. Data are presented as the mean and standard error of the mean used for error bars.

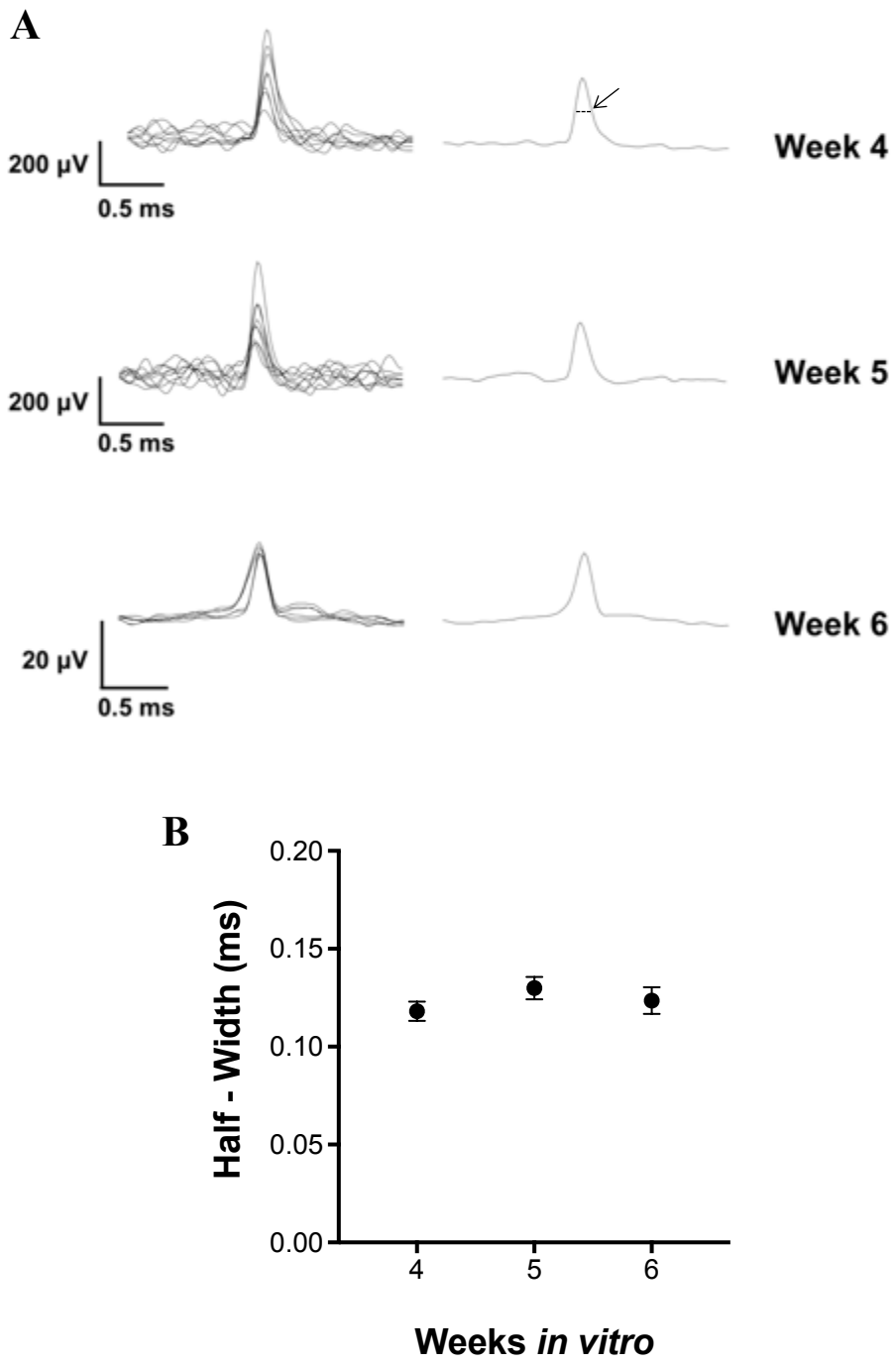

Figure 3.13: **'Fast' waveform activity from human dopaminergic neuron cultures recorded on commercial and custom MEAs. (A)** Three representative 'fast' waveforms recorded at 4, 5 and 6 WIV. Left traces show all the waveforms sorted from one active channel; 4 WIV = 8 spikes, 5 WIV = 9 spikes, 6 WIV = 6 spikes. The trace on the right is the average of all the waveforms. Arrow points to half-width (dashed line) of the average waveform at 4 WIV. **(B)** Average half-width of 'fast' waveforms showing little changes throughout the three weeks. Data are presented as the mean and standard error of the mean used for error bars.

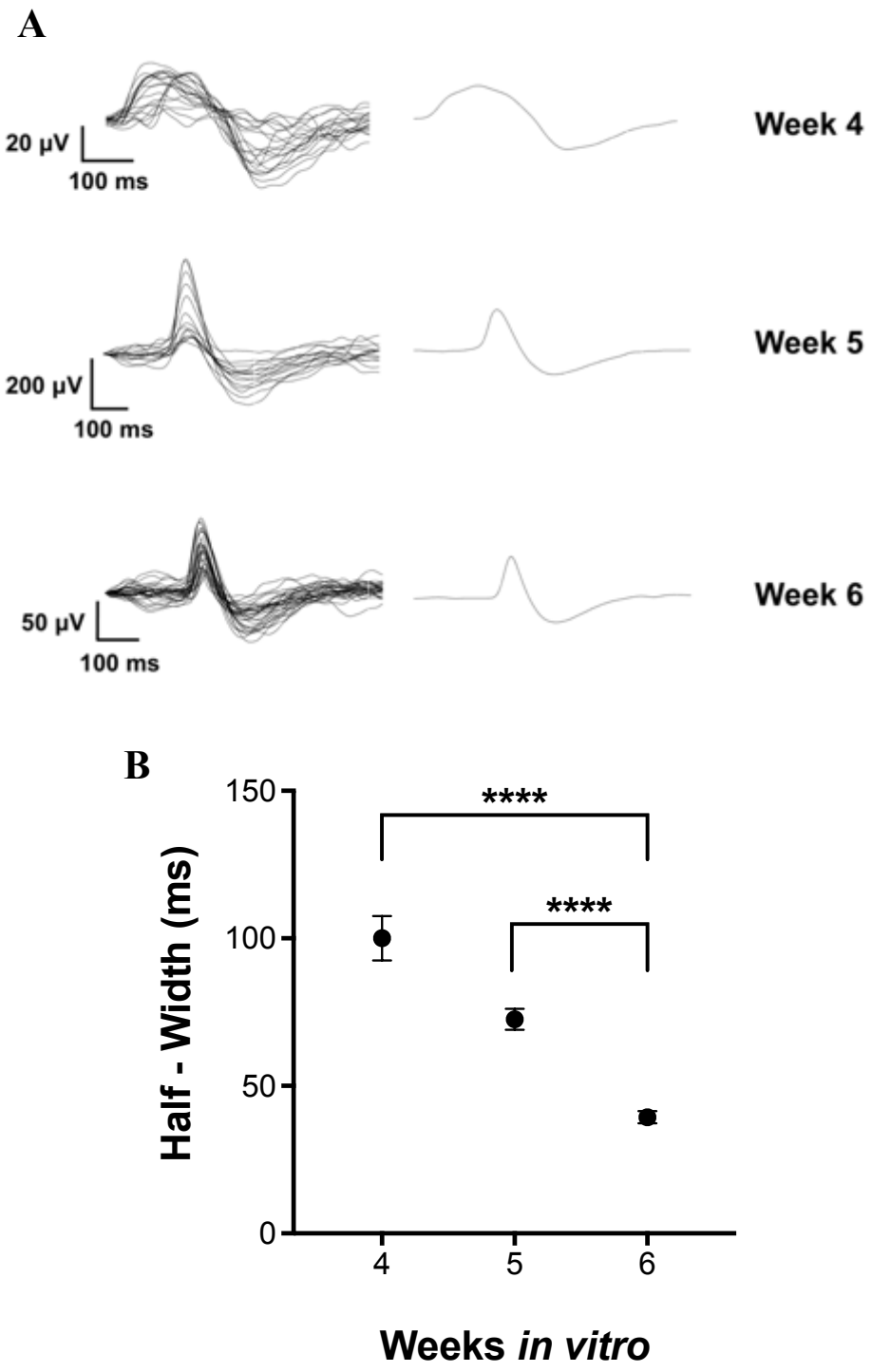

Figure 3.14: **'Slow' waveform activity from human dopaminergic neuron cultures recorded on commercial and custom MEAs. (A)** Three representative 'slow' waveforms recorded at 4, 5 and 6 WIV. Left traces show all the waveforms sorted from one active channel; 4 WIV = 20 spikes, 5 WIV = 15 spikes, 6 WIV = 31 spikes. The trace on the right is the average of all the waveforms. **(B)** Average half-width of 'slow' waveforms showing a reduction throughout the three weeks. Data are presented as the mean and standard error of the mean used for error bars. Asterisks indicate statistical significance, **** $p < 0.0001$.

3.4 Discussion

This chapter has focused on establishing the long-term culture and differentiation of human neural stem cells (hNSCs) into human cerebral cortical neurons (hCCNs) and human dopaminergic neurons. The aim was to develop an alternative *in vitro* model to study neurodegeneration, neuronal function and myelination without the use of animals. The ability to use human cells has been made available since the discovery of human embryonic stem cells (hESCs) in the late 1990s (Thomson *et al.*, 1998) and later on the discovery of the more ethical human induced pluripotent stem cells (iPSCs) (Takahashi and Yamanaka, 2006).

The availability of hiPSCs was ideal as it meant that I could potentially differentiate them into any type of neuron. A decision was made to differentiate into cerebral cortical neurons as they are present in the central nervous system (CNS) which is where demyelination occurs, causing diseases such as multiple sclerosis, and they possess exceptionally long axons, ranging between 10 to 20 mm (Mohan *et al.*, 2015). The protocol used for differentiating hNSCs to hCCNs was provided by the hNSCs supplier Axol Bioscience. Following their protocol, I was able to establish a long-term culture and differentiation of hNSCs, however, that was initially only possible on polystyrene wells and borosilicate coverslips. As I wanted to measure electrical activity of these cultures it was important to maintain these cultures long term on microelectrode arrays (MEAs).

Measuring the conduction velocity is one way to assess myelination *in vivo* (Steffens, Dibaj and Schomburg, 2012) and one way to do this *in vitro* it is ideal to separate the neuronal cell bodies and axons in different compartments in order to stimulate and record from them respectively. The microchannels fabricated that were previously discussed in Chapter 2 were tested using hNSCs and differentiating into hCCNs. These tests aided in developing a PDMS module with embedded microchannels that successfully restricted cell bodies in a separate compartment to axons. However, as the hCCNs were not electrically active within the time course of my studies, I was unable to test this aspect of their electrical activity. Other studies have used microchannels aligned across multiple electrodes to measure conduction velocity in rat dorsal root ganglion (DRG) cells co-cultured with Schwann cells (SCs) though rather low conduction velocities were observed (peaked at 0.59 m/s) (Sakai *et al.*, 2017).

hNSCs, were also differentiated into dopaminergic neurons and were compared to hCCNs electrically using voltage clamp and MEAs (both commercial and custom arrays). These methods allowed for following and validation of the electrical properties and functions when cultured over a period of up to 6 weeks.

3.4.1 Immunocytochemical Characterisation of Human Cerebral Cortical Neurons

The adult cortex consists of a six layered structured and each layer can be identified separately using the suitable layer specific markers (Livesey *et al.*, 2015). Tbr1 is an early cortical marker that is expressed by layer 6 cortical neurons (Shi *et al.*, 2012). Axol Bioscience, the supplier of the hNSCs and the protocol, state that their protocol produces a highly pure population of cortical neurons (>95%). This was confirmed from positive staining of Tbr1 from as early as week 1 post differentiation in over 95% of the cell culture. The cultures expressed Tbr1 throughout the 4-week period, with the population of hCCNs being over 99%. It cannot be definitely concluded that all the red stained cells are hCCNs as a negative control was not carried out and future experiments should include negative controls for immunofluorescence staining.

3.4.2 Culture of Human Neural Stem Cells on Different Surfaces

Initially hNSCs were cultured and proliferated on tissue cultured treated polystyrene well plates before they were differentiated in hCCNs. No issues with the cultures occurred and was able to maintain the differentiated cultures for at least 4 weeks. However, problems were encountered when culturing and differentiating the hNSCs on other surfaces such as those of the commercial and custom MEAs. One of the surfaces that was tested was that of the custom MEA fabricated by Epigem. The custom MEA (V1.0) was pre-coated with SureBond-XF but as soon as 24 hours after seeding the cells, they began to detach. This occurred as the surface was later found to not be what was asked but instead was SU-8, which is known to be bioincompatible when not chemically altered (Xue *et al.*, 2014).

A similar issue was observed when culturing hNSCs onto the commercial standard MEA (60MEA200/30iR-Ti) from Multichannel Systems (Reutlingen, Germany). The silicon nitride (Si_3N_4) surface was made hydrophilic prior to pre-coating with SureBond-XF but

cultures could not be maintained beyond 2 weeks. The cells began to detach from the surface from as early as 3 days *in vitro* (DIV) and by the time differentiation occurred (3 to 10 DIV) there were very few cells remaining.

Instead of using SureBond-XF I tried pre-coating the surfaces with laminin to see if that would improve cell adherence and growth on the commercial MEA. No improvement was found when using laminin and therefore I decided to revert back to using SureBond-XF as laminin also caused the cells to aggregate which did not improve the expansion process. Therefore, from that point onwards, SureBond-XF was used throughout the whole of my PhD for pre-coating surfaces when culturing and differentiating hNSCs.

3.4.3 Culture and Differentiation of Human Neural Stem Cells in Microchannels

It is well known that having a constricting barrier helps prevent the movement of cells into unwanted regions. Being able to manipulate the topology of the cells in culture is advantageous when compared to conventional dissociated neuronal cultures as this method offers a more *in vivo* type approach and also maintains something of a normal nervous system geometry (Yi *et al.*, 2015). For example, having microchannels between two compartments to separate neuron cell bodies from the axons allows axonal interactions with glial cells to be studied (Park *et al.*, 2012). Later studies using embryonic day 16 rat neurons and microchannels successfully allowed the study of axonal growth by applied localised biomolecular treatments although electrical recording was not incorporated into this system (Park *et al.*, 2014).

I designed a similar concept microfluidic device which consisted of two compartments separated by a 10 μm in width microchannel. Due to problems with the fabrication of the first microchannels, explained in Chapter 2, the width of microchannels varied and ranged between 10 to 20 μm. It was therefore found early on that when culturing and differentiating hNSCs in one compartment of the PDMS microchannels, the cell bodies were able to flow and adhere into the second compartment. The issue of the cell bodies entering the second compartment was resolved by using a quartz photomask for the fabrication process and also reducing the width of the microchannels to 5 μm. As expected, this resulted in the cell bodies to remain in the compartment they were seeded as they were unable to flow through the 5 μm constriction. Therefore, this meant that only

axons were able to pass through and grow into the second right-hand side compartment. I was thus able to attain excellent separation in a similar way to Park *et al.*, (2014) though using hCCNs.

3.4.4 Development of Ion Channels and Synaptic Inputs

Since voltage-gated ion channels play a crucial role in the generation and propagation of action potentials (Hodgkin and Huxley, 1952) as well as their distribution and density change with time (Lai and Jan, 2006) it was necessary to follow the changes in channel density in these human neuronal cultures against time. Furthermore, it was necessary to know the electrical state of the cultures in detail in order to validate the MEA derived electricals signals which are extracellular.

In hCCNs, Na_v currents were negligible at week 0, but increased week by week up to week 4 in parallel with axonal growth. In order to determine the true changes in current density it was important to correct for cell capacitance, which is an electrical measurement of cell surface area. This correction indicates that the Na_V current densities increased weekly despite changes in cell surface area. Implying as seen in the electrical traces that the cultured neurons became increasingly excitable.

The same analysis was carried out with human dopaminergic cultures which showed Na_V current densities that also increased weekly up to week 6 (no differences were observed between TH+ and TH- cells). As the channel densities in both cultures were remarkably similar and matched quite well the previously reports from hCCNs (Shi *et al.*, 2012) Na_v expression was unlikely to be the reason for the spontaneous excitability of the dopaminergic cultures versus the electrical silence of the hCCNs.

The reason for the difference was more likely to be due to the lack of synaptic inputs/synaptic maturity seen in the hCCNs electrically which was illustrated by the complete lack of the immunocytochemical presence of pre and postsynaptic markers synaptophysin and PSD-95. This was not the case for dopaminergic neurons as TH+ cells expressed synaptophysin and PSD-95 as well as had an abundance of postsynaptic potentials. However, hCCNs express these markers in long term cultures at 112 DIV and synaptic density was significantly increased by 300 DIV (Odawara *et al.*, 2016). This

indicates that hCCNs, require a much longer time period to mature and begin to form synapses when compared to human dopaminergic neurons.

3.4.5 Activity of Human Dopaminergic Cultures culture on MEAs

I was able to culture human dopaminergic neurons on commercial and custom MEAs even though I was unable to culture and expand hNSCs on them. This was achieved by differentiating hNSCs into human dopaminergic neurons on polystyrene wells and at 2 weeks they were detached and transferred onto commercial and custom MEAs were they remained in culture for up to 6 weeks.

It was previously found by Dr Matthew Euston (PhD student in Dr Brown's lab) that TH positive neurons (dopaminergic neurons) reached a steady level of approximately 25% of the whole culture at 4 to 6 weeks. This data was obtained from single cell patch-clamp electrophysiology experiments. Therefore, it was decided to electrically analyse these cultures during that time period using commercial and custom MEAs as a way to compare the two techniques and to validate the different forms of electrical activity seen in MEA recordings of these cultures.

As expected, the cultures were spontaneously active during the whole three-week period I studied, with the average percentage of active channels ranging between 47.9% to 73.1%. The active channels were analysed for spike-like behaviour and the resulting spikes sorted into two groups, 'fast' and 'slow', based on their waveform duration. Waveforms that were less than 3 ms in duration were classified as 'fast' and waveforms with a duration greater than 3 ms were classified as 'slow'. It was interestingly found that percentage of 'fast' and 'slow' spikes remained at about the same levels of approximately 30% 'fast and 70% 'slow' over the entire period studied (4 to 6 weeks). Analysing the half-widths of the 'fast' waveforms, indicated that the 'fast' activity recorded in the dopaminergic cultures remained unchanged as it was between 0.12 – 0.13 ms. It could be deduced that the 'fast' activity observed was from axonal action potentials whose neurons had reached maturation at or prior to week 4 *in vitro*.

Unlike the 'fast' waveforms which were unchanged by time in culture, 'slow' waveforms became narrower as the weeks *in vitro* progressed. At 4 WIV, the mean half-width was 100.0 ms and by 6 WIV the mean half-width was significantly reduced to 39.3 ms. It seems likely that such slow waveforms represent slow non-action potential related

potentials, such as synaptic and generator potentials. The narrowing of the 'slow' waveforms was most likely due to the maturation of these synapses in culture. This behaviour was also observed by Euston, (2017), who showed that by 6 WIV there was an increase in number and strength of synapses. It is also well known that synaptic development refinement and reconfiguration occurs in cultures (Goda and Davis, 2003). Synapse formation was confirmed by the co-localisation of the presynaptic marker synaptophysin with the postsynaptic marker PSD-95, which is an NMDA receptor-associated protein. Therefore, NMDA and AMPA receptors may be responsible for the spontaneous synaptic currents observed which were completely removed with the addition of antagonists of these receptors (Euston, 2017). This can also explain the reduction in half-width of the 'slow' waveforms as synaptic plasticity is critical during the development and maturation of neural networks (Shi *et al.*, 1999).

The results obtained from the commercial and custom MEAs allow an analysis of the whole human dopaminergic neuron culture that is able to report the entire network behaviour of the culture and could potentially be used to study development and pharmacology of this system. This provides a broader understanding of how the culture develops electrically which can be a great tool in studying cellular functions in more detail in real-time.

3.5 Conclusions

Human cerebral cortical neurons (hCCNs) and human dopaminergic neurons were successfully differentiated from human induced pluripotent stem cells (hiPSCs). Their development was followed electrically (voltage-clamp and MEAs) and immunocytochemically. Both were found to have voltage-gated sodium channels, but only human dopaminergic neurons formed synapses during the period of culture. Issues with differentiating and culture of hCCNs on MEAs meant that it was not possible to record from them *in vitro.* However, differentiated dopaminergic neurons were successfully cultured on custom MEAs (V3.2 and V3.4) and was able to record from them which means that the fabricated MEAs were functional and biocompatible.

Chapter 4

Development of Electrical Behaviour in Mouse Spinal Cord Cultures

Abstract

The much greater availability of microelectrode arrays (MEAs) allows the development of more informative *in vitro* models to study various neurological diseases. MEAs potentially provide the ability to monitor over the long term the trajectory of electrical development and its alteration in pathology. Mouse spinal cord cultures have been used for decades as a model to study the process of myelination in the central nervous system (CNS). In the present study, I have cultured mouse spinal cord cells on commercial and custom MEAs from 2 to 52 days *in vitro* (DIV) to follow their electrical development. Recordings were carried out using a custom 16 channel recording device and various configurations of MEAs that allowed for the simultaneous recording from 16 channels. The cultures were found to be electrically active from as early as 2 DIV and remained so up until 52 DIV. I identified several distinct patterns of electrical activity that altered over time in culture. Spike waveforms were different pre- and post-myelination and the conduction time between electrodes enabled me to assess changes in nominal conduction velocity (NCV) which increased from 0.03 m/s at 2 DIV to 15.00 m/s at 24 DIV. The NCV changes were consistent with the ongoing process of *in vitro* myelination. Successful growth was achieved on custom MEAs and preliminary recordings were obtained, indicating improvements that could be made in the electrode configuration to better capture NCV. The approach shows the use of MEAs in conjunction with pre-existing techniques can provide a much deeper understanding of the process of myelination and could be applied to the study of demyelinating diseases such as multiple sclerosis.

4.1 Introduction

Studying the central nervous system (CNS) provides important information on understanding how it altered by neurodegenerative diseases such as multiple sclerosis (MS). These diseases are usually studied at the cellular level using mouse and rat models such as experimental allergic encephalopathy (EAE), which was introduced in the 1930s, to improve our understanding of multiple sclerosis (Rivers and Schwentker, 1935). This model requires a large number of animals for it to be of sufficient power, for example, it is estimated that 3 cohorts each of 12 animals are necessary to test the efficacy of a single drug (Bijland *et al.*, 2019), which is why alternative or supplemental methods for following development *in vitro* are useful.

The introduction of microelectrode arrays (MEAs) (Thomas *et al.*, 1972) and their development since, allow the electrical behaviour of cultures to be followed across time and offer a highly data-rich temporally valid technique to investigate the CNS *in vitro* in long term cultures (Odawara *et al.*, 2016). MEAs may have tens to hundreds planar electrodes that simultaneously provide recordings from the culture (commercially available by Multichannel Systems). Also, as repeated measures can be made non-destructively from cultures, the use of MEAs as *in vitro* models is more advantageous when compared to some other techniques as it helps reduce the costs by requiring less animals, can be easily manipulated pharmacologically and allows for cell networks to be kept alive for extended periods of time so that long-term changes can be followed. The ability to produce customised MEAs adds a further benefit to optimise the electrode positioning to meet the specific requirements of the investigation.

In this chapter, I developed and applied MEA technology to provide insight into the electrical development of mouse spinal cord cultures. Mouse spinal cord cultures were grown on commercial MEAs to study their differentiation and maturation by recording their electrical activity. The electrical activity recorded was used to interrogate the progress of synaptic formation, cell connectivity and myelination *in vitro*. The results add a finer grained insight into the influence of myelination on neuronal signalling and was comparable to data obtained from other techniques that demonstrate of the presence of myelin using immunocytochemistry (myelin basic protein) and electron microscopy (Thomson *et al.*, 2006). I was able to fabricate and test custom MEAs as well as incorporate microchannels in order to improve the study of *in vitro* myelination. In the

time available however, it was unable to grow cells through the microchannels and therefore I was unable to make any NCV measurements with this method. Parts of this work were published (Bijland *et al.*, 2019).

4.2 Methods

4.2.1 Mice

A total of 5 pregnant mice were used for all experiments in this chapter. The mice were bred and maintained in the Biological Services Facilities at the University of Glasgow. Embryonic day 13 (E13) mice were obtained by mating wild type mice $Cnp^{+/+}$ with $Cnp^{-/-}$ mice (Lappe-Siefke *et al.*, 2003), both on a C57BL/6J (Charles River) background. Pregnant mice were killed on the morning of E13 by either Dr. Julia Edgar or Dr. Matthew Euston who also carried out the dissections. The embryos were removed from the uterine horns and immediately placed on ice in a sterile 10 cm petri dish.

All mouse use was approved by the Ethical Committee of the University of Glasgow and licensed under the Animal [Scientific Procedures] Act 1986 project licence PPL60/3656.

4.2.2 Mouse Myelinating Cell Cultures

The number of embryos obtained varied between the 5 pregnant mice used. The spinal cords of E13 mice were dissected and incubated in 1 ml per 6 cords of 0.25% trypsin in HBSS minus calcium and magnesium for 15 minutes at 37°C. The digestion was then stopped by adding 1 ml per 6 cords of plating medium (50% DMEM, 25% HBSS and 25% horse serum) plus 0.04 mg/ml DNase. The cells were then gently triturated before they were centrifuged at 800 rpm for 5 minutes. Following centrifugation, the cells were resuspended in plating medium and plated at approximately 150,000 cells per cm^2 on commercial and custom MEAs. The MEAs were previously plasma treated and coated with Poly-L-lysine (PLL; Sigma). After about 1 hour of incubation at 37°C, the media in the MEAs was topped up to half the final volume with pre-warmed plating media. Then, at the end of the day, the other half of the volume was added using pre-warmed differentiation media and the cells were incubated at 37°C in 5% CO_2. The differentiation medium was prepared with the following: DMEM supplemented with 30% D-glucose, 10 μg/ml biotin, 50 μM hydrocortisone, 10 μg/ml insulin and 0.5% hormone mix (stock concentration 1 mg/ml apo-transferrin, 20 mM putrescine, 4 μM progesterone, and 6 μM selenium). Half media changes were carried out using serum free differentiation media three times a week up until 12 days *in vitro* (DIV). From 12 DIV onwards, half media changes were carried out three times a week using insulin free differentiation media.

For the experiments in this chapter, cells were plated on the MEAs at either 0 DIV or 14 DIV.

4.2.3 Recording from Commercial MEAs

The mouse spinal cord cultures were maintained on commercial MEAs (60MEA200/30iR-Ti-gr; Multi Channel Systems, Reutlingen, Germany) from 2 to 52 DIV over four separate sets of experiments. A fluorinated ethylene-propylene (FEP) membrane (ALA MEA-MEM-SHEET) was placed over the ring of the MEA and secured in place using an O – ring. This allowed for the cultures to remain sterile when using the MEAs outside of the tissue culture hood. The MEAs were periodically (three to four times a week) transferred from the incubator to the electrophysiology laboratory from the tissue culture room where the recordings were carried out. Out of all the MEA cultures used none were contaminated and were kept in cultures at different time periods ranging between 2 to 52 DIV.

The membrane sealed MEA was then placed into a lab built custom recording device (RD2) and left for 5 minutes in order for the temperature to reach 37°C before beginning recordings. The temperature was controlled and maintained at 37°C using a Peltier device that was attached under the RD2 using thermal paste. The recordings were done in differentiation medium (media was not changed prior to recording). A one-minute gap-free protocol was set up on Clampex 10 software for Windows (Molecular Devices Corporation, California, USA). The signals were pre-amplified by a x10 pre-amplifier headstage (Omnetics, Minnesota, USA) and amplified by an A-M Systems Model 3600 amplifier (Washington, USA). Signals were digitally filtered at 3 Hz high pass filter, 1 kHz low pass filter and amplified up to x20,000. A digital notch filter was used to remove 50 or 60 Hz noise during recording. All recordings were differential AC coupled with the reference to ground. After acquiring two recordings from one side of the MEA, it was rotated, and recordings were made from the other 3 sides of the MEA. Representative images of each side were also taken using a Retiga R1 camera (Teledyne QImaging, Surrey, Canada) and Micro-Manager Open Source Microscopy Software. Once done, the MEAs were placed back into the incubator for future use. The MEAs were carefully transported to avoid disturbances and were kept at 37°C while on the RD2 for most of the time when outside of the incubator (between 20 to 25 minutes). Once the recordings were

obtained the MEAs were placed back into the incubator at 37°C in 5% CO_2. This process was repeated for all commercial MEA recordings carried out 3 or 4 times a week.

For the pharmacology experiments, neural activity modulators were added directly into MEA chamber after removing the FEP membrane (see section 4.2.8 for what compounds were used). A three-minute gap-free protocol was set up on Clampex 10 software and amplifier settings were as mentioned above.

4.2.4 Preparing and Recording from Custom MEAs

Before culturing cells on the custom MEAs, a PDMS module containing a single well or with two wells separated by microchannels (fabrication process explained in Chapter 2) had to be aligned with the electrodes. The custom MEAs together with the PDMS modules were plasma coated to ensure better bonding of the PDMS onto the surface of the MEA. The microchannels were aligned over the electrodes by hand using a compound microscope. For the single well PDMS module, the mouse cultures were seeded in the same way as when seeding a well of a multi-well culture plate. When using the PDMS containing microchannels, cells were seeded in one of the compartments whilst the second compartment only contained media. To ensure the flow from one compartment to the other, the volume in the cell seeded side was higher (300 µl) than that of the second compartment (100 µl). An FEP membrane was also placed over the PDMS module before transporting the custom MEAs for recording. The custom MEAs were placed into different custom recording device (RD3) from the commercial MEAs and the same recording protocol, as detailed in section 4.2.3, was used.

4.2.5 Single Cell Recordings

Whole-cell current clamp recordings were performed using an Axopatch 200B amplifier with a Digidata 1440A digital acquisition system and Clampex 10 software for Windows (Molecular Devices Corporation, California, USA). Experiments were performed using an extracellular solution containing identical ionic concentrations to the cell culture media (mM): 110.3 NaCl, 5.3 KCl, 1.8 CaCl2, 0.8 MgCl2, 10 HEPES, 25 glucose, pH 7.4. The pipette intracellular solution contained (mM): 135 K-gluconate, 2 MgCl2, 2 Na- ATP, 0.5 Na-GTP, 10 HEPES, 0.5 EGTA, pH 7.2. Microelectrodes were pulled from borosilicate glass using a Flaming/Brown P-87 micropipette puller. The microelectrodes were pulled

to a resistance ranging between 3 to 8 MΩ. Neural activity modulators were added directly to the bath (see section 4.2.8 for compounds used).

4.2.6 Analysis of Recordings

All data acquired was analysed offline using Clampfit 10 and 11.1 software for Windows (Molecular Devices Corporation, California, USA) and Excel 2019 (Microsoft, Washington, USA).

Each data file consisted of 16 traces, representing a single recording from 16 separate electrodes. As each MEA had four sides, 59 recordings were made from 59 different electrodes for each MEA. Before further analysis, all traces were filtered using a lowpass Boxcar filter with smoothing points set to 15. An initial superficial manual reading of the traces indicated two distinct waveforms that were classified as 'fast' and 'slow'. To separate the 'fast' from the 'slow' waveforms, an automated threshold search tool was used.

For 'fast' waveforms, the baseline was set to 0 and the trigger marker was set below the peaks of the spikes. For example, if the trigger marker was set to 50μV, any spike above that was selected. The pre- and post-trigger lengths were both set at 1 ms (millisecond). In the event rejection section, the minimum allowed duration was set at 0.1 ms and the maximum allowed duration at 3 ms, for the 'fast' waveforms. With these values set, the threshold search was run, and all events detected were then saved. Any anomalous events due to artefacts were manually rejected. The half-width and interevent interval data produced from this search were copied into Excel for further analysis. This was repeated for all other traces analysed.

For 'slow' waveforms (duration greater than 3 ms), a similar template search was carried out. Firstly, a representative spike was selected to create a template. That template was then used in the template search to scan the trace and select all spikes resembling it. All the spikes collected for that trace were then saved for further analysis. A new template had to be created for each trace analysed due to variations in amplitudes and form. Any anomalous events due to artefacts were manually rejected. The half-width and interevent interval data produced from this search were copied into Excel for further analysis. This was repeated for all other traces analysed. For all the individual waveform detected at

each DIV, they were then averaged to produce one waveform representative of the day *in vitro*.

Once separated into 'fast' and 'slow' spikes, the spike frequency of all active channels was calculated. Frequency was calculated by dividing the total number of spikes by 60 (length of recordings was 60 seconds) for each active channel.

4.2.7 Immunocytochemistry

The immunocytochemistry for all the mouse cultures shown in this chapter were carried out by Dr. Julia Edgars lab and we published the results in Bijland et al., 2019. The primary antibodies used were: mouse anti-CNP (SMI191; 1:1000; Cambridge Bioscience, Cambridge, UK), rabbit anti-Caspr (1:1000; kindly provided by Professor E. Peles), rabbit anti-ionized calcium binding adapter molecule 1 (Iba1; 019-19741; 1:800, Wako, Neuss, Germany), rabbit anti-PLP226 antiserum (N.P. Groome, Oxford Brookes University, Oxford, UK). Bound antibodies were visualised using appropriate combinations of species/isotype-specific fluorochrome-conjugated secondary antibodies which were: 488 goat-anti mouse IgG1 (A2112), 488 goat-anti rabbit IgG (A11008), 568 goat anti-rabbit IgG (A11036). All Alexa Fluor, Life Technologies. Nuclei were stained with DAPI (2 μg/ml).

4.2.8 Drugs and Compounds

All drugs used were diluted from concentrated stock and pipetted directly to the MEA. The drugs used were: tetrodotoxin (TTX; 1 μM; Tocris, 1069), cyanquixaline (CNQX; 5 μM; Tocris, 1090), picrotoxin (100 μM, Sigma- Aldrich, P1675).

4.2.9 Graphs and Statistics

All graphs and statistical analysis were carried out in Prism 8 (GraphPad Software, San Diego, USA). Data were tested for normality in order to choose appropriate statistical tests. The D'Agostino-Pearson and the Shapiro-Wilk normality tests were used. For parametric and multiple independent samples, a one-way ANOVA was performed. A Kolmogorov-Smirnov test was used for two sample data that were non-parametric. When data were parametric and had two samples an unpaired t-test was used. For non-

parametric and multiple independent samples, the Kruskal-Wallis test with a Dunn's multiple comparisons test was performed. Statistical significance was accepted at probabilities of equal to or less than 0.05. A p-value of less than 0.05 is shown as a single asterisk (*). Data are presented as the mean ± standard deviation or the standard error of the mean (SEM) for the error bars.

4.3 Results

4.3.1 Immunocytochemical and Morphological Characterisation of Mouse Spinal Cord Cultures

4.3.1.1 Immunocytochemical Characterisation

To better follow the process of myelination in culture, immunocytochemistry and fluorescence microscopy was carried out on representative cultures at different time points. The fluorescent images shown in **Figure 4.1** were obtained from a recent paper to which I contributed (Bijland *et al.*, 2019). Embryonic day 13 mouse spinal cord cultures are comprised of several cell types and structures such as axons, oligodendrocytes, astrocytes and microglia. These were observed throughout the culture progresses from 6 to 28 DIV and indicates its cellular complexity (**Figure 4.1A-E**).

The morphology of 2' , 3' -cyclic nucleotide 3'-phosphodiesterase (CNP) positive cells can be seen to change from 6 DIV to 28 DIV (**Figure 4.1A)**. CNP is expressed early in the oligodendroglial lineage and is present in non-compact myelin (Trapp et al, 1988). Single myelin-like sheaths were observed at 12 DIV when compared to 6 DIV where the cells have a 'lacy' appearance. The myelin sheaths were more distinct at 21 DIV with fewer 'lacy' appearing cells and by 28 DIV a denser network of myelin sheaths was observed.

Microglia were identified by to ionised calcium binding adaptor molecule 1 (IBA1) staining and were notably visible from 7 DIV. They begin to form multiple processes throughout the culture period up to 28 DIV (**Figure 4.1B)**.

Mouse spinal cord cultures also contained neuronal cells revealed by NeuN staining (neuronal nuclei; NeuN), astrocytes (glial fibrillary acidic protein; GFAP) and oligodendrocyte progenitor cells (OPCs) (neural/glial antigen 2; NG2) (**Figures 4.1C-E**)

Co-staining of proteolipid protein (PLP/DM20), Caspr and phosphorylated neurofilament (NF), shows that by 28 DIV the axons were myelinated, and the internodes were separated by nodes of Ranvier (**Figure 4.1F)**. PLP and DM20 are proteins present in myelin and

therefore a myelin marker. Caspr is a protein present in the paranodal regions of the nodes of Ranvier and NF is an axonal maker.

4.3.1.2 Culture on Commercial MEAs

Mouse spinal cord cells were successfully cultured on commercial MEAs (**Figure 4.2).** They adhered well onto the surface and remained healthy for several weeks in culture up to a total of 52 days. The morphology of the cultures on commercial MEAs was similar to those seen on multi-well polystyrene plates (**Figures 4.2B-E)**.

The cell bodies at 2 DIV (**Figure 4.2B**) were all of similar shape, whereas from 8 DIV (**Figure 4.2C**) there were different cell body morphologies observed in the culture (white arrows). The number of processes present also increased with time in culture, which could be clearly seen when comparing 21 DIV (**Figure 4.2E**) with the commercial MEA cultures of previous days.

The cells were able to differentiate and proliferate on the MEAs which could be seen by the increase in cell density as the days in culture increased. After about 28 DIV, some cell death was observed as cells began to detach (**Figure 4.2F**). However, the cells that remained, adhered to the MEA surface up until day 52 when the experiments were concluded.

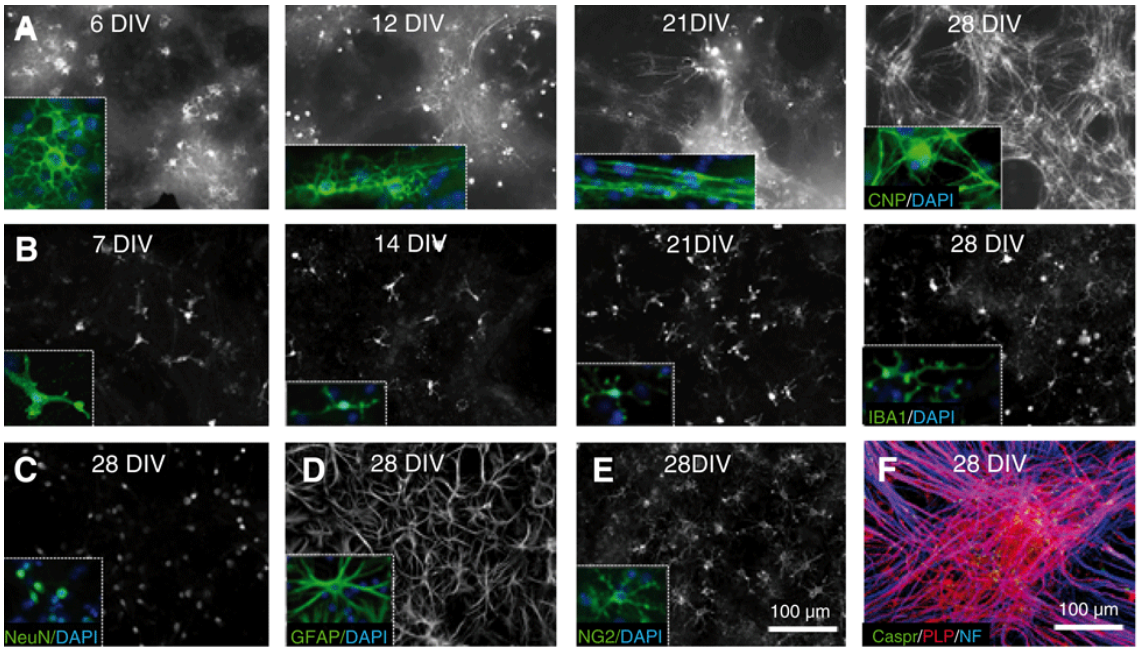

Figure 4.1: Embryonic day 13 mouse spinal cord cells differentiate over time into the major neural cell types of the nervous system. (A) The morphology of CNP positive cells changes with time in culture. At 6 DIV, multiple cell process' extend from the cell body and the cells have a 'lacy' appearance, as shown in the inset. By 21 DIV, many cells have extended multiple myelin-like sheaths and by 28 DIV few 'lacy' appearing cells are left and a dense network of myelin sheaths was visible. **(B)** Iba1 +ve microglia are present at all stages examined. At 7DIV most microglia appear amoeboid but branch out and extend multiple processes over time. **(C)** Antibody to NeuN labels neuronal nuclei and sometimes staining extends into the cytoplasm, but rarely enters the cell processes. **(D)** GFAP positive astrocytes are found throughout the culture, (**E**) as are NG2 +ve oligodendrocyte progenitor cells (OPCs). **(F)** Combined staining with antibodies to PLP/DM20, Caspr and phosphorylated neurofilament (NF), revealed that many axons are covered by consecutive sheaths with nodes of Ranvier straddled by Caspr positive paranodes. (Figure from Bijland *et al.*, 2019).

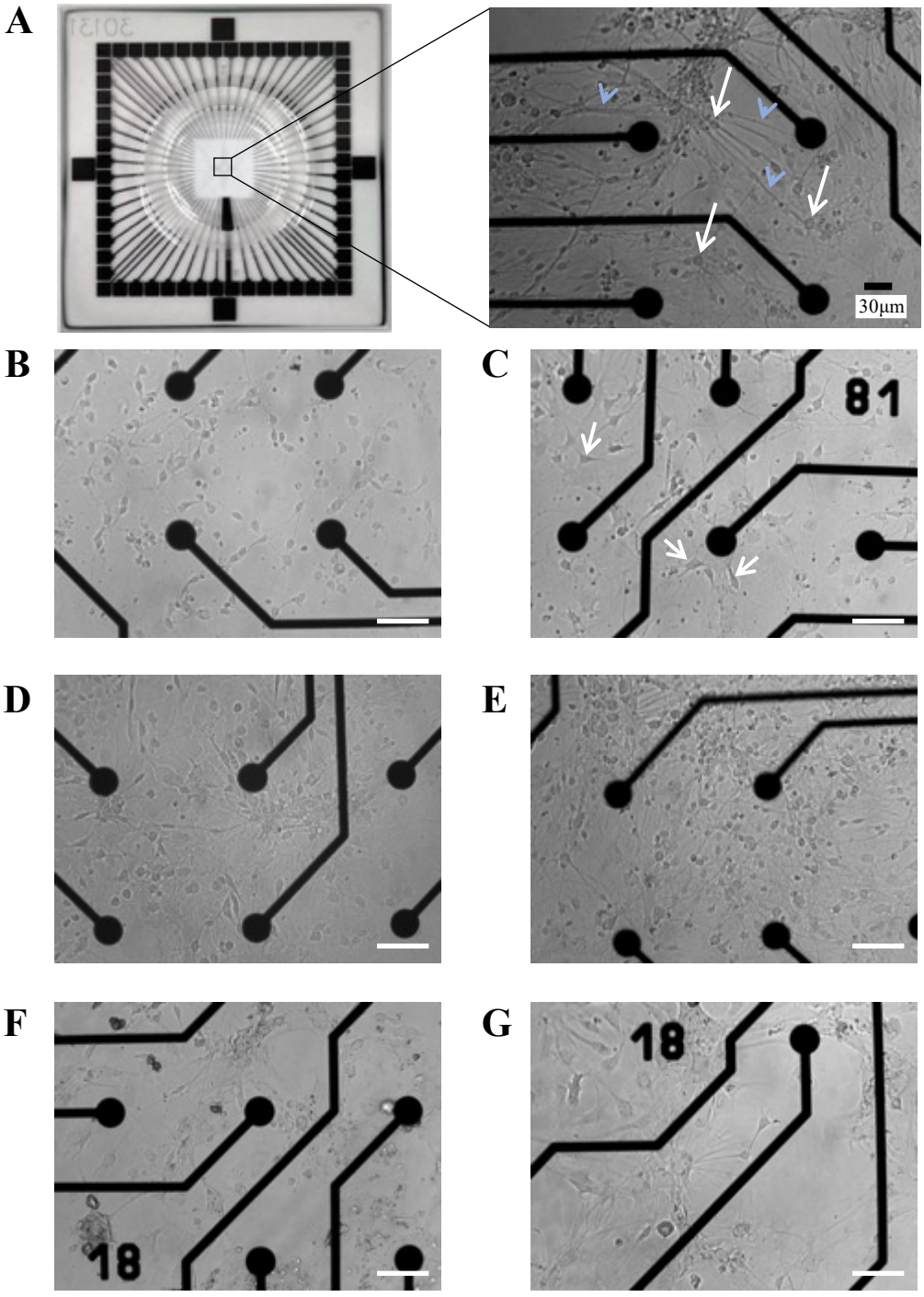

Figure 4.2: Mouse spinal cord cultures on commercial MEAs. (A) Low power view of commercial microelectrode array (MEA) on the left. In the high-power image (right), four electrodes (black circles) can be observed in relation to the cell bodies (white arrows) and processes (including axons; blue arrowheads) of neurons and glia, on an MEA at 22 DIV. Representative images at **(B)** 2 DIV, **(C)** 8 DIV (different cell body morphologies shown by white arrows), **(D)** 14 DIV, **(E)** 21 DIV, **(F)** 29 DIV, **(G)** 44 DIV. Scale bar = 50µm.

4.3.2 Electrical Activity of Mouse Myelinating Cultures

Most data available focuses on mouse spinal cord cultures once myelination begins and up until it concludes. Therefore, I chose to study the activity of the cultures from as early as 2 days *in vitro* (DIV) up to 52 DIV. It was found that from as early as 2 DIV the mouse spinal cord cultures were electrically active. Different types of spike waveform activity were observed at different stages and two examples of active traces at 4 weeks *in vitro* (WIV) indicate this (**Figure 4.3B**). The cultures were found to be electrically active throughout the whole experimental period with a decrease observed only after 7 WIV.

The average number of active channels throughout an eight-week period was measured and it was found that there were approximately between 9 and 33 active channels from a total of 59 channels during the experimental procedure. Between 1 and 7 WIV the number of active channels ranged between 21 and 33 (**Figure 4.3C**).

To analyse the data for statistical significance a one-way ANOVA was performed as the data were found to be normally distributed. There was no statistical difference between the spontaneous activity measured at 1 WIV ($n = 5$) when compared to all the other weeks *in vitro* ($p > 0.05$). However, there was a significant increase in spontaneous activity between 2 WIV ($n = 16$) and 4 WIV ($n = 13$) ($p = 0.0160$). A statistically significant increase in activity was also observed between 3 ($n = 10$) and 4 WIV ($p = 0.0413$). From 4 WIV onwards a decrease in spontaneous activity was observed but it was not statistically significant when compared to 5 ($n = 9$), 6 ($n = 8$) and 7 ($n = 8$) WIV ($p > 0.05$). However, the decrease in activity observed from 4 WIV to 8 WIV ($n = 4$) was statistically significant ($p = 0.0052$). The decrease in active from 5 WIV to 8 WIV was also statistically significant ($p = 0.0333$).

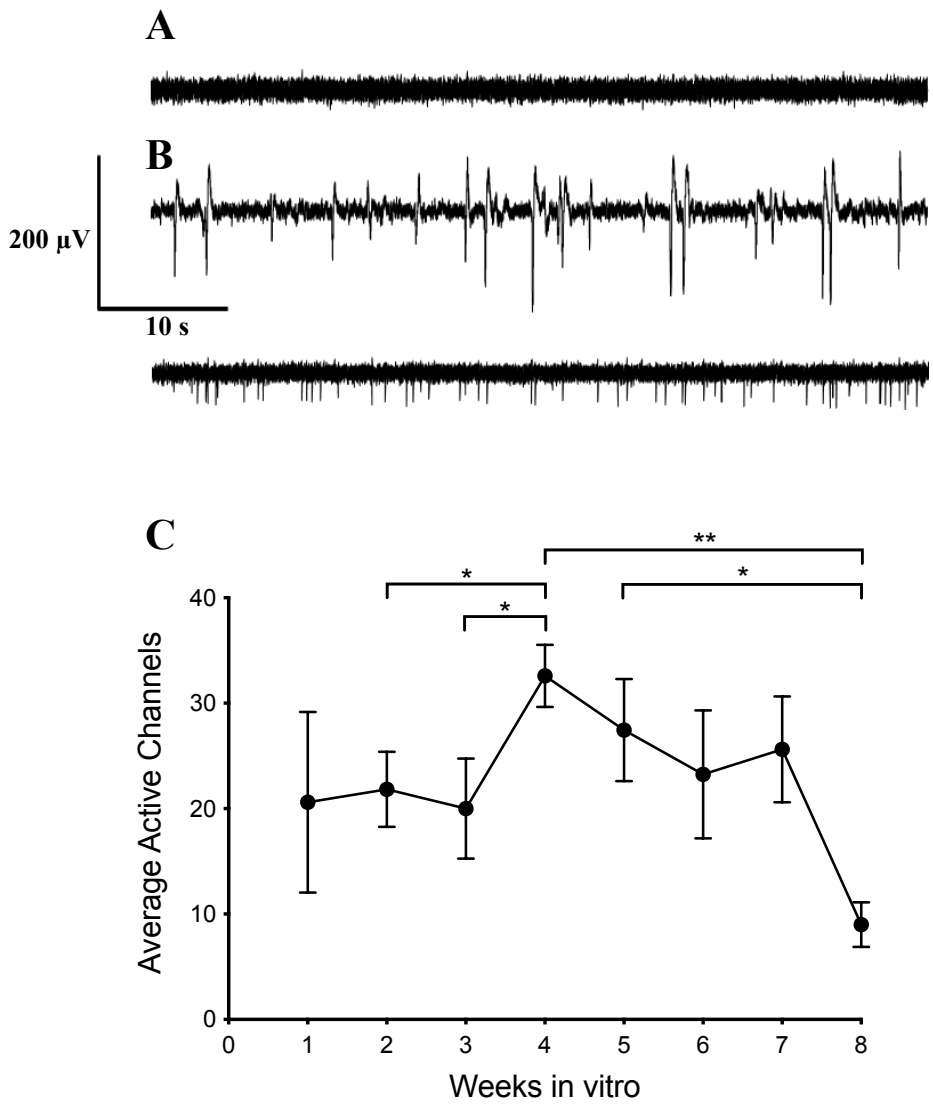

Figure 4.3: Average number of electrically active channels throughout an eight-week period of culture on commercial MEAs. Representative examples of **(A)** a non-active and **(B)** two active channels from 4 weeks *in vitro*. **(C)** All the data obtained from a total of eleven MEAs and averaged to show the varying electrical activity of mouse spinal cord cultures as they differentiate and mature. The n values for each week were as follows: week 1 = 5; week 2 = 16; week 3 = 10; week 4 = 13; week 5 = 9; week 6 = 8; week 7 = 8; week 8 = 4. Data are presented as the mean and standard error of the mean used for error bars; asterisks indicate statistical significance, * $p < 0.05$, ** $p < 0.01$.

4.3.3 Pharmacological Assessment of Mouse Spinal Cord Cultures

To establish if the electrical activity was due to synaptogenesis, electrical recordings were taken daily between 20 and 24 DIV. The results show that at least two types of waveforms were observed, 'fast' and 'slow', as well as burst like activity (**Figure 4.4A)**. Additive pharmacology at 24 DIV demonstrated distinct *in vivo* network-like activity of spinal cord myelinating cultures (**Figure 4.4B**). The addition of 100 μM of picrotoxin, a GABAergic inhibitor, evoked a large increase in 'fast' spikes when compared to the control trace. The subsequent addition of 5 μM of tetrodotoxin (TTX), a voltage-gated sodium channel blocker, inhibited the fast spike-like activity as fewer spikes are present in the third trace versus the second one. Finally, 5 μM of cyanquixaline (CNQX), a blocker of the AMPA/kinate receptors, was added to the MEA bath which in turn further blocked nearly all spontaneous activity previously present.

To complement the data obtained from the MEA recordings, single cell patch recordings were also carried out. Spontaneous electrical activity was observed in 68 out of 75 cells tested with an average spiking frequency being 2.13 ± 0.32 Hz (mean ± SEM). The activity was also enhanced with the addition of 100 μM of picrotoxin and completely blocked by 1 μM of TTX (**Figure 4.4C**).

Comparing both techniques, it was deduced that mouse spinal cord myelinating cell cultures were spontaneously active, and the activity can be manipulated using pharmacology.

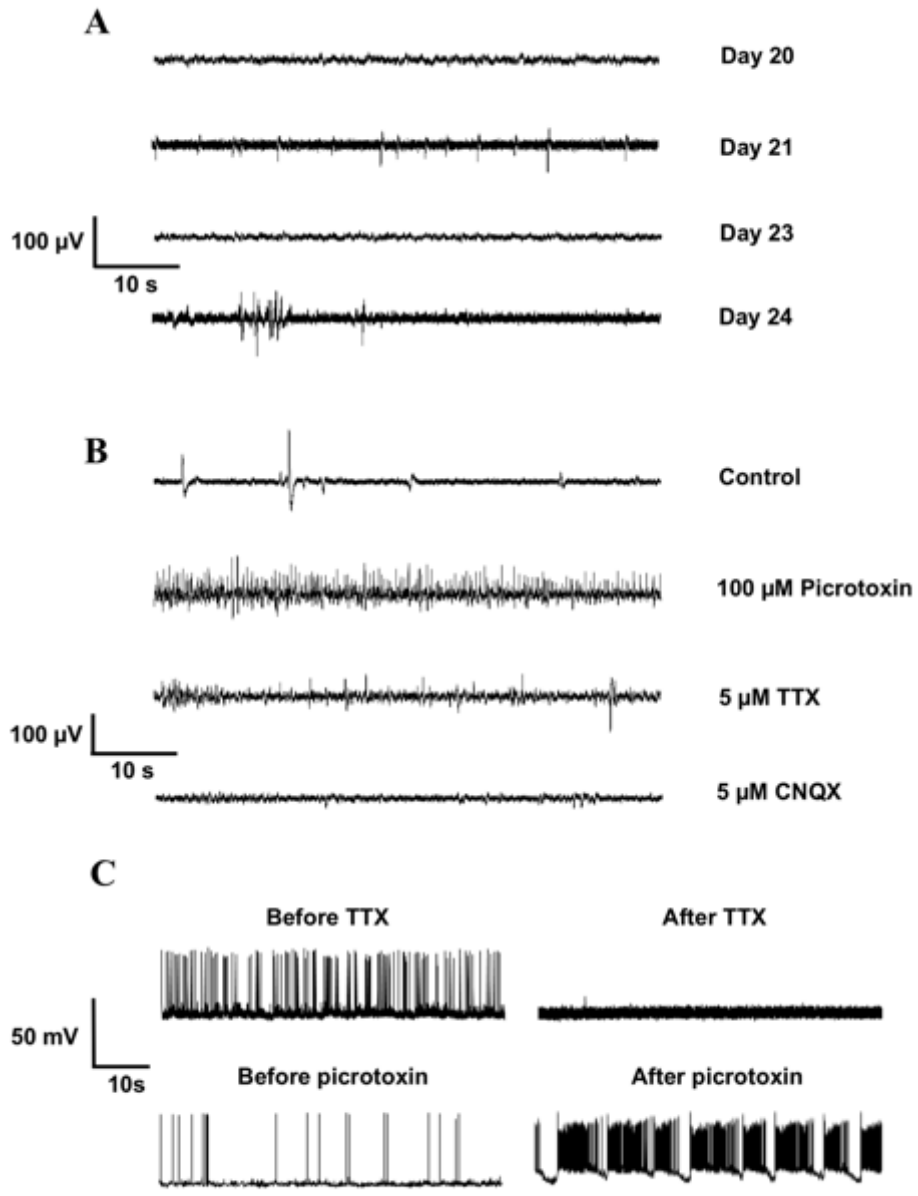

Figure 4.4: Myelinating cell cultures are spontaneously excitable. (**A)** Representative extracellular recordings from a single electrode between 20 and 24 DIV. (**B)** Additive pharmacology on a 24 DIV culture (sequential administration of drugs without washout) demonstrated *in vivo*-like neuronal network activity of spinal cord myelinating cultures. The traces show that addition of picrotoxin evokes a massive increase in 'fast' neuronal activity. Subsequent addition of TTX, inhibits most of the 'fast' spike-like activity. CNQX furthers blocks neuronal activity. (**C)** Examples of whole-cell current clamp recordings from single cells, presumably neurons, firing spontaneously at a resting potential of around -50 mV. Top, traces before and 5 minutes after the addition of 100 µM picrotoxin. Bottom, traces from a second cell before and 5 minutes after the addition of 1 µM TTX. TTX consistently blocked activity (n = 6 cells) whilst picrotoxin caused regular burst spiking in every cell tested (n = 18 cells). (Figure adapted from Bijland *et al.,* 2019).

4.3.4 Changes in of Electrical Activity with Time in Culture

The waveforms were found to vary in duration across time. To better investigate these changes, 10,688 traces obtained from all commercial MEAs were analysed for alterations using waveform discrimination. 'Fast' waveforms were of less than 3 ms in duration and broadened with time in culture (**Figure 4.5**) 'Slow' waveforms were of greater than 3ms in duration and narrowed with time in culture (**Figure 4.6**).

The number of 'fast' waveforms detected from one representative channel at 10, 27 and 44 DIV are shown in **Figure 4.5A** (left), with the average spike waveform on the right. Without further analysis it was clear that the 'fast' waveforms varied at different days. This could be quantified by analysing the changes in half-widths of the spikes from representative channels (**Figure 4.5B)**. The half-widths measured at 10 DIV were 0.31 ± 0.04 (1082 spikes), at 27 DIV was 0.81 ± 0.09 (342 spikes) and at 44 DIV was 0.76 ± 0.06 (30 spikes). The half-width is indicated by the double headed arrow at 10 DIV (**Figure 4.5B**). The representative half-width at 10 DIV (0.27 ± 0.02 ms; 64 spikes) was approximately three times less than that at 27 DIV (0.77 ± 0.06 ms; 238 spikes) and 44 DIV (0.76 ± 0.06 ms; 30 spikes). The decrease in half-width at 27 and 44 DIV when compared to that at 10 DIV was highly statistically significant ($p < 0.0001$; unpaired t-test as the data were normally distributed). The half-widths at 27 DIV and 44 DIV were about the same and were not significantly different ($p = 1.08$). The mean half-width duration of all 'fast' spikes was 0.59 ± 0.35 ms (mean ± standard deviation), measured from a total of 12,638 'fast' spikes.

The number of 'slow' spikes detected from one representative channel at 10, 27 and 44 DIV are shown in **Figure 4.6A** (left), with the average spike waveform on the right. The half-widths measured at 10 DIV was 50.6 ± 8.6 (47 spikes), at 27 DIV was 34.1 ± 6.8 (194 spikes) and at 44 DIV was 26.8 ± 8.1 (152 spikes). Unlike with 'fast' spikes, the half-width (indicated by double headed arrow at 44 DIV) narrowed with time (**Figure 4.6B**). The representative half-width at 44 DIV (24.86 ± 5.30 ms; 12 spikes) was about two times greater than that at 10 DIV (48.52 ± 4.62; 12 spikes). This difference in half-width between 44 DIV and 10 DIV was highly statistically significant ($p < 0.0001$; unpaired t-test as the data were normally distributed). The half-width being lower at 27 DIV (33.32 ± 4.76 ms; 8 spikes) when compared to 10 DIV was also highly significantly

different as $p < 0.0001$ (unpaired t-test). The half-width was lower at 44 DIV than that at 27 DIV and this difference was to be significantly difference as $p = 0.0019$ (unpaired t-test). The mean half-width duration of all 'slow' waveforms was 40.89 ± 17.71 ms (mean ± standard deviation), measured from a total of 12,524 'slow' waveforms.

The number of active channels of which 'fast' waveforms were present increased after 1 WIV (0.3%; from 295 channels) up until 4 WIV (9.5%; from 708 channels). The percentage of active channels with 'fast' waveforms was 4% at 2 WIV (from 1062 channels) and 7.2% at 3 WIV (from 531 channels). From week 5 to week 7 (1475 channels) only four active channels presented activity consisting of 'fast' waveforms, with zero at week 8 (236 channels) (**Figure 4.7**).

The number of active channels of which consisted of 'slow' waveforms ranged between 30.5% at 3 WIV (from 531 channels) to 46.3% at 5 WIV (from 531 channels). There was an increase in 'slow' waveform activity from 4 weeks and onwards when compared to the first 3 weeks. The least amount of 'slow' waveform activity was recorded at 8 WIV (15.3%; from 236 channels) (**Figure 4.7**). A total of eleven commercial MEAs were used at different time periods throughout the eight-weeks of this investigation. One channel represents one electrode of a commercial MEA.

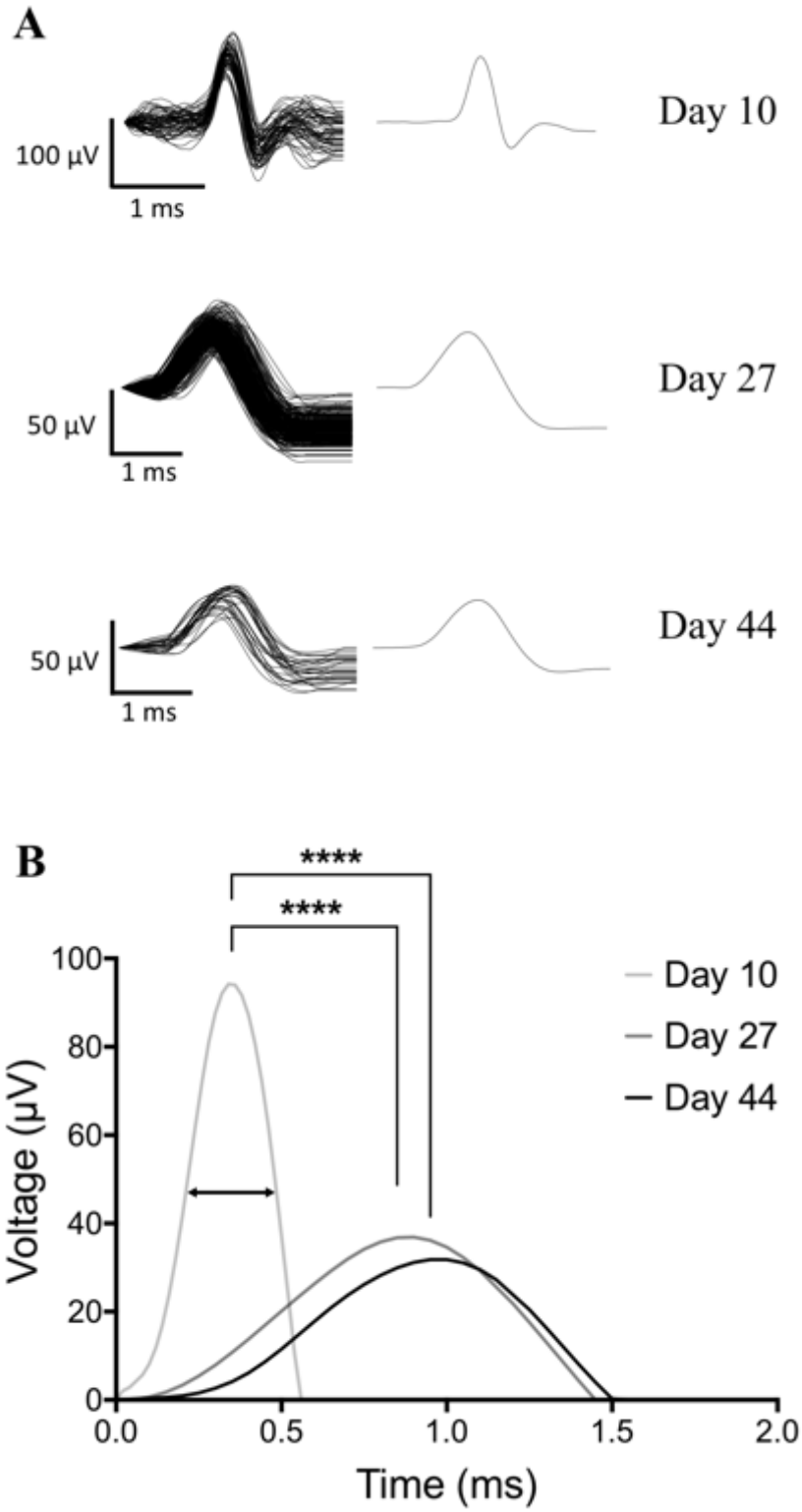

Figure 4.5: 'Fast' waveform activity from mouse spinal cord cultures recorded on commercial MEAs. (A) Three representative 'fast' waveforms recorded at 10, 27 and 44 DIV. Left trace shows all the waveforms sorted from one active channel for that day; 10 DIV = 64 spikes, 27 DIV = 238, 44 DIV = 30 waveforms. The trace on the right is the average of all the spikes. **(B)** Visualisation of the 'fast' waveform half-widths (double headed arrow) at 10, 27 and 44 DIV. Asterisks indicate statistical significance, **** $p < 0.0001$.

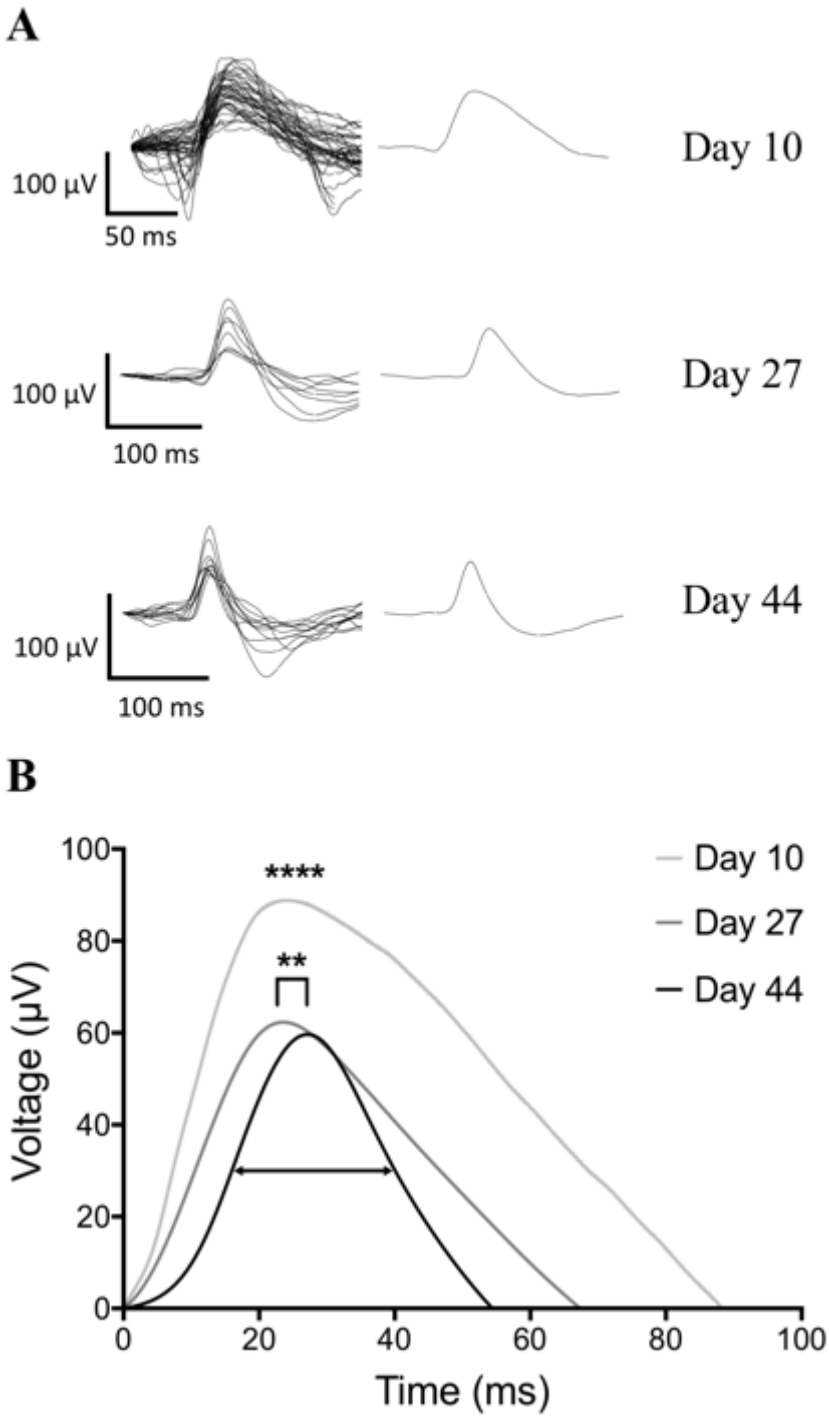

Figure 4.6: 'Slow' waveform activity from mouse spinal cord cultures recorded on commercial MEAs. (A) Three representative 'slow' waveforms recorded at 10, 27 and 44 DIV. Left trace shows all the spikes sorted from one active channel for that day; 10 DIV = 12, 27 DIV = 8, 44 DIV = 12 waveforms. The trace on the right is the average of all the waveforms. **(B)** Visualisation of the 'slow' waveform half-widths (double headed arrow) at 10, 27 and 44 DIV. Asterisks indicate statistical significance, ** $p < 0.01$, **** $p < 0.0001$.

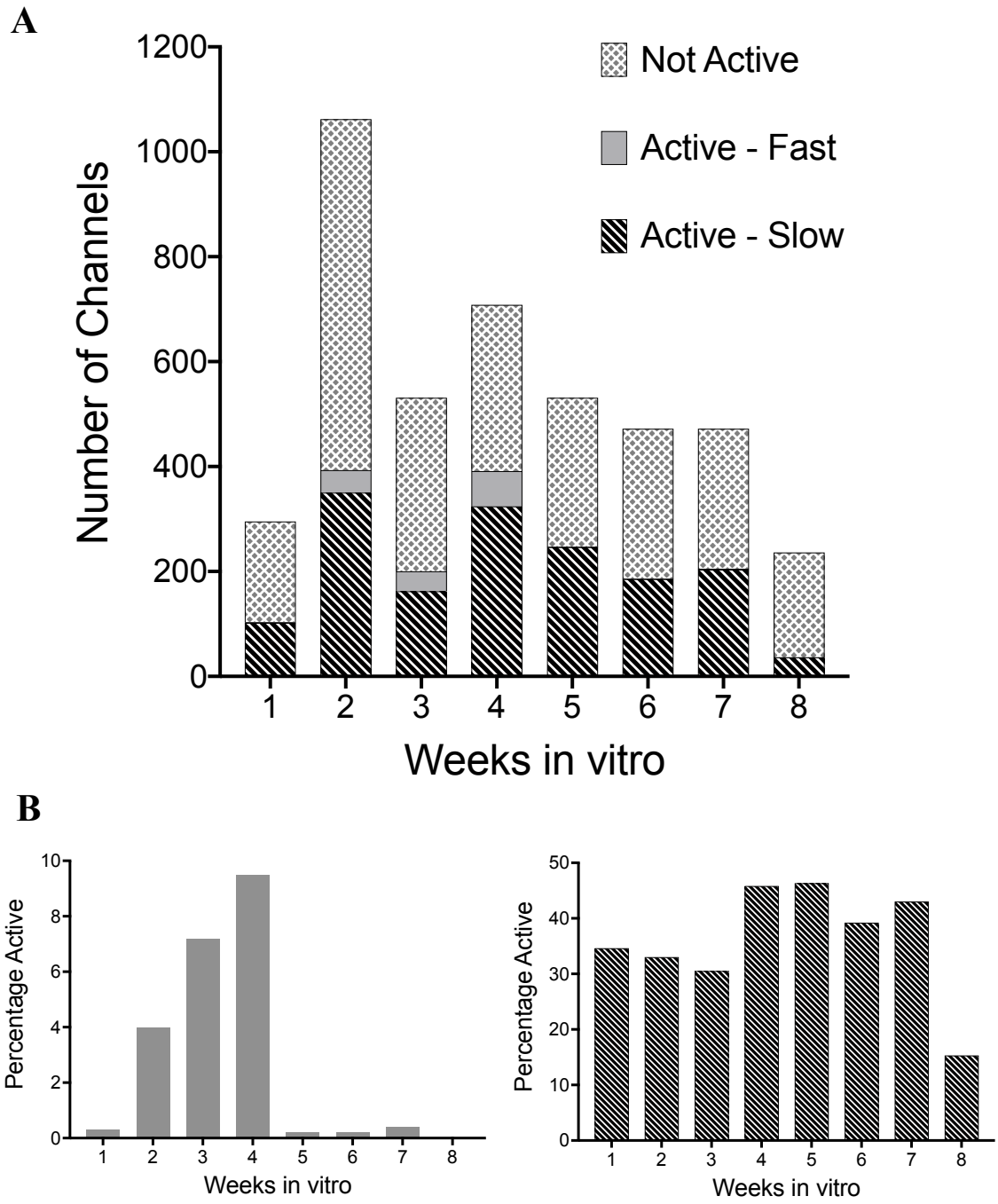

Figure 4.7: Number of channels with 'fast' and 'slow' waveform activity. (A) 'Fast' and 'slow' waveforms were observed throughout the whole culture period of the mouse spinal cord cultures up to 8 weeks *in vitro*. Each channel represents one MEA electrode with a total of 59 electrodes per MEA. **(B)** Percentage of channels with 'fast' (left) and 'slow' (right) waveform activity.

4.3.5 Spike Frequency

The spike frequency, over the period of 7 WIV, of active channels with 'fast' spike activity was calculated (**Figure 4.8A)**. An increase in spike frequency between 1 and 2 WIV was observed, however, no statistical significance could be found as there was only 1 active channel with 'fast' spike activity during 1 WIV. This was also the case for 6 WIV. The mean spike frequency was above 1 Hz for 2 to 5 and 7 WIV. To analyse the data for statistical significance the Kolmogorov-Smirnov test was used as the data were non-parametric and each week was separately statistically analysed compared to other weeks. The decrease in spike frequency from 2 WIV ($n = 42$) and 4 WIV ($n = 63$) was found to be statistically different ($p = 0.0074$). No statistically significant differences were found when comparing the spike frequency of the remaining data points as $p > 0.05$.

When compared to the spike frequencies of the 'fast' waveforms, that of the 'slow' waveforms was at least five times less, as it was below 0.2 Hz throughout 8 WIV (**Figure 4.8B**). To analyse the data for statistical significance, the Kruskal-Wallis test was used as the data were non-parametric and contained multiple samples. The increase in spike frequency of the slower spikes between 1 WIV and 4 WIV was found to being statistically significant ($p = 0.0015$). There was a significant increase in spike frequency between 2 WIV and 4 WIV ($p = 0.0009$) as well as a significant increase was found between 3 WIV and 4 WIV ($p = 0.0057$). Also, the decrease in spike frequency observed from 4 WIV to 7 WIV was found to be statistically significant ($p = 0.0067$).

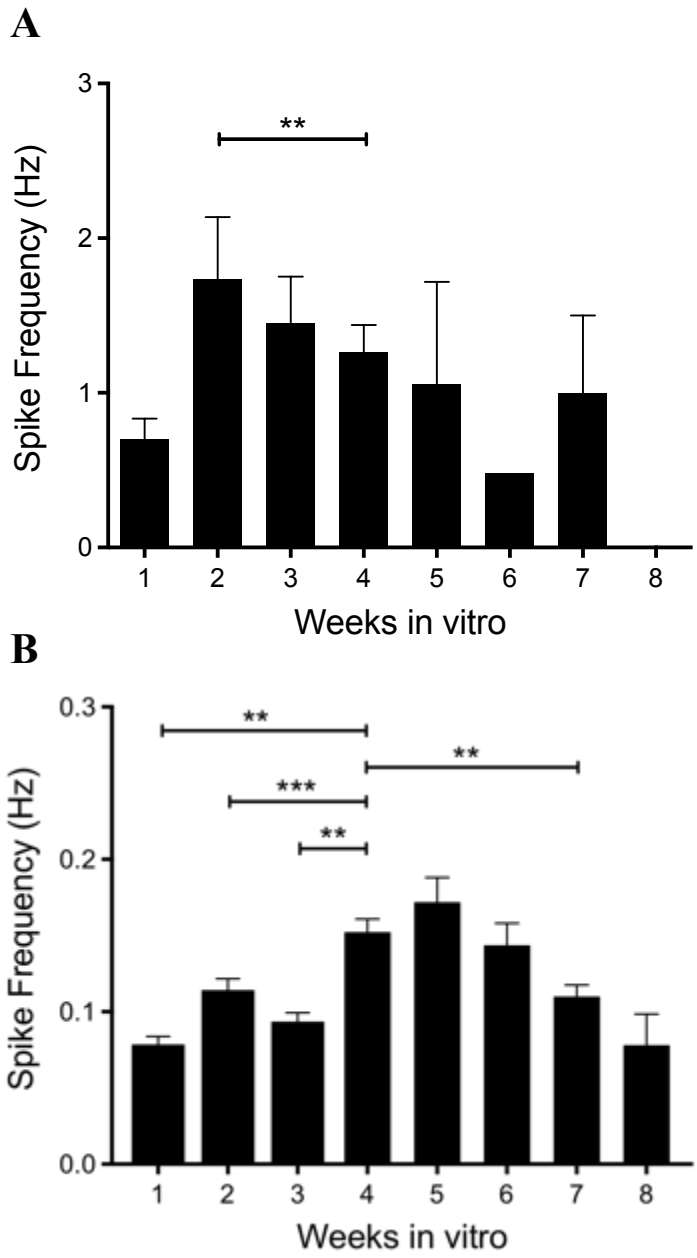

Figure 4.8: Spike frequency of mouse spinal cord cultures recorded on commercial MEAs. The frequency of **(A)** 'fast' and **(B) '**slow' spikes obtained over an eight-week period in culture. The data indicates that active channels comprised of 'fast' spikes had a higher spike frequency when compared to those with slow spikes. Data are presented as the mean and standard error of the mean used for error bars; asterisks indicate statistical significance, * $p < 0.05$, ** $p < 0.01$, *** $p < 0.001$.

4.3.6 Bursts of Activity in Mouse Spinal Cord Cultures

Once the spikes were sorted into 'fast' and 'slow' waveforms it was also observed that bursts of activity were present in the traces with 'fast' waveforms. Bursts of activity are often described as more than 2 spikes firing within a few milliseconds apart. The interevent interval measurement was used to observe if a burst of activity was present in an active channel.

The results show (**Figure 4.9A**) the coefficient of variation percentage from 6 DIV up to 48 DIV (last day where 'fast' waveform activity was recorded). The coefficient of variation percentage was calculated from the means and standard deviation of the interevent interval. When the percentage was above 100% (dashed line), bursts of activity were observed. Bursts of activity were observed between 9 and 23 DIV. Prior to 9 DIV and from 24 DIV and onwards the 'fast' spike waveform activity did not indicate any bursting activity. The data shown were from representative active channels and the number of waveforms and coefficient of variation percentages at each day are shown in **Table 4.1.**

A representative trace at 17 DIV (**Figure 4.9B**) shows what a burst in activity looks like (top). A closer look at the bottom trace, shows 13 'fast' waveforms all within 100 ms. A representative trace at 44 DIV shows no bursting of activity but instead single 'fast' electrical activity (**Figure 4.9C)**.

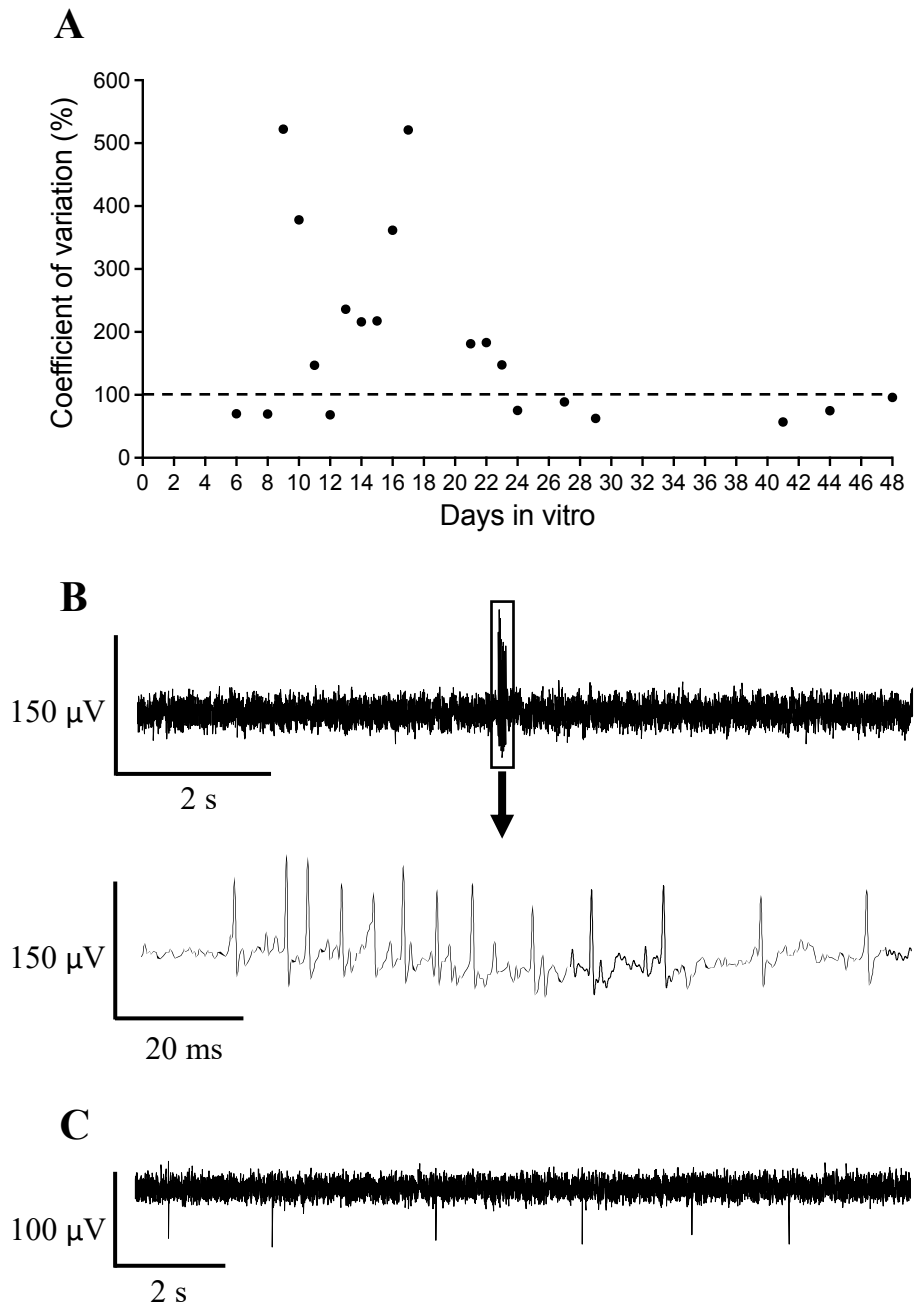

Figure 4.9: Coefficient of variation percentage of 'fast' waveforms from mouse spinal cord cultures between six to forty-eight days *in vitro*. (A) The coefficient of variation was calculated using the mean interevent interval and standard deviation. The interevent interval was obtained from electrically active channels that contained 'fast' waveforms. Values above 100% (dashed line) indicate bursts of activity present. Representative data shown for each day *in vitro*. The n values (number of spikes) varied from 6 (11 DIV) to 387 (21 DIV). The n values for each day can be seen in **Table 4.1**. Representative traces showing **(B)** bursts of activity at 17 DIV compared to **(C)** single spike activity at 44 DIV.

Table 4.1: Coefficient of variation percentage at different days *in vitro*. A percentage over 100 indicates bursts of activity.

Days *in vitro*	Coefficient of variation (%)	Number of 'fast' waveforms
6	70	50
8	69.63	115
9	522.2	78
10	378	171
11	146.9	6
12	68.33	8
13	236	26
14	216.1	35
15	217.4	363
16	361.7	65
17	520.9	34
21	181.2	387
22	183.1	148
23	147.7	364
24	75.3	58
27	88.69	76
29	62.64	103
41	56.83	29
44	74.76	30
48	95.86	90

4.3.7 Conduction Velocity Between Electrodes

'Fast' waveform activity was observed at similar time points within traces of different channels. In real-time, this difference was impossible to be distinguished (**Figure 4.10A**; two top traces). A closer look at the two bottom traces (**Figure 4.10A)** shows that the two waveforms still look fairly similar. This meant that it was necessary to automatically detect the time of peaks by using a peak value calculation with Clampfit software. Calculating the difference between closely correlated events on two adjacent electrodes, which were separated by a known distance, enabled me to calculate the nominal conduction velocity (NCV). NCV increased from 6 DIV up until 24 DIV, with a big jump from 6 to 10 DIV (**Figure 4.10B** and **Table 4.2)**. No further NCVs were calculated after 24 DIV as similar 'fast' waveforms were not detected in two separate channels or there was no more than one channel active. The slowest mean NCV was measured at 6 DIV (0.03 m/s) and the fastest was measured at 24 DIV (15.00 m/s). The data was statistically analysed using the Kruskal-Wallis test (with a Dunn's multiple comparisons test) as the data were non-parametric and contained multiple samples. There was a significant increase in NCV from 6 DIV (0.03 ± 0.0005 ms) to 23 DIV (13.12 ± 1.67 ms) ($p = 0.0206$). The increase in NCV observed between 6 DIV (0.03 ± 0.0005 ms) and 24 DIV (15.00 ± 1.95 ms) was also statistically significant ($p = 0.0023$). The increase in NCV measured at 24 DIV (15.00 ± 1.95 ms) when compared to that at 10 DIV (6.38 ± 0.99 ms) was found to be of significance ($p = 0.0116$). The NCV data are presented as the mean ± standard error of the mean.

The conduction velocity of 'slow' waveforms was also analysed (**Figure 4.11** and **Table 4.3)**. Unlike with 'fast' waveforms, when taking a closer look at two waveforms from two separate channels (**Figure 4.11A**; two bottom traces) the waveform peaks clearly arise at different times (vertical dashed lines apart from each other). This indicates that the NCV was slower than that of 'fast' waveforms. Indeed, this was the case as the fastest NCV recorded was 0.043 m/s at 6 DIV. Unlike with 'fast' waveforms, the NCV did not show an increase with time. It remained at around the same levels between 6 DIV and 44 DIV, ranging from 0.029 m/s (10 DIV) to 0.043 m/s (6 DIV). When comparing the fastest NCV recorded from 'fast' waveforms (24 DIV) to that recorded on the same day from active channels with 'slow' waveforms it was over 400 times higher. No statistically significant differences were found for any day when compared to each other as $p > 0.05$ after carrying out a Mann-Whitney test.

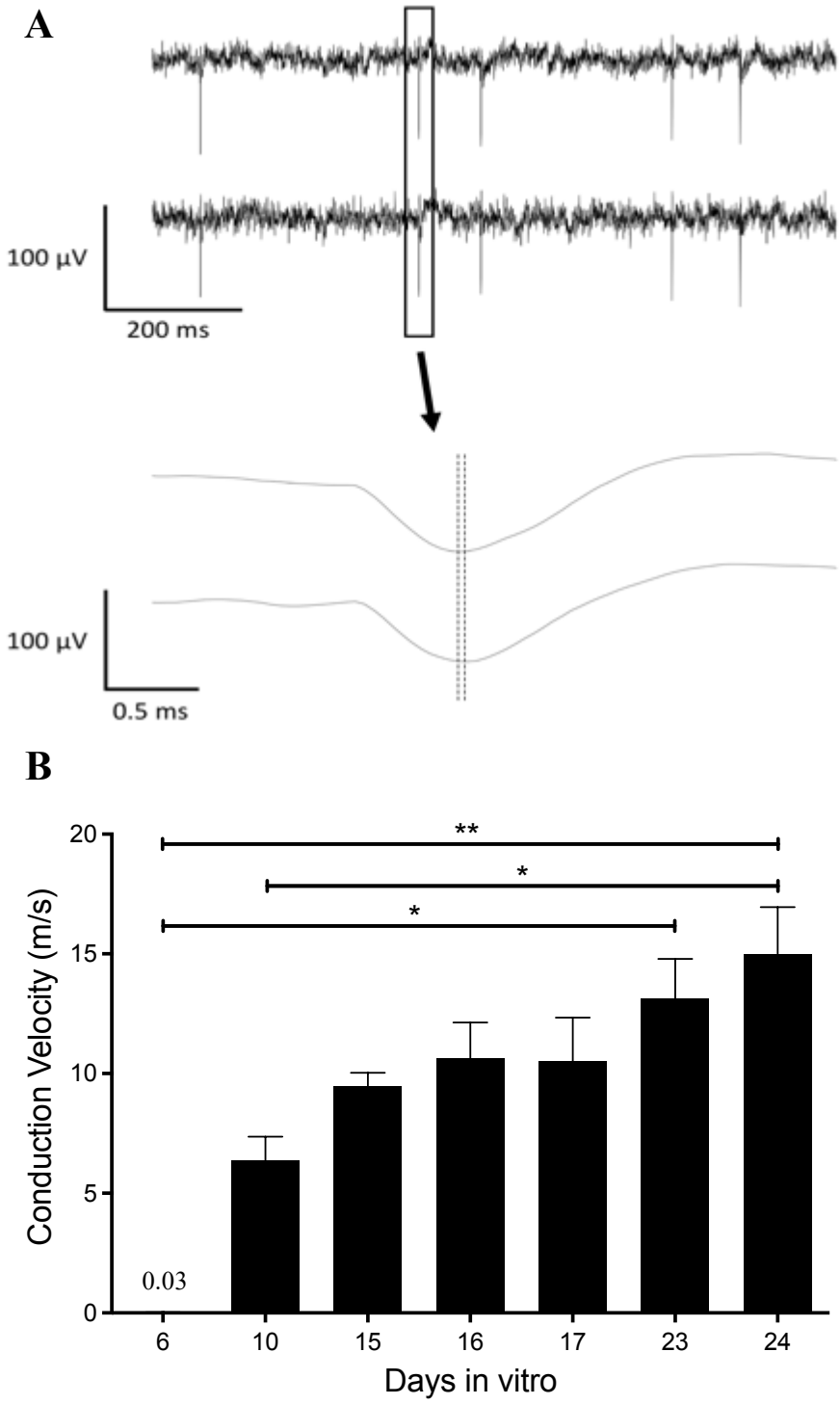

Figure 4.10: Nominal conduction velocity measured from 'fast' waveforms from mouse spinal cord cultures on commercial MEAs. (A) Representative traces of two channels at 24 DIV with 'fast' waveform activity. A closer look at the two spikes waveforms are shown in the bottom traces. **(B)** The conduction velocity was calculated from 'fast' waveforms that were present in two separate channels (distance apart ranged from 200 to 1000 µm). The n values (number of pairs of waveforms compared) were as follows: 6 DIV = 4, 10 DIV = 21, 15 DIV = 9, 16 DIV = 10, 17 DIV = 5, 23 DIV = 17, 24 DIV = 12. Data are presented as the mean and standard error of the mean used for error bars; asterisks indicate statistical significance, * $p < 0.05$, ** $p < 0.01$, *** $p < 0.001$.

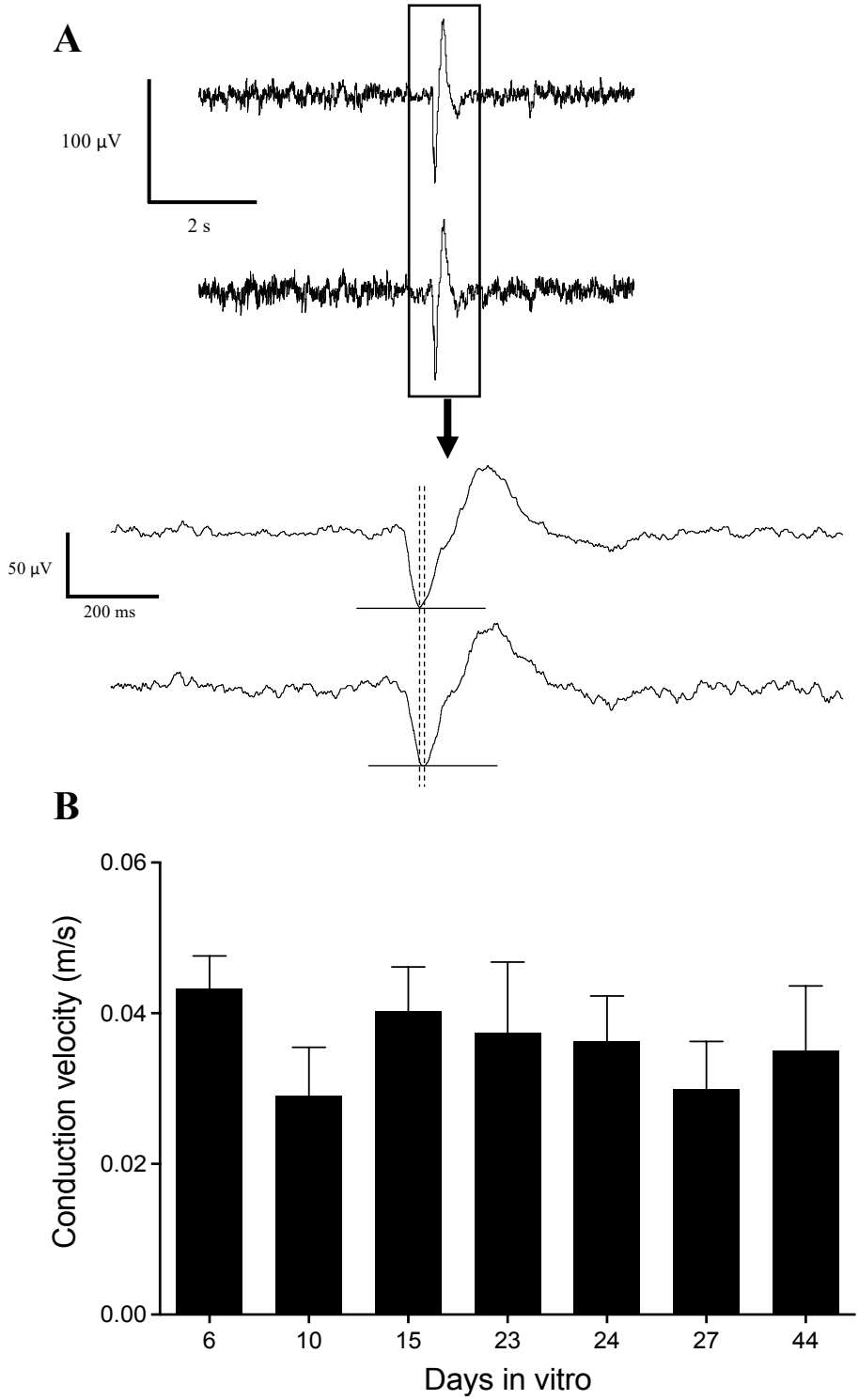

Figure 4.11: Nominal conduction velocity measured from 'slow' waveforms from mouse spinal cord cultures on commercial MEAs. (A) Representative traces of two channels at 27 DIV with 'slow' waveform activity. A closer look at two spikes waveforms are shown in the bottom. **(B)** The conduction velocity was calculated from 'slow' waveforms that were present in two separate channels (distance apart ranged from 200 to 725 µm). The n values (number of pairs of waveforms compared) were as follows: 6 DIV = 2, 10 DIV = 5, 15 DIV = 7, 23 DIV = 20, 24 DIV = 45, 27 DIV = 17, 44 DIV = 34. Data are presented as the mean and standard error of the mean used for error bars.

Table 4.2: Mean nominal conduction velocity of 'fast' waveforms from mouse spinal cord cultures pre and post myelination measured on commercial MEAs.

Day *in vitro*	Nominal Conduction Velocity (m/s)	SEM
6	0.03	0.00053
10	6.38	0.99
15	9.47	0.56
16	10.63	1.51
17	10.50	1.84
23	13.12	1.67
24	15.00	1.95

Table 4.3: Mean nominal conduction velocity of 'slow' waveforms from mouse spinal cord cultures 'pre and post myelination measured on commercial MEAs.

Day *in vitro*	Nominal Conduction Velocity (m/s)	SEM
6	0.043	0.004
10	0.029	0.006
15	0.040	0.006
23	0.037	0.009
24	0.036	0.006
27	0.030	0.006
44	0.035	0.009

4.3.8 Mouse Spinal Cord Cultures on Custom MEAs

Mouse spinal cord cultures were also grown on custom MEAs. The cultures remained adhered well on the surface used (SiO_2) for up to 21 DIV (**Figures 4.12A-C)**. The cells were also cultured in a two well PDMS module with microchannels. Cell growth did not change compared to the single well PDMS module. However, the growth of processes/axons through the microchannels and into the second compartment was not observed. Different attempts to encourage such growth included adding mouse spinal cord cells in both wells, as well as adding nerve growth factors in the second well not containing cells. Neither of these changed the outcome and no processes extended into the second compartment. When microchannel width was varied (two different sizes of microchannels were used, 5 or 10 μm in width, 100 μm in length and 25 μm in height) the outcome remained the same.

Issues with the earlier versions of custom MEAs (outlined in Chapters 2 and 3) resulted in no electrical activity to be recorded. Since updating the custom MEAs to the newer version MEAs (V3.2) electrical activity was recorded as cells were successfully cultured on them. However, as the interelectrode distances of the custom MEAs was greater than that of commercial MEAs, less cell coverage over electrodes was observed which affected the electrical activity recorded as it was unlike that obtained from commercial MEAs. This resulted in fewer active channels (1 - 4 out of 16) which only showed 'slow' waveform activity and no 'fast' activity (**Figure 4.12D**). This was not surprising as on commercial MEAs where total coverage was achieved 'fast' waveform activity was less than 10% (**Figure 4.7B**).

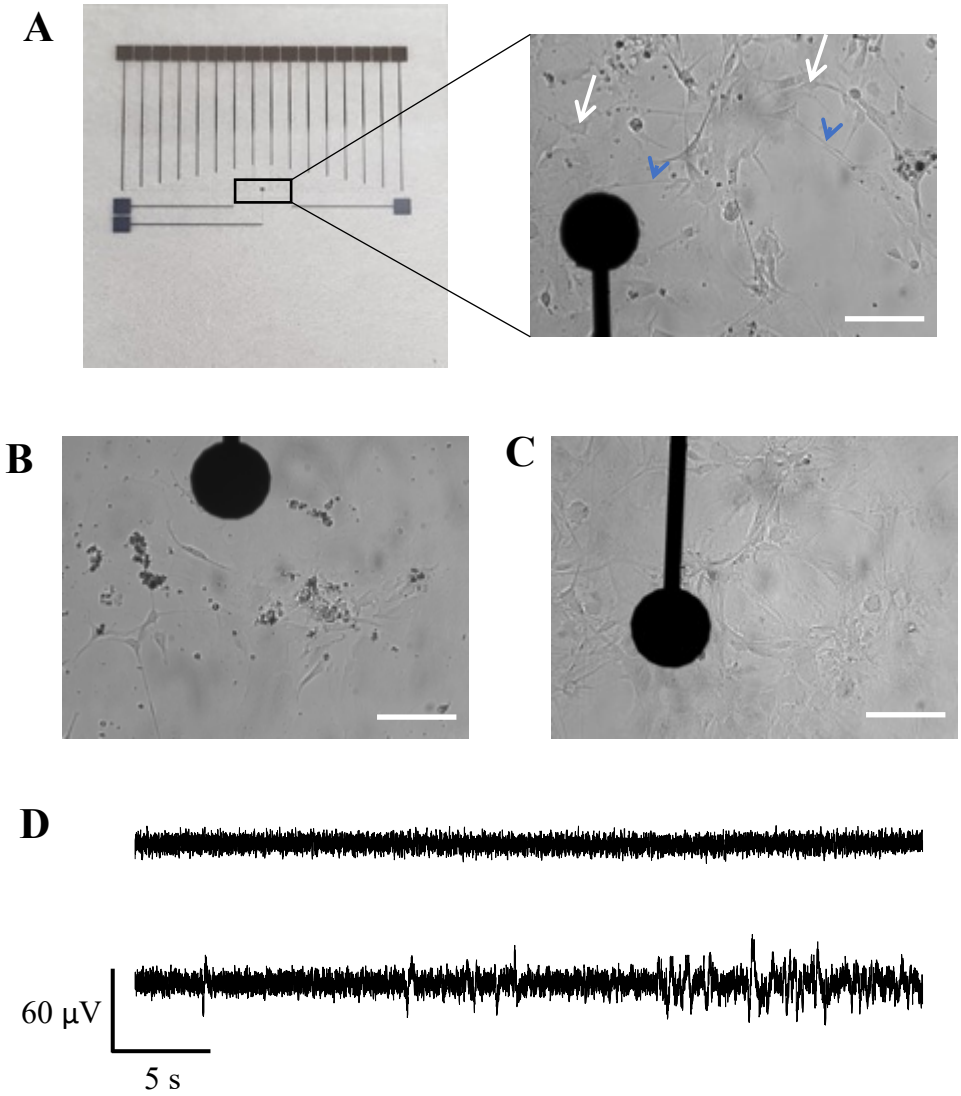

Figure 4.12: Mouse spinal cord cultures on custom microelectrode arrays. (A) Low power view of custom MEA on the left. In the high-power image (right), one electrode (black circle) can be observed in relation to the cell bodies (white arrows) and processes (including axons; blue arrowheads) of neurons and glia, on an MEA at 15 DIV. Representative images at **(B)** 17 DIV and **(C)** 21 DIV. (**D**) Representative traces showing non-active (top) and active (bottom) channels recorded on custom MEAs. Scale bar = 50µm.

4.4 Discussion

Mouse spinal cord cultures have been used for decades to study the central nervous systems and have proved particularly useful to study the process of myelination (Bird and James, 1975; Bijland *et al.*, 2019). However, most studies base their findings on static changes in neuron-glial interactions using techniques such as electron microscopy and immunocytochemistry. Here I have shown that there are detectable changes in electrical behaviour with time and that as myelination progresses it became harder to detect 'fast' waveform activity. This is most likely due to the insulating myelin preventing electrical signals associated with spike propagation being detected. Most notably, by using a non-biased measurement of electrical waveform delay between electrodes I was able to detect an acceleration of nominal conduction velocity (NCV) with time in *in vitro* myelinating cultures for the first time (at such values). The bulk of the data obtained was from commercial MEAs but there were some tests carried out on custom MEAs.

The use of MEAs can further supplement the findings of studies that use markers such as those used in our recent paper (Bijland *et al.*, 2019) to help us gain a more detailed understanding of the process of myelination in the CNS, as well as other CNS functions such as spontaneous electrical and synaptic activity. Neuronal electrical activity can be used to identify the cell types present in the spinal cord cultures, their metabolic status and the general health of the cultures. The use of MEAs have an advantage over single cell patch clamp recordings as the throughput is much higher and the cultures can be monitored 24 hours a day for as long as the cultures can be kept alive. MEAs allow for recordings to be obtained from the whole cell culture and provides a more nuanced readout of electrical activity.

Thousands of traces of extracellular electrical activity were obtained throughout the whole period of mouse spinal cord cells cultured on MEAs (2 to 52 DIV). A lot of information can be extracted from a single active trace which is what I show in this chapter. MEAs are shown to be ideal for following the cultures on a day to day basis which facilitates in understanding how these mouse spinal cord cultures develop *in vitro*. It was also shown that the MEA cultures react to pharmacological stimuli which means that they can be used for drug screening purposes.

4.4.1 Pharmacological Assessment of Mouse Spinal Cord Cultures

Spinal cord cultures for pharmacological experiments were plated onto commercial MEAs and 35 mm cultures dishes at 14 DIV and were kept up to 24 DIV. The cultures were tested on a day-to-day basis for electrical activity using voltage-clamp on the 35 mm dishes and MEA recordings on the commercial MEAs. At 24 DIV a series of drugs were added to the culture. The results with single cell voltage-clamp showed that the cultures were electrically excitable and corelated well with the MEA recordings. Additive pharmacology was done in order to gain a better understanding of what types of activity were present in the culture as it contained a mixture of neuronal and glial cells. The addition of a GABA receptor antagonist, picrotoxin, caused a massive increase in 'fast' spike frequency. This suggests that inhibitory neurons are present in the culture which were previously suppressing any form of spontaneous activity. Following this, TTX was added to the culture to see its effect on axonal action potential, as TTX is a voltage-gated sodium channel blocker. Indeed, TTX caused the reduction of 'fast' waveforms which therefore suggested this activity was due to axonal potentials. CNQX, an AMPA receptor antagonist, was then subsequently added which blocked some of the 'slow' spike like activity still present in the presence of TTX. The blocking of these 'slow' waveforms suggests the presence of glutamatergic neurons and that some of the electrical activity present in these cultures arose from the synaptic release of glutamate. The nature of the inhibition with GABA and CNQX further suggest that the 'slow' waveforms are synaptic, generator or dendritic potentials (Kullmann *et al.*, 2005).

These results were validated by the single cell current clamp recordings. They also showed an increase in activity with the addition of picrotoxin and the activity was blocked with the further addition of TTX and CNQX. The ability to use MEAs to show both a pharmacological response in mouse spinal cord cultures means they can be used as an additive technique in studying the CNS.

4.4.2 Electrical Activity of Mouse Spinal Cord Cultures

Electrical activity from embryonic day 13 (E13) mouse spinal cord cultures was detected on MEAs as early 2 DIV. This was not entirely surprising as mouse spinal cord neural networks are known to be electrically active at E12.5 (Yvert, Branchereau and Meyrand, 2004) therefore the dissociated cells would be expected to become active as soon as the

isolation trauma has passed. In our previous work (Bijland *et al.*, 2019), we did not investigate electrical activity prior to 20 DIV and after 24 DIV. Here I use MEAs to study the cultures for a longer period of time starting at 2 DIV and concluding at 52 DIV which enabled me to follow with much greater precision the development of the spinal cord cultures. This is particularly useful information as neural activity has been linked to the process of myelination (Shimba *et al.*, 2019) and other neuron-glia interactions (Wanke *et al.*, 2016).

About 34% of the channels were electrically active in the first week in culture. The electrical activity remained at about the same levels at 2 and 3 weeks. During weeks 2 and 3, it is known that myelin sheaths begin to form (Thomson *et al.*, 2008). From 3 weeks onwards, the myelin sheaths continue to mature but are more distinct and abundant in mouse myelinating cultures which may explain the increase, to about 56% of active channels at 4 weeks *in vitro*. The average number of spontaneous active channels remained higher from 4 weeks to 7 weeks when compared to the activity in the first 3 weeks.

During week 7, the cultures were no longer as healthy as they were in the previous weeks as they began to detach and less cells adhered to the surface of the commercial MEAs. This was indicative of the drop in the number of active channels as an increased amount of cell death was observed during week 8. Therefore, the decision was taken stop at 52 days which was subsequently a much longer time frame than previous studies, where normally axonal degeneration is studied for up to 14 DIV (Mikhailova *et al.*, 2019) and up to 31 DIV when studying CNS development and functionality (Bijland *et al.*, 2019). Thus, my work here extends the experimental time window for such studies by two to three weeks.

One possible reason for the ultimate deterioration of the cultures could have been the regular transportation of the cultures from the incubator (37ºC) that was in the tissue culture room to our lab (20ºC) and then onto my set-up (37ºC). Regular changes in temperature are known to induce a cellular stress response (Neutelings *et al.*, 2013) which could explain the culture deterioration by week 8. Therefore, if the setup used for recording had a heated/gas enclosure it would mean the MEAs could remain in there throughout the whole experimental period. This would avoid any damage caused by transportation and exposure to sudden changes in temperature (37°C to 20°C).

4.4.3 Classification of Electrical Activity

4.4.3.1 'Fast' and 'Slow' Waveforms

When analysing through all the traces, it was clear that the types of waveforms varied with time and therefore, I examined this aspect in more detail. Initially the spikes had to be sorted into two groups, 'fast' and 'slow' waveforms. The half-width of neuronal action potential varies depending the type of neuron and the recording site, for example the waveform half-widths of motor and cortical neurons varies between 0.5 to 2 milliseconds (ms) whereas that of dopaminergic neurons of mouse brain slices is not less than about 4 ms (Bean, 2007). As motor neurons are also present in the mouse spinal cord (Stifani, 2014), in my analysis, for a spike to be placed in the 'fast' group its waveform duration had to be less than 3 ms. Any spikes whose waveforms were broader than 3 ms were placed in the 'slow' group.

The half-width data allowed for differentiating between the different waveforms observed at different days. It was found that the 'fast' and 'slow' waveforms changed with time *in vitro*. The 'fast' spikes waveform was narrower pre-myelination (10 DIV), whereas post-myelination (27 and 44 DIV) the waveform was about three times broader. This could be explained by the changes in sodium ion channel distribution on the axons of unmyelinated and myelinated axons. Unmyelinated axons have voltage-gated sodium channels evenly distributed along them. $Na_v1.2$ (one of the several sodium channel α subunits) channels are predominately expressed in unmyelinated axons (Vacher, Mohapatra and Trimmer, 2008). As the axons become myelinated $Na_v1.2$ channels become replaced by $Na_v1.6$ channels which are expressed at the nodes of Ranvier (Van Wart and Matthews, 2006). This also explains why most 'fast' waveforms were predominately present in active channels at 3 and 4 WIV (during myelination and myelin maturation) and are later lost presumably because of myelin covering the majority of the axons over the recording electrodes.

The number of active channels consisting of 'fast' waveform activity at 4 WIV was about 2.5 times greater when compared to 'fast' waveform activity containing channels at 2 WIV (pre- and early myelination). The reduction of 'fast' waveform activity after 4 WIV could be due to the increase of juxtaparanodal fast potassium currents which suppress re-

excitation to a certain extent (Vabnick *et al.*, 1999) or insulation of the axons close to the electrodes.

Unlike 'fast' waveforms, 'slow' waveforms became narrower as the number of days in culture increased, (mean half-width was 48.5 ms at 10 DIV and 24.9 ms by 44 DIV). 'Slow' waveforms were observed throughout the 8 WIV with not much variation, except at 8 WIV when the percentage of channels consisting of 'slow' waveforms was reduced to 15.3% from 43.0% at 7 WIV. As synaptic activity was demonstrated here both pharmacologically and electrophysiologically with whole cell voltage-clamp, these slower waveforms were attributed to synaptic potentials. The decrease in half-width of 'slow' waveforms as the DIV increase could be explained by several different factors such as the change in distribution of calcium channels on myelinated axons from unmyelinated axons (Lai and Jan, 2006). Another factor could be the increase in glutamate transporters due the maturation of glial cells (Martinez-Lozada *et al.*, 2014). Both of these features shorten and intensify the synaptic potential as synapses mature.

4.4.3.2 Spike Frequency and Bursts of Activity

MEAs also provide the opportunity to study the spike frequency and bursting activity of a mixture of cells which is a good proxy of the overall network activity. Knowing the firing rate of the cultures as the DIV increase and when bursts of activity arise, helps build a picture of axonal and synaptic maturation. My spike frequency results were similar to the results of another study which looked at mouse ventral horn (spinal) cultures (Black, Atmaramani and Pancrazio, 2017), where it was found that spike frequency of 'fast' waveforms increased after 1 WIV and remained between 1 to 2 HZ throughout the remaining culture period.

I used the interevent interval between spike peaks and their coefficient of variation expressed as a percentage to define burst-like activity. A coefficient of percentage above 100% is a strong indication that bursts of activity were present. Bursts of activity were found to be present in cultures after 1 WIV. This coincided with the increase in 'fast' waveform frequency mentioned earlier. Bursts were present between 9 and 23 DIV. This could be explained by the beginning and progression of myelination as well as the differentiation and maturation of the glial cells (Thomson *et al.*, 2008).

4.4.4 Assessing Myelination of Mouse Spinal Cord Cultures through Electrode-to-Electrode Conduction Velocity

Myelination has been studied for decades using techniques such as electron microscopy (Morris, Hudson and Weddell, 1972) and immunocytochemistry (Sternberger *et al.*, 1978; Thomson *et al.*, 2006). Studies in mice show that it is important to distinguish if the myelination is compact or loose, as in the absence of compact myelin neuronal cytoskeleton maturation was negatively affected (Brady *et al.*, 1999) and conduction velocity (measured *in vivo*) in the optic nerve of proteolipid protein (PLP)-deficient mice which have non compact myelin sheaths was impaired (Gutiérrez *et al.*, 1995). Thus, a more accurate evaluation of myelination state would be to measure nominal conduction velocity (NCV) in culture which has the advantage of being a repeated measure for the same culture for as long as the culture can be kept alive. I examined this idea using custom MEAs with integrated microchannels. When this approach failed, I used commercial MEAs with electrode-to-electrode connectivity and conduction delays as a proxy for axonal conduction. In this case, the electrical activity recorded from mouse myelinating cultures on commercial MEAs could be used as an approach to study myelination *in vitro*.

I found that electrode-to-electrode NCV increased precipitously from 6 DIV to 24 DIV, indicating an increase in development and compaction of myelin previously undetected with other methods and also correlating with immunocytochemical observations. Bijland *et al.*, (2019) showed using positive CNP staining that early myelin sheath formation occurred at 12 DIV and continued forming around axons as the days progress. Previous studies indicated that myelination began at about 15 DIV, with the majority of myelination occurring between 17 to 23 DIV. This was seen through electron microscopy images and myelin marker (myelin basic protein, MBP) immunostaining (Thomson *et al.*, 2006). Therefore, the NCV data shown in this chapter confirms that myelination progresses as the number of days *in vitro* increases. However, an increased NCV was observed from as early as 10 DIV, which could indicate that myelination may begin a few days earlier than previously reported and/or that maturation of axons and moderate increases in NCV occur prior to myelination. The velocity of around 0.03 m/s was found at 6 DIV and by 24 DIV this was significantly increased to 15.00 m/s. This is the first time such high NCVs have been recorded *in vitro* and is similar to velocities seen in *in vivo* experiments (Mozafari *et al.*, 2015). Previous *in vitro* myelin studies show conduction velocities ranging between 1 – 2 m/s (Freeman *et al.*, 2015) and 0.44 – 0.59

m/s (Sakai *et al.*, 2017). Unlike electron microscopy, using MEAs to assess the progress of myelin compaction is more advantageous as the cells do not require to be fixed and can be kept alive for as long as required. Also, unlike MEAs, immunocytochemistry is unable to distinguish between non-compact and compact myelin. However, I was unable to measure possible NCVs higher than 15 m/s due to the sample rate limit from the amplifier filters used and this could also explain the lack of faster NCVs in previous studies.

It was also important to look at changes in conduction velocity of the 'slow' waveforms as that would indicate if myelination had also affected the other aspects of cells electrical activity. Unsurprisingly, it was found that the conduction velocity measured from 'slow' waveforms remained fairly constant throughout the culture and ranged between 0.029 to 0.043 m/s, indicating that NCV changes did not alter in the non-myelinated portions of the neurons from as early as 6 DIV up to 44 DIV reinforcing the view that the 'fast' waveforms were axonal spikes.

Another way to confirm that the NCVs recorded from mouse spinal cord cultures were due to the maturation of myelin and not caused by other factors such as straightening of axonal branches, increases in axonal diameter or redistribution and optimisation of ion channel coverage of the axon surface, would be to measure the effect of carrying out demyelination *in vitro* using cuprizone (cuprizone induces demyelination both *in vivo* and *in vitro* (Matsushima and Morell, 2001)*)*. A good timepoint for this experiment would be at 24 DIV, when a decrease in NCV should be clearly observed. This would further increase confidence in the findings in this chapter. This experiment could be repeated earlier on, for example at 6 DIV, and observe any changes in NCV in the presence of cuprizone. The hypothesis would be that the NCV would not increase after 6 DIV in the presence of cuprizone.

Furthermore, remyelination could be assessed by the removal of cuprizone after demyelination has occurred. Remyelination has been reported in mice once they are taken off a cuprizone diet (Blakemore, 1973). Therefore, it is hypothesised that removing cuprizone from the culture should cause remyelination and thus begin to see an increase in NCV as the time passes. Once this demyelination/remyelination on MEAs is established, novel drugs can be tested on neuronal cultures to study their neuroprotective properties as well as their remyelination efficacy.

4.4.5 Mouse Spinal Cord Cultures on Custom MEA

Several iterations of custom MEAs (V2.0, V3.0, V3.2, V3.4) were used for the experiments in this chapter to enable better measurement of NCV. The main hurdle to overcome was to achieve long term culture similar to multi-well plates and glass. The use of silicon dioxide (SiO_2) for the surface (insulating layer) of the MEA was found to be ideal. The custom MEA was designed in a way to allow both stimulation and recording from the culture. A PDMS module, bonded onto the surface of the MEA, consisting of two wells separated by microchannels allowed for separation of stimulating and recording electrodes. The purpose of the microchannels was to restrict the cell bodies in the stimulating compartment and for the neuronal processes to grow through the microchannels and into the second recording compartment. The issue with the mouse spinal cord cultures that arose was that the axons would not grow through the microchannels but remained in one compartment together with the cell bodies. At first, the issue was that a number of cell bodies would flow through the microchannels before adhering onto the surface and that was solved by reducing the width of the microchannels to 5 μm from 10 μm. This reduction was found to restrict the cell bodies in one compartment; however, the axons still did not grow through the microchannels. Therefore, no recordings could be carried out in this culture.

Alongside the microchannel PDMS module, single well PDMS modules without microchannels were also used in order to replicate commercial MEAs that had one single well where the cells were seeded. This meant that cells would definitely be growing over some of the recording electrodes of the custom MEA. Therefore, the quality of the electrodes could be assessed. On early custom MEAs, electrical activity was not recorded due to inaccurate/faulty electrode exposure (either the electrodes were not fully exposed, or they were fully coated by the insulating layer). Later, by improving the accuracy of the deposition of the insulating SiO_2 layer functional electrodes were fabricated (see Chapter 2). Following the adjustments in the deposition of the SiO_2 layer, electrical activity was recorded from the custom MEAs (V3.2 and V3.4).

4.5 Conclusions

Mouse spinal cord cultures, studied electrically using commercial MEAs over a period of 50 days, were electrically active from as early as 2 DIV. Electrical activity was characterised as ‘fast’ and ‘slow’ which meant that the extracellular recordings were from different neuronal structures such as the cell body, axons and dendrites. The development of myelination was investigated by measuring electrode-to-electrode nominal conduction velocity which increased from 6 DIV up until 24 DIV. The velocities measured in this chapter are the highest recorded thus far *in vitro*. Therefore, MEAs ability for long-term recording from live neuronal cultures without disturbing the cells makes them a great tool for assessing myelination and thus used for developing novel *in vitro* neurodegenerative disease models.

Chapter 5

General Discussion

In this thesis, I have successfully combined human and mouse neuronal cultures with microelectrode arrays (MEAs) and microfluidic modules. Following an initial shortcoming with the custom MEAs produced by Epigem Limited, I was able to fabricate them myself at the nanofabrication facility of Heriot-Watt University. This allowed me to trial different versions with a fast turnaround from idea to product. The first iterations were not up to standard as not all electrodes were functional due to problems with electrode and insulator deposition. Also, the cells would not adhere onto them for long periods of time and therefore I was unable to record from them. Once these issues were overcome, I was able to use custom MEAs to record from human dopaminergic cultures and mouse spinal cord cultures.

The purpose of fabricating my own custom MEAs and not only use what is commercially available was to produce a low-cost biochip with embedded microchannels that would guide axonal growth over recording electrodes and restrict neuronal cell bodies in a separate stimulating compartment that could be used to investigate myelination *in vitro*. I showed that the microchannels fabricated functioned as hypothesised by allowing only axonal growth of human cerebral cortical neurons (hCCNs) through into the second compartment. However, I was not able to record from the biochip as the hCCNs did not grow on it long enough for the axons to pass through the microchannels and also obtain any recordings from.

Biochips were tested with mouse spinal cord cultures and human dopaminergic cultures too but still no growth through the channels was observed. However, myelination *in vitro* was electrically investigated using commercial MEAs and mouse spinal cord cultures. Electrode-to-electrode nominal conduction velocity (NCV) was measured which increased significantly between 6 days *in vitro* (DIV) and 24 DIV where it reached a peak velocity of 15 m/s. This shows that MEAs can be used to follow myelination *in vitro* and therefore can be done in the biochips I fabricated with human neurons in order to develop novel human *in vitro* multiple sclerosis and other disease models.

I believe that myelination is not assessed electrically as much as other techniques due to the multiple difficulties that arise when incorporating different technologies like MEAs, microfluidics and human neurons. However, with my biochip (following a few tweaks) this hurdle can be overcome.

5.1 Microelectrode Arrays and Culture Issues

Following already established techniques such as photolithography and physical vapour deposition I fabricated functional custom MEAs on which CNS cells successfully adhered onto and were maintained in cultures for 3 to 6 weeks. The different versions I designed and fabricated are detailed in Chapter 2 (**Table 2.1**).

The choice of materials and dimensions were based on the findings from previous studies and the cost of materials. In order for the metal to be a suitable substrate for long term culture it had to have good electrical conductivity properties and be non-toxic. Possible candidates included gold (Au), platinum (Pt) black and titanium (Ti). These metals are found in most of the commercially available MEAs from companies such as Multichannel Systems (Reutlingen, Germany) and Ayanda Biosystems (Lausanne, Switzerland). Au was first considered as it is commonly used, but its high cost meant it was quickly ruled out as it was important for the custom MEAs to have a low cost for future possible commercialisation and also aligned with the relatively cheap cost of the whole recording set up. Similarly to Au, Pt black was also ruled out because of its price but also due to it having issues with adhesion and reproducibility. This is because it needs to be redeposited after every culture as it is removed during the cleaning process (Eick *et al.*, 2009). Therefore, Ti was the ideal candidate due to its low cost, good electrical conductivity and lack of toxicity (Kim *et al.*, 2018).

The electrode diameters ranged between 20 to 80 μm for the different versions. The final diameter chosen (V3.2, V3.4 and V4.0) was 50 μm which was greater than that of the commercial MEAs used (30 μm). MEAs have electrodes of various diameters concentrated in a small area in order to increase the spatial resolution of the recorded signal, however, the smaller the electrode size the higher the impedance which results in a low signal to noise ratio (Cogan, 2008). Therefore, slightly bigger electrodes were chosen as to have a lower impedance and thus a better signal to noise ratio than that obtained from the commercial MEAs.

I found that culturing and differentiating hNSCs on commercial MEAs was not possible as during the differentiation process the cells were no longer adhered onto the surface (Chapter 3). After trying different coating solutions as an attempt to improve cell adherence on the commercial MEAs and not observing any improvement, I decided to

use an alternative insulating layer for the custom MEAs. Therefore, instead of Si_3N_4, I used SiO_2. SiO_2 is widely used in the field for insulating purposes as it also is biocompatible and has better insulating properties (higher resistivity) than Si_3N_4 (Bartzsch *et al.*, 2009). Culturing and differentiating hNSCs on SiO_2 showed an improvement as the density of the cells did not drop as quickly as that of those cultured on Si_3N_4. However, all cells eventually detached after 2 to 3 weeks.

On the other hand, human dopaminergic cultures and mouse spinal cord cultures were maintained on the custom MEAs for as long as those cultured on commercial MEAs. Therefore, the use of SiO_2 for the insulating layer could be considered an improvement compared to Si_3N_4.

5.2 Microchannels for Axon Isolation

In Chapter 2 I described the fabrication process of making microchannels of different dimensions using soft lithography. The purpose of these microchannels was to separate the neuronal cell bodies from the axons as the cell bodies would be restricted and remain in the first compartment while the second would only contain axons. This was achieved with microchannels measuring 5 μm in width, 50 μm in length and 25 μm in height. hNSCs were seeded into the left-hand side compartment and were differentiated into hCCNs. Only axonal growth was observed in the right-hand side compartment as the cell bodies were successfully prevented from flowing and adhering in the right-hand side compartment by the 5 μm microchannels.

The result achieved was expected as it has been shown by several other studies who used a similar concept design (compartments separated by microchannels) to investigate axonal growth (Park *et al.*, 2014) and axon/glia interactions (Park *et al.*, 2012). The compartment layout for both these studies was different to the one I used as it was important for the microchannels to align with the electrode layout of the custom MEAs. Another difference was the dimensions of the microchannels. For investigating axonal growth, the Park *et al*., (2014) module consisted of microchannels measuring 20 μm in width, 10,000 μm in length and 3 μm in height. The reason for the 200 times greater microchannel length was that they were looking at how axonal growth was affected by various treatments and therefore wanted to visualise axons growing separately through microchannels. My microchannel dimensions were closer to those of the axon/glia study

(Park *et al.*, 2012) that had microchannels measuring 20 μm wide, 3 μm high and 400 μm long as the end goal was to add glial cells in the axonal compartment to study myelination electrically *in vitro.*

Another design option was to have longer microchannels and have glia growing within the channels which was a concept tested by Sakai et al., 2017. They cultured DRG neurons whose axons grew through microchannels that contained Schwan cells and could stimulate and record from a series of electrodes aligned along microchannel measuring 50 μm wide, 2000 μm long and 6 μm high (**Figure 1.9**). The peak conduction velocity recorded was 0.59 m/s at 32 DIV which when compared to the velocities measured from mouse spinal cord cultures in this thesis was much slower. A direct comparison cannot be made due to the different cell types, but the velocities of their myelinated culture was only 0.15 m/s greater than the unmyelinated culture. This could be due to the myelination being restricted to develop and mature within the microchannels and that is why I did not use microchannels longer than 100 μm. Even though still in 2D, the axon/glia interaction would occur in an open well and not be restricted by a few microns hindering myelination.

When testing the microchannels with mouse myelinating cultures, even with 50 μm long microchannels, I was unable to achieve axonal growth into the second compartment as the cells remained and developed in the cell seeding compartment. As the overall aim of the microchannels was to isolate axons from cell bodies, the length of the microchannels could be further reduced to as low as 5 μm in an attempt for achieving the same results as the hCCNs with other cells like those from the mouse spinal cord.

5.3 Characterising Electrically Active Human and Animal Neuronal Cultures

5.3.1 Human Neural Cultures

Human dopaminergic neurons and hCCNs were tested electrically using voltage-clamp electrophysiology as well as culturing on commercial and custom MEAs to validate the MEA measurements. Sodium current densities of both neuronal cultures increased with time in culture, following weekly assessments with patch-clamp and as expected the addition of TTX blocked the sodium voltage-sensitive currents. Unlike the dopaminergic cultures, no excitatory spontaneous postsynaptic currents (ESPCs) were recorded in the

hCCNs throughout the 4 weeks tested. ESPCs were observed from week 2 of dopaminergic cultures in both TH+ and TH- cells. These results were confirmed as dopaminergic cultures positively stained for synaptophysin (presynaptic) and PSD-95 (postsynaptic) whereas hCCNs did not show any electrical or immunological evidence for the presence of synapses. These findings were expected as it is already known that hCCNs require a long time (over 4 weeks) in culture before they start firing spontaneous action potentials and for functional synapses to be form (Shi *et al.*, 2012). In contrast the human dopaminergic neurons showed earlier signs of synapse formation from as early week 2 (Yang *et al.*, 2019) which is comparable to the data shown in Chapter 3.

In addition, I showed that culture of human dopaminergic neurons was possible on both commercial and custom MEAs which provided further information on the electrical behaviour of the cells. The dopaminergic cultures were electrically active from week 4 to week 6 which was expected from the findings using voltage-clamp. The main difference between these two techniques is that with patch-clamp you can selectively choose which cell to analyse and therefore distinguish between TH+ or TH- neurons whereas with MEAs the electrical activity is recorded from the whole culture as long as they are growing over the electrodes.

My recordings indicated that two distinct waveforms were present in the electrical activity traces. These waveforms were classified as ‘fast’ and ‘slow’ depending on their duration. ‘Fast’ waveform had a duration of less than 3 ms and waveforms with a duration greater than 3 ms were classified as ‘slow’. The ‘slow’ waveform activity was more prominent (about 70%) than ‘fast’ waveform activity (about 30%) throughout the culture period (4 to 6 weeks). There was no change in ‘fast’ waveform shape whereas the slow waveforms became narrower with time, which can be explained by the synaptic maturation that is known to occur in dopaminergic cultures (Shi *et al.*, 2012).

5.3.2 Mouse Neural Cultures

Mouse spinal cord cultures were electrically active from 2 DIV up until 52 DIV on commercial MEAs. In Chapter 4, I show that you can follow the development of these cells by looking at their waveforms, spike frequency and bursting of activity as well as perform additive pharmacology to investigate the origin of the electrical activity recorded. The shape of ‘fast’ and ‘slow’ waveforms was altered with as the DIV

increased. Broadening of 'fast' waveforms was observed with an increase in DIV which could be attributed to the change of sodium ion channel distribution along unmyelinated and myelinated axons (Vacher, Mohapatra and Trimmer, 2008). Similarly, to human dopaminergic cultures, the 'slow' waveforms became narrower which could again be due to synaptic maturation but in this case could also be caused by the redistribution of calcium channels on the axons during the process of myelination (Lai and Jan, 2006).

5.4 Assessing Myelination *in vitro* using MEAs

An increase in electrode-to-electrode NCV over time was measured from mouse spinal cord cultures using commercial MEAs. A large and significant increase in NCV was recorded from 6 to 10 DIV as it went from 0.03 m/s to 6.38 m/s. This increase suggests that myelination began which is at least 2 days earlier than what previous studies have found when staining for CNP (Bijland *et al.*, 2019) or that maturation of axons and increasing sodium channel distribution generated faster NCVs. NCVs continued to increase up until the last possible recording at 24 DIV which was the peak NCV measured at 15.0 m/s. I was unable to calculate NCV past 24 DIV as no 'fast' electrical activity was recorded from 25 DIV onwards, possibly due to the increase of myelinated axons growing over the recording electrodes.

The increase in NCV was expected as it is known that during that time period is when myelination occurs in mouse *in vitro* cultures (Thomson *et al.*, 2006). When compared to the study that measured conduction velocity in myelinating rat DRG neurons (Sakai *et al.*, 2017) the peak velocity measured here is about 25 times greater. To my knowledge, the NCV measurements I present in this thesis are the highest velocity recorded *in vitro* thus far. Future work to enhance these results would be to add demyelinating drugs such as amiodarone, dichloroacetate, tumor necrosis factor-α antagonists and measure its effect on conduction velocity and possible recovery as demyelination occurred. This would allow to study the process of demyelination and remyelination *in vitro* and an investigation of possible neuroprotective agents.

The next step would involve culturing these mouse spinal cord neurons on custom MEAs with microchannels (biochip), as on commercial MEAs the cells randomly grow over the electrodes in a disorganised manner. Therefore, the source of the electrically activity cannot be pinpointed to a certain number of cells and also relies on the spontaneous

activity of the cultures. Replacing that with a biochip, would allow for a more organised and controlled growth as the cell bodies would remain in a separate compartment to the axons and also have the ability to stimulate the cell bodies to evoke an action potential that would be recorded from the electrodes in the axonal compartment. Adding a source of stimulation means that neuronal cultures that are not spontaneously active such as hCCNs, can also be investigated and used for in models to study myelination.

5.5 Conclusions

This work has aimed at developing a system integrating MEAs and microchannels that can be used as a tool for investigating neurodegenerative diseases like multiple sclerosis. To do this, functional custom MEAs were fabricated and were tested using hNSCs, hCCNs, human dopaminergic cultures and mouse spinal cord cultures. The fabricated microchannels were able to successfully separate hCCN cell bodies and axons in two different compartments. Myelination was assessed electrically using commercial MEAs and mouse spinal cord cultures by showing that conduction velocity increases with time thus indicating an improvement in myelin compaction. This involved the development of analysis protocols for electrical events that can be standardised and applied to the myelinating cultures and represent a relatively simple and cost-effective approach to interrogate the electrical behaviour of the cultures across time.

In conclusion, the findings from this thesis provide proof that MEAs and microfluidics are excellent tools for developing *in vitro* neurological disease models as cells can be electrically analysed and manipulated over long periods of time. Combining the two to form a biochip adds an extra advantage as cell cultures can now be spatially investigated and thus try to mimic the cells environment in the human CNS or PNS.

References

- Achyuta, A. K. H. *et al.* (2013) 'A modular approach to create a neurovascular unit-on-a-chip', *Lab on a Chip*, 13(4), pp. 542–553. doi: 10.1039/c2lc41033h.
- Aggarwal, S. *et al.* (2013) 'Myelin membrane assembly is driven by a phase transition of myelin basic proteins into a cohesive protein meshwork.', *PLoS biology*, 11(6), p. e1001577. doi: 10.1371/journal.pbio.1001577.
- Aharoni, R. (2015) 'Remyelination in multiple sclerosis: realizing a long-standing challenge.', *Expert review of neurotherapeutics*, 7175(November), pp. 1–4. doi: 10.1586/14737175.2015.1112740.
- Antel, J. *et al.* (2012) 'Primary progressive multiple sclerosis: Part of the MS disease spectrum or separate disease entity?', *Acta Neuropathologica*, 123(5), pp. 627–638. doi: 10.1007/s00401-012-0953-0.
- Arancibia-Cárcamo, I. L. *et al.* (2017) 'Node of ranvier length as a potential regulator of myelinated axon conduction speed', *eLife*, 6, pp. 1–15. doi: 10.7554/eLife.23329.
- Axolbio (2016) 'Human iPSC-Derived Neural Stem Cells'. Available at: https://www.axolbio.com/page/neural-stem-cells-cerebral-cortex.
- Azim, K. and Butt, A. M. (2011) 'GSK3β negatively regulates oligodendrocyte differentiation and myelination in vivo', *Glia*, 59(4), pp. 540–553. doi: 10.1002/glia.21122.
- Bakkum, D. J. *et al.* (2013) 'Tracking axonal action potential propagation on a high-density microelectrode array across hundreds of sites', *Nature Communications*, 4. doi: 10.1038/ncomms3181.
- Bartzsch, H. *et al.* (2009) 'Electrical insulation properties of sputter-deposited SiO 2′ Si 3N 4 and Al 2O 3 films at room temperature and 400 °C', *Physica Status Solidi (A) Applications and Materials Science*, 206(3), pp. 514–519. doi: 10.1002/pssa.200880481.
- Bean, B. P. (2007) 'The action potential in mammalian central neurons', *Nature Reviews Neuroscience*, 8(6), pp. 451–465. doi: 10.1038/nrn2148.
- Berényi, A. *et al.* (2014) 'Large-scale, high-density (up to 512 channels) recording of local circuits in behaving animals', *Journal of Neurophysiology*, 111(5), pp. 1132–1149. doi: 10.1152/jn.00785.2013.
- Bijland, S. *et al.* (2019) 'An in vitro model for studying CNS white matter:

Functional properties and experimental approaches', *F1000Research*, 8(0), pp. 1–24. doi: 10.12688/f1000research.16802.1.

- Bird, M. and James, D. W. (1975) 'Myelin formation in cultures of previously dissociated mouse spinal cord', *Cell and Tissue Research*, 162(1), pp. 93–105. doi: 10.1007/BF00223265.
- Black, B. J., Atmaramani, R. and Pancrazio, J. J. (2017) 'Spontaneous and evoked activity from murine ventral horn cultures on microelectrode arrays', *Frontiers in Cellular Neuroscience*, 11(September), pp. 1–10. doi: 10.3389/fncel.2017.00304.
- Blakemore, W. F. (1973) 'Remyelination of the superior cerebellar peduncle in the mouse following demyelination induced by feeding cuprizone', *Journal of the Neurological Sciences*, 20(1), pp. 73–83. doi: 10.1016/0022-510X(73)90119-6.
- Braak, H. *et al.* (2003) 'Staging of brain pathology related to sporadic Parkinson's disease', *Neurobiology of Aging*, 24(2), pp. 197–211. doi: 10.1016/S0197-4580(02)00065-9.
- Bradl, M. and Lassmann, H. (2010) 'Oligodendrocytes: biology and pathology.', *Acta neuropathologica*, 119(1), pp. 37–53. doi: 10.1007/s00401-009-0601-5.
- Brady, S. T. *et al.* (1999) 'Formation of compact myelin is required for maturation of the axonal cytoskeleton', *Journal of Neuroscience*, 19(17), pp. 7278–7288. doi: 10.1523/jneurosci.19-17-07278.1999.
- Campenot, R. B. (1977) 'Local control of neurite development by nerve growth factor', *Proceedings of the National Academy of Sciences*, 74(10), pp. 4516–4519. doi: 10.1073/pnas.74.10.4516.
- Canter, R. G., Penney, J. and Tsai, L. H. (2016) 'The road to restoring neural circuits for the treatment of Alzheimer's disease', *Nature*, 539(7628), pp. 187–196. doi: 10.1038/nature20412.
- Cogan, S. F. (2008) 'Neural Stimulation and Recording Electrodes', *Annual Review of Biomedical Engineering*, 10(1), pp. 275–309. doi: 10.1146/annurev.bioeng.10.061807.160518.
- Coquinco, A. *et al.* (2014) 'A microfluidic based in vitro model of synaptic competition', *Molecular and Cellular Neuroscience*, 60(November 2015), pp. 43–52. doi: 10.1016/j.mcn.2014.03.001.
- Craig, A. *et al.* (2003) 'Quantitative analysis of perinatal rodent oligodendrocyte lineage progression and its correlation with human', *Experimental Neurology*, 181(2), pp. 231–240. doi: 10.1016/S0014-4886(03)00032-3.

- Douvaras, P. *et al.* (2014) 'Efficient generation of myelinating oligodendrocytes from primary progressive multiple sclerosis patients by induced pluripotent stem cells.', *Stem cell reports*, 3(2), pp. 250–9. doi: 10.1016/j.stemcr.2014.06.012.
- Douvaras, P. and Fossati, V. (2015) 'Generation and isolation of oligodendrocyte progenitor cells from human pluripotent stem cells.', *Nature protocols*, 10(8), pp. 1143–54. doi: 10.1038/nprot.2015.075.
- Dugger, B. N. and Dickson, D. W. (2017) 'Pathology of neurodegenerative diseases', *Cold Spring Harbor Perspectives in Biology*, 9(7), pp. 1–22. doi: 10.1101/cshperspect.a028035.
- Durães, F., Pinto, M. and Sousa, E. (2018) 'Old drugs as new treatments for neurodegenerative diseases', *Pharmaceuticals*, 11(2), pp. 1–21. doi: 10.3390/ph11020044.
- Dzamko, N., Geczy, C. L. and Halliday, G. M. (2015) 'Inflammation is genetically implicated in Parkinson's disease', *Neuroscience*, 302, pp. 89–102. doi: 10.1016/j.neuroscience.2014.10.028.
- Dziedzic, T. *et al.* (2010) 'Wallerian degeneration: A major component of early axonal pathology in multiple sclerosis', *Brain Pathology*, 20(5), pp. 976–985. doi: 10.1111/j.1750-3639.2010.00401.x.
- Eick, S. *et al.* (2009) 'Iridium oxide microelectrode arrays for in vitro stimulation of individual rat neurons from dissociated cultures', *Frontiers in Neuroengineering*, 2(NOV), pp. 1–12. doi: 10.3389/neuro.16.016.2009.
- Euston, M. R. S. (2017) *Membrane Currents and Pacemaking in Corticotrophs and hiPSC-Derived Dopaminergic Neurons*.
- Farooqi, N., Gran, B. and Constantinescu, C. S. (2010a) 'Are current disease-modifying therapeutics in multiple sclerosis justified on the basis of studies in experimental autoimmune encephalomyelitis?', *Journal of neurochemistry*, 115(4), pp. 829–44. doi: 10.1111/j.1471-4159.2010.06982.x.
- Farooqi, N., Gran, B. and Constantinescu, C. S. (2010b) 'Are current disease-modifying therapeutics in multiple sclerosis justified on the basis of studies in experimental autoimmune encephalomyelitis?', *Journal of Neurochemistry*, 115(4), pp. 829–844. doi: 10.1111/j.1471-4159.2010.06982.x.
- le Feber, J. *et al.* (2015) 'Barbed channels enhance unidirectional connectivity between neuronal networks cultured on multi electrode arrays', *Frontiers in Neuroscience*, 9(November), pp. 1–10. doi: 10.3389/fnins.2015.00412.

- Feigin, V. L. *et al.* (2019) 'Global, regional, and national burden of neurological disorders, 1990–2016: a systematic analysis for the Global Burden of Disease Study 2016', *The Lancet Neurology*, 18(5), pp. 459–480. doi: 10.1016/S1474-4422(18)30499-X.
- Feinstein, A., Freeman, J. and Lo, A. C. (2015) 'Treatment of progressive multiple sclerosis: what works, what does not, and what is needed.', *The Lancet. Neurology*, 14(2), pp. 194–207. doi: 10.1016/S1474-4422(14)70231-5.
- Franklin, R. J. M. (2015) 'Regenerative Medicines for Remyelination: From Aspiration to Reality', *Cell Stem Cell*, 16(6), pp. 576–577. doi: 10.1016/j.stem.2015.05.010.
- Freeman, S. A. *et al.* (2015) 'Acceleration of conduction velocity linked to clustering of nodal components precedes myelination', *Proceedings of the National Academy of Sciences of the United States of America*, 112(3), pp. E321–E328. doi: 10.1073/pnas.1419099112.
- Gautier, H. O. B. *et al.* (2015) 'Neuronal activity regulates remyelination via glutamate signalling to oligodendrocyte progenitors', *Nature Communications*, 6, p. 8518. doi: 10.1038/ncomms9518.
- Gehrmann, J. *et al.* (1995) 'Amyloid precursor protein (APP) expression in multiple sclerosis lesions', *Glia*, 15(2), pp. 141–151. doi: 10.1002/glia.440150206.
- Ghane-Motlagh, B. and Sawan, M. (2013) 'A review of Microelectrode Array technologies: Design and implementation challenges', *2013 2nd International Conference on Advances in Biomedical Engineering, ICABME 2013*, pp. 38–41. doi: 10.1109/ICABME.2013.6648841.
- Goda, Y. and Davis, G. W. (2003) 'Mechanisms of synapse assembly and disassembly', *Neuron*, 40(2), pp. 243–264. doi: 10.1016/S0896-6273(03)00608-1.
- Goldman, S. A. and Kuypers, N. J. (2015) 'How to make an oligodendrocyte', *Development*, 142(23), pp. 3983–3995. doi: 10.1242/dev.126409.
- Gruchot, J. *et al.* (2019) 'The Molecular Basis for Remyelination Failure in Multiple Sclerosis', *Cells*, 8(8), pp. 1–14. doi: 10.3390/cells8080825.
- Gutiérrez, R. *et al.* (1995) 'Decompaction of CNS myelin leads to a reduction of the conduction velocity of action potentials in optic nerve', *Neuroscience Letters*, 195(2), pp. 93–96. doi: 10.1016/0304-3940(94)11789-L.

- Hodgkin, A. L. and Huxley, A. F. (1952) 'Currents carried by sodium and potassium ions through the membrane of the giant axon of Loligo', *The Journal of Physiology*, 116(4), pp. 449–472. doi: 10.1113/jphysiol.1952.sp004717.
- Inglese, M. (2006) 'Multiple sclerosis: new insights and trends.', *AJNR. American journal of neuroradiology*, 27(5), pp. 954–7. doi: 10.1016/j.apjtb.2016.03.009.
- Ito, D., Komatsu, T. and Gohara, K. (2013) 'Measurement of saturation processes in glutamatergic and GABAergic synapse densities during long-term development of cultured rat cortical networks', *Brain Research*, 1534, pp. 22–32. doi: 10.1016/j.brainres.2013.08.004.
- Jacobs, J. (2016) 'Multiple Sclerosis: associated cardiometabolic risks and impact of exercise therapy', (April).
- Jagielska, A. *et al.* (2012) 'Mechanical Environment Modulates Biological Properties of Oligodendrocyte Progenitor Cells', *Stem Cells and Development*, 21(00), pp. 2905–2914. doi: 10.1089/scd.2012.0189.
- Jakovcevski, I. *et al.* (2009) 'Oligodendrocyte development and the onset of myelination in the human fetal brain.', *Frontiers in neuroanatomy*, 3(June), p. 5. doi: 10.3389/neuro.05.005.2009.
- Jensen, W., Yoshida, K. and Hofmann, U. G. (2006) 'In-vivo implant mechanics of flexible, silicon-based ACREO microelectrode arrays in rat cerebral cortex', *IEEE Transactions on Biomedical Engineering*, 53(5), pp. 934–940. doi: 10.1109/TBME.2006.872824.
- Johnstone, A. F. M. *et al.* (2010) 'Microelectrode arrays: A physiologically based neurotoxicity testing platform for the 21st century', *NeuroToxicology*, 31(4), pp. 331–350. doi: 10.1016/j.neuro.2010.04.001.
- Jongbloets, B. C. and Pasterkamp, R. J. (2014) 'Semaphorin signalling during development', *Development*, 141(17), pp. 3292–3297. doi: 10.1242/dev.105544.
- Kalb, R., Giesser, B. and Costello, K. (2012) *Multiple Sclerosis For Dummies*.
- Kim, G. H. *et al.* (2018) 'Recent progress on microelectrodes in neural interfaces', *Materials*, 11(10). doi: 10.3390/ma11101995.
- Kim, H. J. *et al.* (2012) 'Integrated Microfluidics Platforms for Investigating Injury and Regeneration of CNS Axons', *Annals of Biomedical Engineering*, 40(6), pp. 1268–1276. doi: 10.1007/s10439-012-0515-6.
- Kullmann, D. M. *et al.* (2005) 'Presynaptic, extrasynaptic and axonal GABAA receptors in the CNS: where and why?', *Progress in Biophysics and Molecular*

Biology, 87(1), pp. 33–46. doi: 10.1016/j.pbiomolbio.2004.06.003.

- Kutzelnigg, A. and Lassmann, H. (2014) *Pathology of multiple sclerosis and related inflammatory demyelinating diseases*. 1st edn, *Handbook of Clinical Neurology*. 1st edn. Elsevier B.V. doi: 10.1016/B978-0-444-52001-2.00002-9.
- Lai, H. C. and Jan, L. Y. (2006) 'The distribution and targeting of neuronal voltage-gated ion channels', *Nature Reviews Neuroscience*, 7(7), pp. 548–562. doi: 10.1038/nrn1938.
- Lappe-Siefke, C. *et al.* (2003) 'Disruption of Cnp1 uncouples oligodendroglial functions in axonal support and myelination', *Nature Genetics*, 33(3), pp. 366–374. doi: 10.1038/ng1095.
- Lassmann, H., Brück, W. and Lucchinetti, C. (2001) 'Heterogeneity of multiple sclerosis pathogenesis: implications for diagnosis and therapy.', *Trends in molecular medicine*, 7(3), pp. 115–21. doi: 10.1016/S1471-4914(00)01909-2.
- Lee, H. J. *et al.* (2015) 'A multichannel neural probe with embedded microfluidic channels for simultaneous in vivo neural recording and drug delivery', *Lab on a Chip*, 15(6), pp. 1590–1597. doi: 10.1039/C4LC01321B.
- Livesey, M. R. *et al.* (2015) 'Functional properties of in vitro excitatory cortical neurons derived from human pluripotent stem cells.', *The Journal of physiology*, 00(July), pp. 1–10. doi: 10.1113/JP270660.
- Logan, S. *et al.* (2019) 'Studying Human Neurological Disorders Using Induced Pluripotent Stem Cells: From 2D Monolayer to 3D Organoid and Blood Brain Barrier Models', *Comprehensive Physiology*, 9(2), pp. 565–611. doi: 10.1002/cphy.c180025.
- Lovas, G. *et al.* (2000) 'Axonal changes in chronic demyelinated cervical spinal cord plaques', *Brain*, 123, pp. 308–317. doi: 10.1093/brain/123.2.308.
- Lublin, F. D. and Reingold, S. C. (1996) 'Defining the clinical course of multiple sclerosis: Results of an international survey', *Neurology*, 46(4), pp. 907–911. doi: 10.1212/WNL.46.4.907.
- Mackenzie, I. S. *et al.* (2014) 'Incidence and prevalence of multiple sclerosis in the UK 1990-2010: a descriptive study in the General Practice Research Database.', *Journal of neurology, neurosurgery, and psychiatry*, 85(1), pp. 76–84. doi: 10.1136/jnnp-2013-305450.
- Majumdar, D. *et al.* (2011) 'Co-culture of neurons and glia in a novel microfluidic platform.', *Journal of neuroscience methods*, 196(1), pp. 38–44. doi:

10.1016/j.jneumeth.2010.12.024.

- Martinez-Lozada, Z. *et al.* (2014) 'Activation of sodium-dependent glutamate transporters regulates the morphological aspects of oligodendrocyte maturation via signaling through calcium/calmodulin-dependent kinase IIβ's actin-binding/-stabilizing domain', *Glia*, 62(9), pp. 1543–1558. doi: 10.1002/glia.22699.
- Matsushima, G. K. and Morell, P. (2001) 'The neurotoxicant, cuprizone, as a model to study demyelination and remyelination in the central nervous system', *Brain Pathology*, 11(1), pp. 107–116. doi: 10.1111/j.1750-3639.2001.tb00385.x.
- Melle, G. *et al.* (2020) 'Intracellular Recording of Human Cardiac Action Potentials on Market-Available Multielectrode Array Platforms', *Frontiers in Bioengineering and Biotechnology*, 8(February), pp. 1–10. doi: 10.3389/fbioe.2020.00066.
- Miccoli, B. *et al.* (2019) 'High-density electrical recording and impedance imaging with a multi-modal CMOS multi-electrode array chip', *Frontiers in Neuroscience*, 13(JUN), pp. 1–14. doi: 10.3389/fnins.2019.00641.
- MicroChem (2015) 'SU-8 2000 Permanent Epoxy Negative Photoresist Processing Guidelines', *SU-8 2000 Datasheet*, (MicroChem), pp. 1–5.
- Mikhailova, M. M. *et al.* (2019) 'Primary culture of mouse embryonic spinal cord neurons: Cell composition and suitability for axonal regeneration studies', *International Journal of Neuroscience*, 129(8), pp. 762–769. doi: 10.1080/00207454.2019.1567508.
- Millet, L. J. *et al.* (2007) 'Microfluidic devices for culturing primary mammalian neurons at low densities.', *Lab on a chip*, 7(8), pp. 987–94. doi: 10.1039/b705266a.
- Mohan, H. *et al.* (2015) 'Dendritic and axonal architecture of individual pyramidal neurons across layers of adult human neocortex', *Cerebral Cortex*, 25(12), pp. 4839–4853. doi: 10.1093/cercor/bhv188.
- Monk, K. R., Feltri, M. L. and Taveggia, C. (2015) 'New insights on schwann cell development', *Glia*. doi: 10.1002/glia.22852.
- Morin, F. *et al.* (2006) 'Constraining the connectivity of neuronal networks cultured on microelectrode arrays with microfluidic techniques: A step towards neuron-based functional chips', *Biosensors and Bioelectronics*, 21(7), pp. 1093–1100. doi: 10.1016/j.bios.2005.04.020.
- Morris, J. H., Hudson, A. R. and Weddell, G. (1972) 'A study of degeneration and

regeneration in the divided rat sciatic nerve based on electron microscopy', *Zeitschrift f□r Zellforschung und Mikroskopische Anatomie*. doi: 10.1007/bf00981944.

- Mozafari, S. *et al.* (2015) 'Skin-derived neural precursors competitively generate functional myelin in adult demyelinated mice', *Journal of Clinical Investigation*, 125(9), pp. 3642–3656. doi: 10.1172/JCI80437.
- MS Society (2020) 'MS Prevalence Report', (January), pp. 1–7. Available at: https://www.mssociety.org.uk/what-we-do/our-work/our-evidence/ms-in-the-uk.
- Multichannel Systems (2015) 'Micro-electrode Array (MEA) Manual'.
- Nam, Y. and Wheeler, B. C. (2011) 'In vitro microelectrode array technology and neural recordings', *Critical Reviews in Biomedical Engineering*, 39(1), pp. 45–61.
- Nave, K.-A. and Werner, H. B. (2014) 'Myelination of the Nervous System: Mechanisms and Functions', *Annual Review of Cell and Developmental Biology*, 30, pp. 503–533. doi: 10.1146/annurev-cellbio-100913-013101.
- Neutelings, T. *et al.* (2013) 'Effects of Mild Cold Shock (25°C) Followed by Warming Up at 37°C on the Cellular Stress Response', *PLoS ONE*, 8(7), pp. 1–15. doi: 10.1371/journal.pone.0069687.
- Obien, M. E. J. *et al.* (2015) 'Revealing neuronal function through microelectrode array recordings', *Frontiers in Neuroscience*, 9(JAN), p. 423. doi: 10.3389/fnins.2014.00423.
- Odawara, A. *et al.* (2016) 'Physiological maturation and drug responses of human induced pluripotent stem cell-derived cortical neuronal networks in long-term culture.', *Scientific reports*, 6(April), p. 26181. doi: 10.1038/srep26181.
- Orabona, E. *et al.* (2013) 'Photomasks fabrication based on optical reduction for microfluidic applications', *Micromachines*, 4(2), pp. 206–214. doi: 10.3390/mi4020206.
- Park, J. *et al.* (2009) 'Microfluidic compartmentalized co-culture platform for CNS axon myelination research', *Biomedical Microdevices*, 11(6), pp. 1145–1153. doi: 10.1007/s10544-009-9331-7.
- Park, J. *et al.* (2012a) 'Multi-compartment neuron-glia co-culture platform for localized CNS axon-glia interaction study.', *Lab on a chip*, 12(18), pp. 3296–304. doi: 10.1039/c2lc40303j.
- Park, J. *et al.* (2012b) 'Multi-compartment neuron–glia co-culture platform for

localized CNS axon–glia interaction study', *Lab on a Chip*, 12(18), p. 3296. doi: 10.1039/c2lc40303j.

- Park, J. *et al.* (2014) 'A microchip for quantitative analysis of CNS axon growth under localized biomolecular treatments.', *Journal of neuroscience methods*, 221(9), pp. 166–74. doi: 10.1016/j.jneumeth.2013.09.018.
- Park, J. W. *et al.* (2008) 'Quantitative analysis of CNS axon regeneration using a microfluidic neuron culture device', *Biochip Journal*, 2(1), pp. 44–51.
- Parkinson, J. (1817) *An essay on shaking palsy*, *Sherwood, Neely and Jones*.
- Piaton, G. *et al.* (2011) 'Class 3 semaphorins influence oligodendrocyte precursor recruitment and remyelination in adult central nervous system', *Brain*, 134(4), pp. 1156–1167. doi: 10.1093/brain/awr022.
- Pine, J. (1980) 'Recording action potentials from cultured neurons with extracellular microcircuit electrodes', *Journal of Neuroscience Methods*, 2(1), pp. 19–31. doi: 10.1016/0165-0270(80)90042-4.
- Poewe, W. *et al.* (2017) 'Parkinson disease', *Nature Reviews Disease Primers*, 3, pp. 1–21. doi: 10.1038/nrdp.2017.13.
- Przedborski, S., Vila, M. and Jackson-Lewis, V. (2003) 'Neurodegeneration: What is it and where are we?', *Journal of Clinical Investigation*, 111(1), pp. 3–10. doi: 10.1172/JCI200317522.
- Ray Dorsey, E. *et al.* (2018) 'Global, regional, and national burden of Parkinson's disease, 1990–2016: a systematic analysis for the Global Burden of Disease Study 2016', *The Lancet Neurology*, 17(11), pp. 939–953. doi: 10.1016/S1474-4422(18)30295-3.
- Renshaw, B., Forbes, A. and Morison, B. R. (1940) 'ACTIVITY OF ISOCORTEX AND HIPPOCAMPUS: ELECTRICAL STUDIES WITH MICRO-ELECTRODES', *Journal of Neurophysiology*, 3(1), pp. 74–105. doi: 10.1152/jn.1940.3.1.74.
- Rivers, T. M. and Schwentker, F. F. (1935) 'ENCEPHALOMYELITIS ACCOMPANIED BY MYELIN DESTRUCTION EXPERIMENTALLY PRODUCED IN MONKEYS', *The Journal of Experimental Medicine*, 61(5), pp. 689–702. doi: 10.1084/jem.61.5.689.
- Rolston, J. D., Gross, R. E. and Potter, S. M. (2009) 'A low-cost multielectrode system for data acquisition enabling real-time closed-loop processing with rapid recovery from stimulation artifacts', *Frontiers in Neuroengineering*, 2(JUL), pp.

1–17. doi: 10.3389/neuro.16.012.2009.

- Di Ruscio, A. *et al.* (2015) 'Multiple sclerosis: getting personal with induced pluripotent stem cells.', *Cell death & disease*, 6(7), p. e1806. doi: 10.1038/cddis.2015.179.
- Ryynänen, T. *et al.* (2011) 'All Titanium microelectrode array for field potential measurements from neurons and cardiomyocytes-A Feasibility Study', *Micromachines*, 2(4), pp. 394–409. doi: 10.3390/mi2040394.
- Sakai, K. *et al.* (2017) 'A co-culture microtunnel technique demonstrating a significant contribution of unmyelinated Schwann cells to the acceleration of axonal conduction in Schwann cell-regulated peripheral nerve development', *Integrative Biology (United Kingdom)*, 9(8), pp. 678–686. doi: 10.1039/c7ib00051k.
- Scelfo, B. *et al.* (2012) 'Application of multielectrode array (MEA) chips for the evaluation of mixtures neurotoxicity', *Toxicology*, 299(2–3), pp. 172–183. doi: 10.1016/j.tox.2012.05.020.
- Schierbeek, A. (1953) 'The collected letters of Antoni van Leeuwenhoek; an appeal to the scientific world.', *Antonie van Leeuwenhoek*, 19(3), pp. 181–8. Available at: http://www.ncbi.nlm.nih.gov/pubmed/13080983.
- Selvaraj, V. *et al.* (2012) 'Differentiating human stem cells into neurons and glial cells for neural repair.', *Frontiers in bioscience: a journal and virtual library*, 17(October 2015), pp. 65–89. Available at: http://eutils.ncbi.nlm.nih.gov/entrez/eutils/elink.fcgi?dbfrom=pubmed&id=22201733&retmode=ref&cmd=prlinks%5Cnpapers2://publication/uuid/06A4D609-0816-4662-A843-AC9AF99A21D6.
- Semple, B. D. *et al.* (2013) 'Brain development in rodents and humans: Identifying benchmarks of maturation and vulnerability to injury across species', *Progress in Neurobiology*, 106–107, pp. 1–16. doi: 10.1016/j.pneurobio.2013.04.001.
- Shi, S. H. *et al.* (1999) 'Rapid spine delivery and redistribution of AMPA receptors after synaptic NMDA receptor activation', *Science*, 284(5421), pp. 1811–1816. doi: 10.1126/science.284.5421.1811.
- Shi, Y. *et al.* (2012) 'Human cerebral cortex development from pluripotent stem cells to functional excitatory synapses.', *Nature neuroscience*, 15(3), pp. 477–86, S1. doi: 10.1038/nn.3041.

- Shimba, K. *et al.* (2019) 'Evaluation of Conduction Properties of Sensory Axons with High-Density Microelectrode Array', *BMEiCON 2019 - 12th Biomedical Engineering International Conference*, pp. 19–22. doi: 10.1109/BMEiCON47515.2019.8990233.
- Simons, M. and Trajkovic, K. (2006) 'Neuron-glia communication in the control of oligodendrocyte function and myelin biogenesis', *J.Cell Sci.*, 119(0021-9533 (Print)), pp. 4381–4389. doi: 10.1242/jcs.03242.
- Snaidero, N. *et al.* (2014) 'Myelin membrane wrapping of CNS axons by PI(3,4,5)P3-dependent polarized growth at the inner tongue.', *Cell*, 156(1–2), pp. 277–90. doi: 10.1016/j.cell.2013.11.044.
- Sperry, Z. J. *et al.* (2018) 'Flexible microelectrode array for interfacing with the surface of neural ganglia', *Journal of Neural Engineering*, 15(3), p. 036027. doi: 10.1088/1741-2552/aab55f.
- Steffens, H., Dibaj, P. and Schomburg, E. D. (2012) 'In vivo measurement of conduction velocities in afferent and efferent nerve fibre groups in mice', *Physiological Research*, 61(2), pp. 203–214. doi: 10.33549/physiolres.932248.
- Sternberger, N. H. *et al.* (1978) 'Myelin basic protein demonstrated immunocytochemically in oligodendroglia prior to myelin sheath formation.', *Proceedings of the National Academy of Sciences*, 75(5), pp. 2521–2524. doi: 10.1073/pnas.75.5.2521.
- Stifani, N. (2014) 'Motor neurons and the generation of spinal motor neuron diversity', *Frontiers in Cellular Neuroscience*, 8(OCT), pp. 1–22. doi: 10.3389/fncel.2014.00293.
- Takahashi, K. and Yamanaka, S. (2006) 'Induction of Pluripotent Stem Cells from Mouse Embryonic and Adult Fibroblast Cultures by Defined Factors', *Cell*, 126(4), pp. 663–676. doi: 10.1016/j.cell.2006.07.024.
- Takeda, A. *et al.* (1998) 'Abnormal accumulation of NACP/α-synuclein in neurodegenerative disorders', *American Journal of Pathology*, 152(2), pp. 367–372.
- Taylor, A. M. *et al.* (2010) 'Microfluidic Local Perfusion Chambers for the Visualization and Manipulation of Synapses', *Neuron*, 66(1), pp. 57–68. doi: 10.1016/j.neuron.2010.03.022.
- Taylor, J. P., Brown, R. H. and Cleveland, D. W. (2016) 'Decoding ALS: From genes to mechanism', *Nature*, 539(7628), pp. 197–206. doi:

10.1038/nature20413.

- Technologies, S. (no date) *STEMdiff ™ Dopaminergic Neuron Differentiation and Maturation Protocol*.
- Thomas, C. A. *et al.* (1972) 'A miniature microelectrode array to monitor the bioelectric activity of cultured cells', *Experimental Cell Research*, 74(1), pp. 61–66. doi: 10.1016/0014-4827(72)90481-8.
- Thomson, C. E. *et al.* (2006) 'Murine spinal cord explants: A model for evaluating axonal growth and myelination in vitro', *Journal of Neuroscience Research*, 84(8), pp. 1703–1715. doi: 10.1002/jnr.21084.
- Thomson, C. E. *et al.* (2008) 'Myelinated, synapsing cultures of murine spinal cord - Validation as an in vitro model of the central nervous system', *European Journal of Neuroscience*, 28(8), pp. 1518–1535. doi: 10.1111/j.1460-9568.2008.06415.x.
- Thomson, J. A. *et al.* (1998a) 'Embryonic stem cell lines derived from human blastocysts.', *Science (New York, N.Y.)*, 282(5391), pp. 1145–7. doi: 10.1126/science.282.5391.1145.
- Thomson, J. A. *et al.* (1998b) 'Embryonic stem cell lines derived from human blastocysts.', *Science (New York, N.Y.)*, 282(5391), pp. 1145–7. doi: 10.1126/science.282.5391.1145.
- Tieu, K. (2011) 'A guide to neurotoxic animal models of Parkinson's disease', *Cold Spring Harbor Perspectives in Medicine*, 1(1), pp. 1–20. doi: 10.1101/cshperspect.a009316.
- Trapp, B. D. *et al.* (1998) 'Axonal transection in the lesions of multiple sclerosis.', *The New England journal of medicine*, 338(5), pp. 278–85. doi: 10.1056/NEJM199801293380502.
- Vabnick, I. *et al.* (1999) 'Dynamic potassium channel distributions during axonal development prevent aberrant firing patterns', *Journal of Neuroscience*, 19(2), pp. 747–758. doi: 10.1523/jneurosci.19-02-00747.1999.
- Vacher, H., Mohapatra, D. P. and Trimmer, J. S. (2008) 'Localization and Targeting of Voltage-Dependent Ion Channels in Mammalian Central Neurons', *Physiological Reviews*, 88(4), pp. 1407–1447. doi: 10.1152/physrev.00002.2008.
- Vassall, K. A., Bamm, V. V and Harauz, G. (2015) 'MyelStones: the executive roles of myelin basic protein in myelin assembly and destabilization in multiple sclerosis.', *The Biochemical journal*, 472(1), pp. 17–32. doi:

10.1042/BJ20150710.

- Virchow, R. and Chance, F. (1860) *Cellular Pathology as based upon physiological and pathological histology. Twenty lectures delivered in... 1858. Translated from the second edition of the*. Available at: https://books.google.co.uk/books?hl=en&lr=&id=59pUAAAAcAAJ&oi=fnd&pg=PR15&ots=8YKVffkIUW&sig=54yQ-ksP6Uq2R1jrmeN_jvmFzWc (Accessed: 8 May 2016).
- Wallin, M. T. *et al.* (2019) 'Global, regional, and national burden of multiple sclerosis 1990–2016: a systematic analysis for the Global Burden of Disease Study 2016', *The Lancet Neurology*, 18(3), pp. 269–285. doi: 10.1016/S1474-4422(18)30443-5.
- Wang, S. *et al.* (2013) 'Human iPSC-derived oligodendrocyte progenitor cells can myelinate and rescue a mouse model of congenital hypomyelination.', *Cell stem cell*, 12(2), pp. 252–64. doi: 10.1016/j.stem.2012.12.002.
- Wang, S. S.-H. *et al.* (2008) 'Functional trade-offs in white matter axonal scaling.', *The Journal of neuroscience : the official journal of the Society for Neuroscience*, 28(15), pp. 4047–56. doi: 10.1523/JNEUROSCI.5559-05.2008.
- Wanke, E. *et al.* (2016) 'Neuron-glia cross talk revealed in reverberating networks by simultaneous extracellular recording of spikes and astrocytes' glutamate transporter and K+ currents', *Journal of Neurophysiology*, 116(6), pp. 2706–2719. doi: 10.1152/jn.00509.2016.
- Ward, A. A. and Thomas, L. B. (1955) 'The electrical activity of single units in the cerebral cortex of man', *Electroencephalography and Clinical Neurophysiology*, 7(1), pp. 135–136. doi: 10.1016/0013-4694(55)90067-5.
- Van Wart, A. and Matthews, G. (2006) 'Expression of sodium channels Nav1.2 and Nav1.6 during postnatal development of the retina', *Neuroscience Letters*, 403(3), pp. 315–317. doi: 10.1016/j.neulet.2006.05.019.
- Weinshenker, B. G. *et al.* (1989) 'The natural history of multiple sclerosis: a geographically based study. I. Clinical course and disability.', *Brain : a journal of neurology*, 112, pp. 133–146. doi: 10.1093/brain/122.10.1941.
- Wilson, H. C., Onischke, C. and Raine, C. S. (2003) 'Human Oligodendrocyte Precursor Cells In Vitro: Phenotypic Analysis and Differential Response to Growth Factors', *Glia*, 44(2), pp. 153–165. doi: 10.1002/glia.10280.
- Wisniewski, H. M. *et al.* (1989) 'Cytoskeletal protein pathology and the formation

of beta-amyloid fibers in Alzheimer's disease', *Neurobiology of Aging*, 10(5), pp. 409–412. doi: 10.1016/0197-4580(89)90079-1.

- Wood, C., Williams, C. and Waldron, G. J. (2004) 'Patch clamping by numbers', *Drug Discovery Today*, 9(10), pp. 434–441. doi: 10.1016/S1359-6446(04)03064-8.
- Wu, G. F. and Alvarez, E. (2011) 'The immunopathophysiology of multiple sclerosis.', *Neurologic clinics*, 29(2), pp. 257–78. doi: 10.1016/j.ncl.2010.12.009.
- Xiang, G. *et al.* (2007) 'Microelectrode array-based system for neuropharmacological applications with cortical neurons cultured in vitro', *Biosensors and Bioelectronics*, 22(11), pp. 2478–2484. doi: 10.1016/j.bios.2006.09.026.
- Xue, P. *et al.* (2014) 'Protein covalently conjugated SU-8 surface for the enhancement of mesenchymal stem cell adhesion and proliferation', *Langmuir*, 30(11), pp. 3110–3117. doi: 10.1021/la500048z.
- Yang, H. *et al.* (2019) 'Generation of functional dopaminergic neurons from human spermatogonial stem cells to rescue parkinsonian phenotypes', *Stem Cell Research and Therapy*, 10(1), pp. 1–19. doi: 10.1186/s13287-019-1294-x.
- Yi, Y. *et al.* (2015) 'Central Nervous System and its Disease Models on a Chip', *Trends in Biotechnology*, xx, pp. 1–15. doi: 10.1016/j.tibtech.2015.09.007.
- Yvert, B., Branchereau, P. and Meyrand, P. (2004) 'Multiple Spontaneous Rhythmic Activity Patterns Generated by the Embryonic Mouse Spinal Cord Occur Within a Specific Developmental Time Window', *Journal of Neurophysiology*, 91(5), pp. 2101–2109. doi: 10.1152/jn.01095.2003.
- Zuchero, J. B. and Barres, B. A. (2015) 'Glia in mammalian development and disease.', *Development (Cambridge, England)*, 142(22), pp. 3805–9. doi: 10.1242/dev.129304.